ORSAY
n° d'ordre :

LAL XX-XX
Décembre 2003

Mémoire d'Habilitation à Diriger des Recherches

A high power Fabry-Pereot resonator for Compton Polarimetry with the longitudinally polarised lepton beams at HERA

Fabian Zomer

Habilitation soutenue le lundi 22 décembre 2003, devant la commission d'examen :

MM.	D. Barber	rapporteur
	A. Blondel	rapporteur
	M. Davier	président
	M. Klein	rapporteur
	C. Pascaud	

Contents

Pour Matthieu, mon fils
Pour ma famille
Pour mes amis

"Wenn man sich sein Haus fertig gebaut hat, merkt man, unversehens Etwas dabei gelernt zu haben, das man schlechterdings hätte wissen müssen, bevor man zu bauen-anfieng."

("Quand on a construit une maison, on a généralement appris quelque chose qu'on aurait dû savoir avant de commencer à construire.")

F. Nietzsche (Jenseits von gut und böse)

Introduction

This document was written in order to obtain the French Habilitation Diploma. Since considerable freedom is allowed for the substance and the form of such a document, I have taken this opportunity to provide a rather detailed technical report on the new HERA polarimeter.

After approximately height years of running, the HERA electron-proton Collider of the German DESY Laboratory has undergone major machine upgrades. These modifications – which took place during the years 2001-2002 – have two aims: an increase of the electron-proton luminosity by a factor of four and the supply of longitudinally polarised electrons at the high energy electron-proton interactions points, i.e. within the two detectors H1 and ZEUS.

During the first year of operation, HERA-II had encountered very difficult background conditions at the H1 and ZEUS interaction points. To reach the high luminosity, it was realised that further modifications of the electron-proton interaction point regions were required. This was the purpose of the year 2003 HERA-II shutdown.

In spite of these difficulties, the good news came from the electron beam polarisation. Just before the 2003 shutdown, the H1 and ZEUS spin rotators, used to polarise longitudinally the naturally transversally polarised electrons, were switched on and a polarisation of 50 % was reached.

To cover accurately the physics of high luminosity polarised electron-proton collisions, an upgrade of the longitudinal polarimeter was proposed and accepted at the end of 2000. This new polarimeter, currently installed at HERA and waiting for its commissioning, is the main topic of this document.

In chapter 1, studies of the impact of the polarisation measurement accuracy on three observables, the right-handed and the standard charged current cross-sections and the determination of the light quark couplings to the Z^0 are presented. These topics do not obviously cover all the HERA upgrade programme but they are quite representative of the requirements for the precision on the polarisation measurement. The main point is that, unlike small polarisation asymmetry measurements, absolute cross section measurements are very sensitive to the polarisation uncertainties. Since the electron-proton luminosity is expected to increase by a factor of four, we show that the accuracy of the polarisation measurements must increase as well.

In the second chapter, the beam polarisation built up and the Compton polarimetry are presented. Very briefly, Compton polarimetry consists in measuring and analysing the energy spectrum of photons backscattered after laser-electron interactions. The polarimeter performances then rely, not only but essentially, on the choice of laser. In this context, I complete this chapter by a study of the statistic and systematics uncertainties related to Compton polarimetry. From this study, we conclude that a continuous laser

beam of a few kilo Watts is desirable to full-fill the physics requirements given in chapter 1.

The polarimeter upgrade, proposed to reach the laser power defined in chapter 2, is described in chapter 3. The core of this polarimeter is a high finesse Fabry-Pérot cavity filled by a 750 mW ND:YaG laser. This optical resonator, made of two super-mirrors located around the electron beam, provides a few kilo Watts laser beam. The main experimental difficulties related to the operation of such a device are discussed, namely the mechanical implementation at HERA and the conditions to maintain the optical resonance. The experimental setup consists in two separate pieces: an optical bench and a calorimeter located approximately 60 m downstream. Both pieces, together with their related control and readout electronics are also described.

One important point of the optical setup is the control and the measurement of the laser light polarisation, this is the subject of chapter 4. In this chapter, basics of light polarimetry (usually called ellipsometry) are given. We describe the setups used to measure the laser beam polarisation and to create a laser circular polarisation. This is a very important aspect of our polarimeter since the determination of the electron beam polarisation depends directly on the level of the laser circular polarisation. Results of the calibration of a prototype ellipsometer are reported and an estimate of the uncertainty on the laser polarisation measurement is given.

Before reaching the final design of the cavity installed at HERA, a prototype cavity has been built and operated at Orsay. Results of the laser/cavity alignments and performances of the laser power amplification with this prototype are described in chapter 6. I also give the performances of the final cavity that we operated both at Orsay and HERA (without electron beam at the time of writing this document).

An appendix is devoted to electromagnetic calculations related to laser beam propagation in anisotropic plates. This technical work was required in order to reach a high level of accuracy in the determination of the laser polarisation.

Before ending this introduction, I would like to emphasise that this document does not only describe my personal contribution but the work of an entire group. The list of the contributors is: Baroyer, E. Barrelet, W. Beckhusen and his group, C. Berg and his group, R. Bernier, F. Berny, F. Blot, M. Bouchel, V. Brisson, T. Caceres, J. Colin, P. Favre, P. Corona, P. Deck, M. Desmond, H. Hirseman, Y. Holler, M. Jacquet-Lemire, B. Jacquemard, J. Ludwig, F. Marechal, R. Marie, N. Meyners, C. Pascaud, E. Pfuetzenreuter and his group, Y. Queinnec, A. Reboux, D. Richard, P. Rivoirard, C. Ronic, K. Sieber, V. Soskov,T. Szatkowski, S. Trochet, Z. Zhang and the LAL workshop group, the LAL administrative group and myself.

Chapter 1

Polarisation and HERA Upgrade Physics program

With HERA-II, the physics of longitudinally polarised lepton – unpolarised proton scattering at high momentum transfer is opened. Experiments of this kind have been carried out in the past at SLAC [1] and at CERN [2] but on fixed targets and therefore at small transfer momentum. Though their sensitivity to the electroweak parameters was very small, these early precise experiments have confirmed the universality of the Standard Model in lepton-hadron deep inelastic scattering.

With HERA-II, among a large number of physics topics, a high precision electroweak physics program becomes feasible with longitudinally polarised charged lepton-proton deep inelastic scattering. These topics were discussed during a workshop held in 1995-1996 [3] and more recently, new topics related to the Quantum-Chromo-Dynamics were covered in refs. [4, 5]. The experimental advantage of an electron-proton collider experiment, with respect to a fixed target neutrino-nucleus experiment is manifold (see appendix 1.5.1).

Briefly summarising, the use of longitudinally polarised lepton beams allow to pin down chiral couplings, that is the couplings of the quarks to the Z^0 in the Standard Model. In theories going beyond the Standard Model, additional chiral couplings also appear. This is the case for lepto-quarks models or super-symmetry theories with R-parity violation. For these researches, the lepton beam polarisation helps to improve the limits on these couplings and in case of discovery, to discriminate between various theoretical scenarios. Assuming that the Standard Model holds, longitudinally polarised lepton beams also bring new constraints on the parton density functions [4] and on the parton-parton correlation functions [5].

Although the HERA-II physics programme has been extensively discussed in ref. [3], the propagation of the statistical and systematic uncertainties of the polarisation measurement to the physics results were not fully investigated in that document.

This point had to be investigated for the HERA longitudinal polarimeter upgrade proposal [6]. In this context, I have performed a statistical analysis of the effects of the polarisation measurements for three physics topics: determination of the right handed charged current (RH) cross-section, measurement of the charged current (CC) cross section and determination of the light quark coupling constants to the Z^0. In addition, I also studied the potential gain obtained by doing the analyses with a polarisation binning. This work is described in detail in the present chapter.

In the following sections, I assume that the reader is familiar with the kinematics and

dynamics of deep inelastic electron-proton scattering. If not, I have included an introduction to this topic in the appendix of this chapter. This appendix describes the unpolarised cross-section measurements and the related structure function physics analyses performed before the HERA-II machine upgrade. For a complete review concerning unpolarised ep deep inelastic scattering, I refer to the Habilitation document of Zhiqing Zhang [7].

1.1 Right Handed Charged Current

The search for right handed charged current (RH CC) in e^-p deep inelastic scattering is one of the most spectacular subjects that one can cover with a longitudinally polarised lepton beam. For a detailed introduction to this search we refer to ref. [8]. Here, it suffices to say that the RH CC is a non standard contribution to the pure V-A coupling of the CC process. In e^-p and e^+p interactions, it is taken into account by writing the observed CC cross sections in the following way

$$\sigma^{e^+}_{obs,CC}(P) = \frac{1+P}{2}\sigma^{e^+}_{CC} + \frac{1-P}{2}\sigma^{e^+}_{LH} \tag{1.1}$$

$$\sigma^{e^-}_{obs,CC}(P) = \frac{1-P}{2}\sigma^{e^-}_{CC} + \frac{1+P}{2}\sigma^{e^-}_{RH} \tag{1.2}$$

where: $\sigma^{e^+}_{LH}$ and $\sigma^{e^-}_{RH}$ are vanishing in the standard model and represent the RH CC cross-sections; $\sigma^{e^+}_{CC}$ and $\sigma^{e^-}_{CC}$ are the standard CC cross sections (see eq. 1.24 in appendix 1.5.1) and correspond to the reactions $e^+_R + p \to \bar{\nu}_e + X$ and $e^-_L + p \to \nu_e + X$, respectively.

From eqs. 1.1 and 1.2, one sees that $\sigma^{e^+}_{LH}$ and $\sigma^{e^-}_{RH}$ can be measured by combining e^+ and e^- beam data and/or different polarisation $P > 0$ and $P < 0$. A data sample of beam charge $\pm$ and polarisation $\pm|P|$ will be denoted by $e^{\pm}_{\pm|P|}$ throughout this chapter.

Among the possible cross section ratios one can build using the four data samples $\{e^{\pm}_{\pm|P|}\}$, the following [8]

$$R_4(|P|) = \frac{\sigma^{e^+}_{obs,CC}(-|P|) + \sigma^{e^-}_{obs,CC}(|P|)}{\sigma^{e^+}_{obs,CC}(|P|) + \sigma^{e^-}_{obs,CC}(-|P|)} \tag{1.3}$$

is sensitive to the RH CC signal. In this expression, the subscript *obs* refers to the measured cross section at a given value of the lepton beam polarisation P.

Note that, according to the above definition one gets $\sigma^{e^+}_{obs,CC}(P=0) = \sigma^{e^+}_{CC}/2$ in the standard model. Defining further

$$r_4 = \frac{\sigma^{e^+}_{LH} + \sigma^{e^-}_{RH}}{\sigma^{e^+}_{CC} + \sigma^{e^-}_{CC}} \text{ and } \quad \alpha = \frac{1-|P|}{1+|P|} \quad \Rightarrow \quad R_4(|P|) = \frac{\alpha + r_4}{1 + \alpha r_4}\,. \tag{1.4}$$

Notice that in the case where only two data samples $\{e^-_{\pm|P|}\}$ are available one has [8]

$$R_2(|P|) = \frac{\sigma^{e^-}_{obs,CC}(|P|)}{\sigma^{e^-}_{obs,CC}(-|P|)}\,, \quad r_2 = \frac{\sigma^{e^-}_{RH}}{\sigma^{e^-}_{CC}} \Longrightarrow R_2(|P|) = \frac{\alpha + r_2}{1 + \alpha r_2} \tag{1.5}$$

and an equivalent expression for e^+.

The value of r

$$r = \frac{R - \alpha}{1 - \alpha R} \, . \tag{1.6}$$

can then be obtained by measuring R and α.

However, neither the spin nor the charge of the lepton beam will be changed frequently at HERA. A measurement of R_2 (R_4) is then expected to appear after a few years of data taking with all the experimental problems implied by merging such data. With a fast and precise measurement of the lepton beam polarisation it is nevertheless possible to perform another kind of analysis based on a fit to the observed cross sections themselves as functions of the polarisation P. Writing eq. (1.2) as

$$\sigma^{e^-}_{obs,CC}(P) = \frac{\sigma^{e^-}_{CC} + \sigma^{e^-}_{RH}}{2} - P\frac{\sigma^{e^-}_{CC} - \sigma^{e^-}_{RH}}{2} \, , \tag{1.7}$$

$\sigma^{e^-}_{RH}$ is determined from a linear fit to the observed cross section as a function of P. This fit can be performed step by step during data taking if data are acquired during the polarisation rise in order to get a polarisation range from 0 to P_∞ (see chap. 2). The result of this fit is a model independent determination of $\sigma^{e^-}_{RH}$.

In both cases, the accuracy is limited by statistical and systematic errors on the cross section and on the polarisation measurements. Uncertainties on the CC cross section measurement, as estimated in H1, are shown in fig. 1.1 as a function of Q^2 and are of the order of a few percent where statistics is large (at high Q^2, systematics will decrease with an increase of the statistics). As for the polarisation uncertainties, they depend on the polarimeter performance.

The aim of the following studies is to determine what performance is required for the physics analysis. We start by an estimate of the influence of the polarisation's statistical and systematic accuracies on the r measurement (eq. 1.6). Because error propagations to the cross section measurement (eq. 1.7) are easily handled, the effects of the CC's systematics will be described for this measurement only.

1.1.1 Cross section ratio: the precision requirement for the polarisation measurement

For the sake of simplicity we shall consider r_2 and R_2 that we shall denote r and R.

Experimentally, the observed cross sections are derived from the number of events:

$$\sigma^{e^-}_{obs}(P) = \frac{N^-_{obs,P}}{\mathcal{L}_P(e^-)}$$

where $N^-_{obs,P}$ is the number of observed CC events with e^- beam of polarisation P and $\mathcal{L}_P(e^-)$ is the corresponding luminosity.

Statistical uncertainty

The statistical uncertainty of the R's measurement is therefore given by:

$$\frac{\delta R}{R} = \frac{\delta N^-_{obs,P}}{N^-_{obs,P}} \oplus \frac{\delta N^-_{obs,-P}}{N^-_{obs,-P}} \oplus \frac{\delta \mathcal{L}_P(e^-)}{\mathcal{L}_P(e^-)} \oplus \frac{\delta \mathcal{L}_{-P}(e^-)}{\mathcal{L}_{-P}(e^-)}$$

with $a \oplus b = \sqrt{a^2 + b^2}$. Here the correlations between the polarisation and luminosity measurements are effectively neglected. We therefore already assume that the luminosity monitor and the polarimeter are precise and fast enough to control these correlations (see chap. 2).

Assuming $r = 0$ for the error calculation and the same luminosity for both polarisation samples ($\mathcal{L}_P(e^-) \approx \mathcal{L}_{-P}(e^-)$) one gets

$$\frac{\delta R}{R} = \sqrt{\frac{4}{\sigma^{e^-}_{CC}(1-P^2)\mathcal{L}} + 2\left(\frac{\delta\mathcal{L}}{\mathcal{L}}\right)^2}.$$

From eq. 1.6 one further obtains the uncertainty on r:

$$\frac{\delta r}{r} = \frac{[4P\delta R] \ \oplus \ [2\sqrt{2}(1-R^2)\delta P]}{(1+P-R(1-P))(P-1+R(1+P))}\ , \tag{1.8}$$

where the factor $\sqrt{2}$ comes from the fact that there are two independent polarisation measurements having the same uncertainty δP. Substituting the expression of R one further gets:

$$\delta r = \frac{(1+P+r-Pr)^2}{4P}\delta R \oplus \frac{(1-r^2)}{\sqrt{2}P}\delta P\ ,$$

where it is obvious that the larger P, the smaller δr. Fig. 1.2 shows δr as a function of δP for an integrated luminosity of 250 pb^{-1} per data sample and neglecting the statistical uncertainty of the luminosity measurement: in order to be able to neglect the contribution of the polarisation statistical uncertainty one must keep $\delta P < 0.2 \times 10^{-2}$.

In eq. 1.8 the same value $|P|$ has been taken for the positive and the negative beam charge samples. In practice they may differ and eq. 1.8 can easily be modified by defining P_+ for the value of the positive beam charge and P_- for the negative beam charge. In fig. 1.2 δr as a function of δP is shown for $\delta R = 2\% R$ and $P_+ = 0.5$, $P_- = -0.4$ (dashed curve), $P_+ = 0.4$, $P_- = -0.5$ (dotted curve). As expected, δr is very sensitive to P_+ because of the $(1+P)/2$ polarisation weight of eq. 1.2.

The accuracy on the determination of r can be increased, in principle, by considering different values of P. This is possible by measuring the polarisation during the polarisation rise. This possibility will be described in the next section in the context on the cross-section measurement.

Effect of polarisation's systematic uncertainties

Finally, using eq. 1.5 one can also estimate the effect on r of an additive systematic shift $\delta_{add,sys}$ of the polarisation measurement. The simplest case corresponds to $\sigma_{RH} = 0$. In this case $r = 0$ and $R = (1-|P|)/(1+|P|)$ where $|P|$ is the polarisation delivered by HERA. However, the "measured" polarisation factor α reads as $\alpha = (1-|P|+\delta_{add,sys})/(1+|P|+\delta_{add,sys})$ so that one obtains a fake "measured" value of r:

$$r_{sys} = \frac{\delta_{add,sys}}{2+\delta_{add,sys}} \approx \frac{\delta_{add,sys}}{2}\ . \tag{1.9}$$

Therefore, looking at fig. 1.2, it appears to be crucial to keep the systematic uncertainty on the polarisation measurement below $\approx 5 \cdot 10^{-3}$ absolute.

Note that, if instead of an additive systematic shift, one considers a scaling systematic shift $\delta_{sca,sys}(P) \propto P$, then $\alpha = (1-|P+\delta_{sca,sys}(P)|)/(1+|P+\delta_{sca,sys}(P)|)$. As a result the systematic shift induced on the determination of r is also given by eq. 1.9 but with an opposite sign.

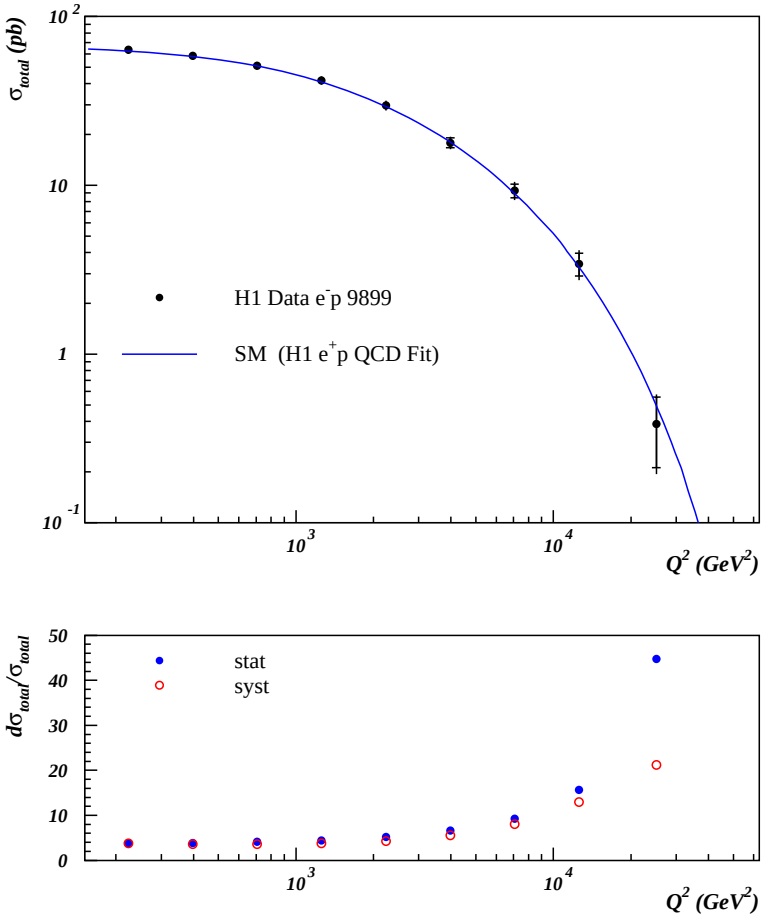

Figure 1.1: *Top plot: H1 measurement of* $\int_{Q^2}^{s}(d\sigma^{e^-}/dQ^2)dQ^2$ *as a function of* Q^2*. Bottom plot: estimates of the statistical and systematic uncertainties. From [23].*

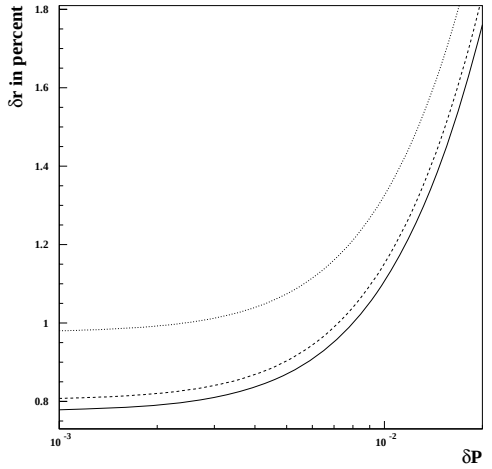

Figure 1.2: *Statistical uncertainty on the determination of r in % (see text) as a function of the statistical uncertainty of P. Full curve: $P_+ = 0.5$ and $P_- = -0.5$; dashed curve: $P_+ = 0.5$ and $P_- = -0.4$; dotted curve $P_+ = 0.4$ and $P_- = -0.5$. Systematics are not taken into account for this figure.*

1.1.2 Absolute cross-section: effect of the polarisation rise

To determine directly the RH CC, a linear fit to $\sigma^{e^-}_{obs,CC}(P)$ can be performed using eq. (1.7). Statistical and systematic uncertainties on the polarisation and $\sigma^{e^-}_{obs,CC}(P)$ measurements can thus be taken simultaneously into account.

Usually one divides the systematic uncertainties in two parts [9, 10]: 1) those which induce correlations between the measurements (usually named "correlated systematics") 2) those which do not induce correlations between the measurements ("uncorrelated systematics").

However, in the case of the observed CC cross section integrated over Q^2, only one measurement is considered and thus, this distinction doesn't make sense. Nevertheless two kinds of systematic uncertainties can be distinguished in this case [11]:

- Additive sources, i.e. those which do not depend either implicitly or explicitly on the polarisation: all systematic uncertainties related to the background subtraction (the contamination from the high Q^2 neutral current is in principle polarisation dependent, but this dependence shows up only at very high $Q^2 \approx M_Z^2$). For illustration, effects of an additive systematic shift is shown in the bottom plot of fig 1.3.

- Scaling sources, i.e. those which depend implicitly but not explicitly on the polarisation: all uncertainties which scale with the cross-section measurement, that is all except the additive one in the case of a single measurement (see the top plot of fig 1.3).

In order to perform a quantitative error propagation, we shall consider the situation where $\sigma^{e^-}_{RH} = 0$. This assumption implies that the uncertainty on $\sigma^{e^-}_{RH}$ is related to the

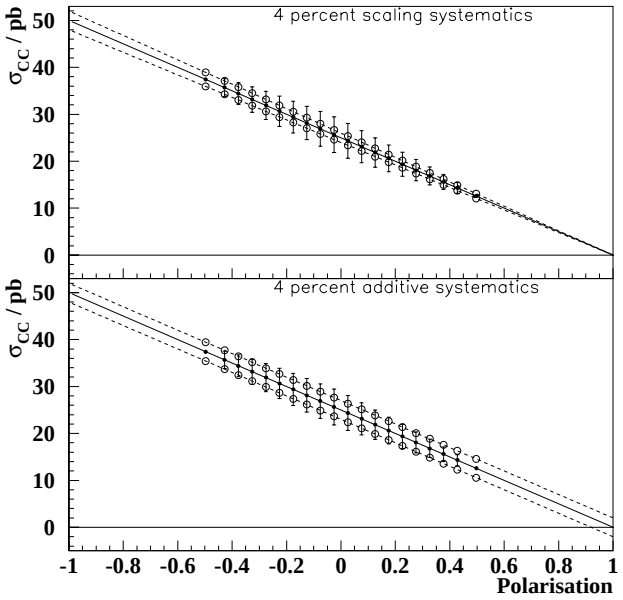

Figure 1.3: *Cross section as a function of polarisation for* $\mathcal{L} = 250\ pb^{-1}$ *per beam charge. Full dots show the nominal (unbiased) measurements and error bars are statistical only (see eq. 1.12 together with eq. 1.13 and 1.15). Empty dots show the shifts induced by* $\pm 4\%$ *scaling (top plot) and* $\pm 4\%$ *additive (bottom plot) systematic uncertainties. The full lines and the dashed lines are here as guide lines to illustrate how the unbiased and the biased cross sections behave respectively.*

limit of existence of the RH CC. In this case the error propagation is very simple. From eq. 1.7 one can see that the RH CC cross section is given by extrapolating $\sigma^{e^-}_{obs,CC}(P)$ to $P = +1$ (see fig. 1.3). Therefore, the uncertainty on $\sigma^{e^-}_{RH}$ depends only on the statistical uncertainty and on the additive systematic uncertainties.

In some sense, the search for RH CC is a measurement of the residual background if such a signal doesn't exist. It means that all systematic uncertainty studies related to the CC cross section measurement must also be performed for all backgrounds. In the case of the CC cross section these effects are of second order but they are of the first order for the RH CC.

Anticipating section 1.2 one also sees, from eq. 1.7, that the CC cross section is given by the ordinate intercept at $P = -1$ (see fig. 1.3). Therefore the uncertainty on this quantity depends on statistics and on both, additive and scaling, systematic uncertainty sources (the additive contribution being reduced by constraining the fit to the standard model expectation).

Note that the systematic error propagation is straightforward in these two physics cases. Nevertheless we shall incorporate them in the covariance matrix for sake of completeness.

Fit procedure

The simplest procedure to determine $\sigma^{e^-}_{RH}$ is the χ^2 minimisation. It is defined by

$$\chi^2 = \overrightarrow{V} \cdot W \overrightarrow{V}, \tag{1.10}$$

with W the inverse of the $n \times n$ (n = number of polarisation bins) covariance matrix and

$$V_i = \sigma^{e^-}_{obs,CC}(\bar{P}_i) - (a\bar{P}_i + b) \ .$$

a and b are the two unknown parameters[1]

$$a = -\frac{\sigma^{e^-}_{CC} - \sigma^{e^-}_{RH}}{2} \ ; b = \frac{\sigma^{e^-}_{CC} + \sigma^{e^-}_{RH}}{2} \ .$$

$\bar{P}_i$ is the averaged polarisation of the i^{th} bin.

a and b are determined by minimising the χ^2 and $\sigma^{e^-}_{RH}$ is finally given by

$$\sigma^{e^-}_{RH} = a + b \ \text{ with } \ \delta\sigma^{e^-}_{RH} = \sqrt{\overrightarrow{\partial}\Sigma . \mathcal{M}^{-1} \overrightarrow{\partial}\Sigma} \tag{1.11}$$

using standard statistical formula where $\mathcal{M}$ is the 2×2 fit matrix

$$\mathcal{M}_{ij} = \frac{1}{2}\frac{\partial^2\chi^2}{\partial p_i \partial p_j} \ ; p_1 \equiv a \ ; \ p_2 \equiv b$$

and $\overrightarrow{\partial}\Sigma = (1, 1)$ (i.e. partial derivative of $(a + b)$ by a and b). Note that the χ^2 is a quadratic form of a and b. Hence, since we are only interested in $\delta\sigma^{e^-}_{RH}$, the value of the

[1] We shall only perform a model independent analysis, i.e. two parameters are considered. Using further constraints, i.e. fixing $-a = b$ and looking at deviations from the SM predictions leads to a more accurate determination of a limit on the RH CC. This point is described in section 1.2.

χ^2 doesn't enter our calculations. Our estimates of $\delta\sigma^{e^-}_{RH}$ are then also valid for the case $\sigma^{e^-}_{RH} \neq 0$ up to the error treatment which assumes $\sigma^{e^-}_{RH} = 0$.

Instead of $a+b$, $(a+b)/(a-b)$ or $(-b/a)$ could have also been considered. It can be shown that for $\sigma^{e^-}_{RH} = 0$ all error estimates coincide. However, if $\sigma^{e^-}_{RH} \neq 0$, the derivative vector $\overrightarrow{\partial}\Sigma$ depends on a and b in the later two cases. Explicit values of a and b (i.e. a model for RH CC) are therefore required to perform the error calculations.

Returning to the calculation of $\delta\sigma^{e^-}_{RH}$, there are two contributions to consider:

- *Statistical uncertainty.* Neglecting for now the systematics, the matrix W is diagonal ($W_{ii} = w_i$) and depends on the luminosity since the statistical precision is estimated from the number of CC events:

$$\delta_{stat}(i) \approx \frac{\sqrt{N^{e^-}_{obs,CC}(\bar{P}_i)}}{\mathcal{L}_i} = \sqrt{\frac{\sigma^{e^-}_{CC}(1-\bar{P}_i)}{2\mathcal{L}_i}} \tag{1.12}$$

  and $w_i = 1/\delta^2_{stat}(i)$. $\mathcal{L}_i$ is the luminosity corresponding to the i^{th} bin, normalised to the total luminosity:

$$\mathcal{L}_i = C\int_{t(P_i)}^{t(P_{i+1})} \mathcal{L}(t)dt \;\; , \mathcal{L}(t) = \frac{1}{(1+0.42t/5.9)^{1/0.42}} \;\; , \;\; C = \frac{\mathcal{L}_{TOT}}{\sum_{i=0}^{n}\mathcal{L}_i} \; , \tag{1.13}$$

  where the following beam (time dependent) life time $\tau_L(t) \approx 0.42 \times t + 5.9$ with t given in hour, has been used as estimated by looking at a typical HERA fill (see fig. 2.5 in chap. 2); $t(P)$ is obtained by inverting the time evolution of the polarisation

$$P(t) = P_\infty[1 - \exp(-t/\tau)] \tag{1.14}$$

  with $\tau_P = \tau_{ST}/P_{ST} \times P_\infty$, $\tau_{ST} = 43.2$ min, $P_{ST} = 0.916$ as determined at HERA [12]. It is worth mentioning that the rising curve is not as smooth as eq. 1.14 in reality (see chap. 2). For numerical estimates $\mathcal{L}_{TOT} = 250$ pb^{-1} will be used. This number corresponds to the, optimistic, expected luminosity corresponding to one year of data taking. An average fill duration $t_{max} = 12$h will be chosen. In the expression for χ^2, the value of the polarisation $\bar{P}_i$ is the mean weighted by the luminosity:

$$\bar{P}_i = \frac{\int_{t(P_i)}^{t(P_{i+1})} P(t)\mathcal{L}(t)dt}{\mathcal{L}_i} \; . \tag{1.15}$$

- *Systematic uncertainties.* For CC, the sources of systematic uncertainties are determined for the whole data sample, so that they do not depend on the polarisation value. Therefore dividing the CC measurements into polarisation bins introduces a correlation between these bins. These effects are taken into account via the covariance matrix [11]:

$$\mathrm{Cov}_{ij} = \delta^2_{stat}(i)\delta_{ij} + \delta_{sca}(i) \times \delta_{sca}(j) + \delta_{add}(i) \times \delta_{add}(j) \tag{1.16}$$

  where δ_{ij} stands for the Kronecker symbol, $\delta_{add}(i)$ and $\delta_{sca}(i)$ are the additive and scaling systematic uncertainties respectively . If ϵ_{add} and ϵ_{sca} are the relative additive and relative scaling systematic uncertainties, then

$$\delta_{add}(i) \approx \epsilon_{add}\sigma^{e^-}_{CC} \quad , \quad \delta_{sca}(i) \approx \epsilon_{sca}\frac{1-\bar{P}_i}{2}\sigma^{e^-}_{CC} \; .$$

In these expressions the difference between scaling and additive uncertainties is explicit. The additive source is taken to be a fraction ϵ_{add} of a reference data sample of a given beam charge (here $P = -1 \Rightarrow \sigma_{obs} = \sigma_{CC}$): because the "background cross section" doesn't depend on polarisation, its contribution is the same in any polarisation bin i. On the contrary, the scaling uncertainty is proportional to the observed CC cross section (i.e. $\sigma^{e^-}_{CC}(1 - \bar{P}_i)/2$). For numerical estimates ϵ_{add} and ϵ_{sca} will be defined by the quadratic sum of all systematic uncertainties of each type since the measurement is the same in all polarisation bins.

It is worth mentioning that the covariance matrix expression (eq. 1.16) holds only in the case of symmetric systematic uncertainties. Asymmetric systematics require a special treatment [13] which can noticeably modify the results.

In fig. 1.4, $n^{e^-}_{obs,CC}$ is plotted as a function of P_i for two extreme bin widths, 0.5 and 0.01, using the numbers given above and $P_\infty = \pm 0.5$. One first remarks that, because of the polarisation and luminosity time evolution, the bulk of the statistics is located around $\pm|P_\infty|$. The use of the polarisation weighted by the luminosity reduces the maximum polarisation when the bin width is large (0.47 in our simplistic description). Note that because of the low statistics observed in certain bins the χ^2 procedure is not really adequate. The adequate statistical procedure should be the likelihood maximisation which is not considered here.

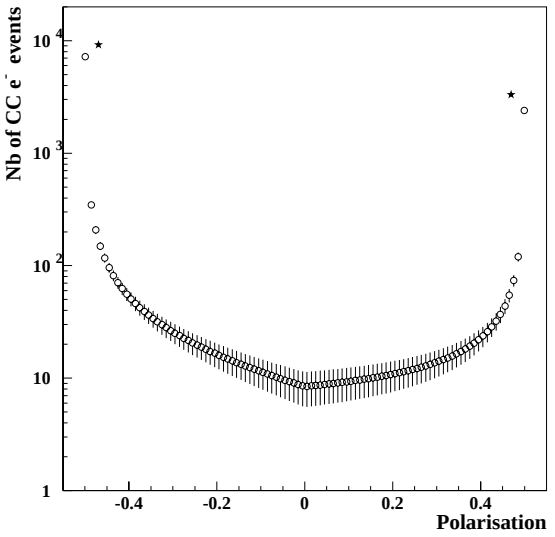

Figure 1.4: *Number of events computed using $\sigma^{e^-}_{CC} = 50$ pb as a function of the polarisation for two bin width, $dP = 0.5$ (stars) and $dP = 0.01$ (empty dots). Here two beam polarisation data samples are considered $e^-_{\pm|P|}$ and $|P_\infty| = 0.5$. Each sample represents 250 pb^{-1}. The statistical uncertainties shown in this figures reflect the polarisation build up curve as specified in the text as well as the luminosity decay during the fill. A luminosity fill duration of 12 h has been considered.*

Numerical estimates

To perform numerical estimates of $\delta(\sigma^{e^-}_{RH})$, we choose: $P_\infty = \pm 0.5$ (see eq. 1.14), $\sigma^{e^-}_{CC} = 50$ pb which corresponds to $Q^2 > 10^3$ GeV^2 (above this threshold the background is below 1%) and an average luminosity fill duration of 12h. As for the systematics we take $\epsilon_{sca} = 0.04$ and $\epsilon_{add} = 0.01$ (the value of ϵ_{add} is not determined in the unpolarised CC analyses, it is estimated from the uncertainty on the background subtraction). These are not exactly the numbers corresponding of the H1 1998-1999 $\sigma^{e^-}_{CC}$ measurement but the systematic error propagation is so simple that any change in the relative additive systematic uncertainty is directly applicable to $\delta(\sigma^{e^-}_{RH})$ (ϵ_{sca} has no effects as we shall see).

Three analyses are performed using:

- $[+/-]$ = two data samples $e^-_{-|P|}$ and $e^-_{+|P|}$;
- $[-]$ = single data sample $e^-_{-|P|}$;
- $[+]$ = single data sample $e^-_{+|P|}$.

For each data sample we take $\mathcal{L}_{TOT} = 250$ pb^{-1} (there are two times more events in analysis $[+/-]$ than in $[-]$ and $[+]$) and we vary the number of polarisation bins between 1 and 50.

Effect of CC's uncertainties only

The relative uncertainty $\delta(\sigma^{e^-}_{RH})$ has been estimated, for the three analyses, according to the procedure described in the previous sections.

To illustrate such a linear fit, the error band of the $[+/-]$ analysis, when no polarisation bins are used, is shown in fig. 1.5. $\delta(\sigma^{e^-}_{RH})$ is given by the extrapolation of the error band at $P = +1$ and $\delta(\sigma^{e^-}_{CC})$ by the extrapolation at $P = -1$.

Another parameter has been introduced for this study: a timing threshold above which the luminosity and polarisation measurements begin. For now, in the HERMES analyses, only runs with $|P| > 0.4$ are used for physics (below this limit, the polarisation measurement is currently not precise enough). For $|P_\infty| = 0.5$ and using our simplistic polarisation build up formula, $|P| = 0.4$ is reached at $t = 40$ min. Therefore we show the error estimates as a function of the polarisation bin width for three timing thresholds $t_{cut} = 0$, 10 min (one may not be able to take data at the beginning of the luminosity run) and 40 min.

As a result, $\delta(\sigma^{e^-}_{RH})$ decreases significantly when the polarisation bin width decreases for the $[+]$ and $[-]$ analyses (see fig. 1.6). There is no improvement for the $[+/-]$ analysis as can be seen from fig. 1.7. The reason is that, because of the linearity, no additional information is provided by the polarisation binning when two charge samples are considered.

In order to illustrate the effect of the non-diagonal terms of the covariant matrix (= the correlations), we have repeated the $[+/-]$ analysis by fixing $\mathrm{Cov}_{ij} = 0$ for $i \neq j$. The result is shown in fig. 1.7. Without accounting for these terms, the uncertainty on $\delta(\sigma^{e^-}_{RH})$ is overestimated as well as the influence of the polarisation bin width.

Another study that can be made is the polarisation/depolarisation scenario: once the polarisation growth is finished, the beam is depolarised so that another rise starts again. One can model it by changing the average duration of the run to, say, 2.5 h (it is 12h

for the results given above). The results are shown in fig. 1.6 for the analysis [+]. With this scenario one looses sensitivity for all the analyses since the weight of the largest polarisation value is reduced.

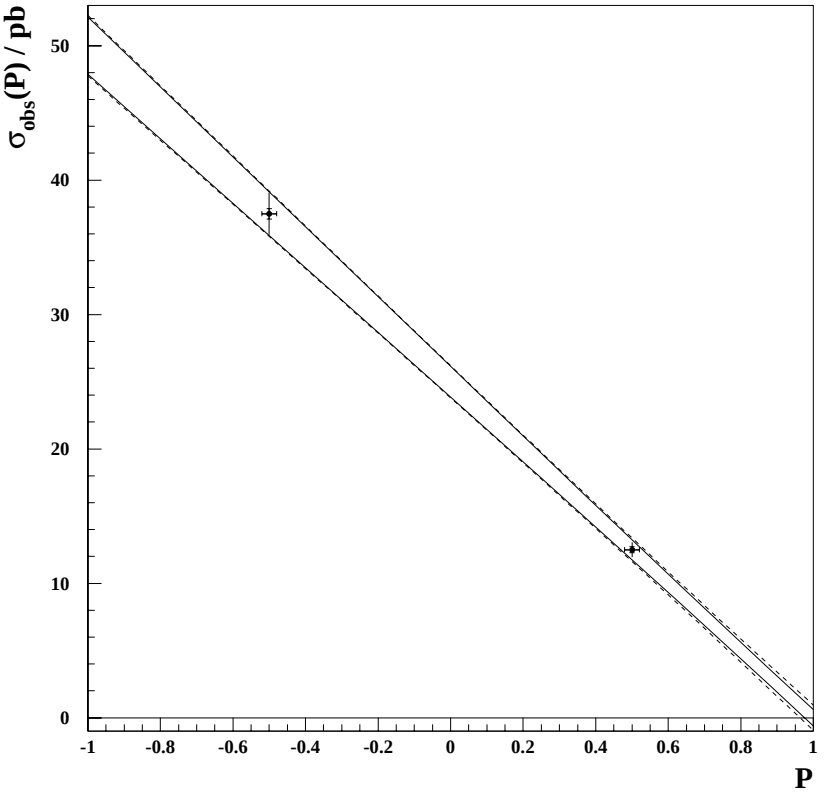

Figure 1.5: *CC cross section measurement together with the error band computing from the linear fit. Two beam polarisation data samples are considered* $e^-_{\pm|P|}$ *and* $|P_\infty| = 0.5$. *Each sample represents 250* pb^{-1}. *The inner error bar of each data point represents the statistical uncertainty and the outer error bars is obtained by adding quadratically the statistical at the systematic uncertainties. The full curve correspond to the case where the statistical uncertainty on the polarisation measurement is fixed to 0.2% and the dashed curve to 2%.*

Effects of CC's uncertainties and polarisation's statistical uncertainty

The influence of the statistical uncertainty of the polarisation is estimated by adding quadratically $\delta P \times \sigma^{e^-}_{CC}/2$ to the diagonal of the covariance matrix (eq. 1.16). The result is shown in fig. 1.8 (see also fig. 1.5). As already stated in section 1.1.1,we also find here that the polarisation's statistical accuracy must be kept at the few per mill level, even when the CC cross section's uncertainties are taken into account. The gain by going from $P_\infty = 0.5$ to $P_\infty = 0.6$ is also shown. In the same figure another scenario is shown: a sample of $e^-_{|P_\infty|}$ corresponding to 250pb^{-1} and a sample of unpolarised e^- corresponding to the HERA-I data taking are combined. As a result it appears that this

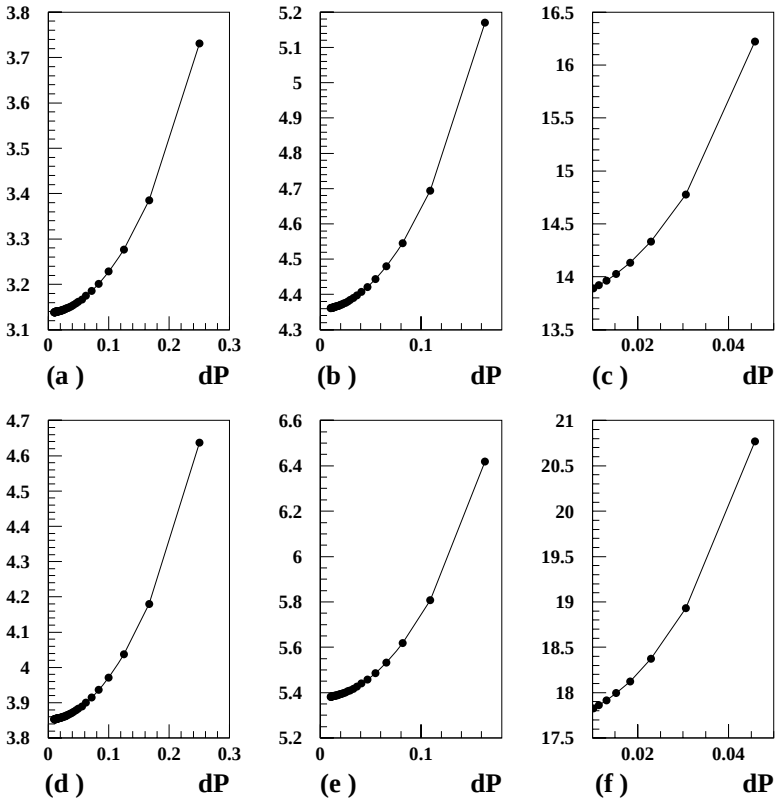

Figure 1.6: *All plots show the uncertainty (statistical plus systematics) on* $\sigma^{e^-}_{RH}/\sigma_{SM}$ *in percent for* $Q^2 > 1000\ GeV^2$ *as a function of the polarisation bin width* dP*. These results are obtained from a* χ^2 *minimisation for one data sample* $e^+_{\pm|P|}$ *and* $|P_\infty| = 0.5$*, corresponding to 250* pb^{-1}*. The plots of the first column (a,d) correspond to* $t_{cut} = 0$ *(see text); the second column (b,e) to* $t_{cut} = 10$ *min; the third column (c,f) to* $t_{cut} = 40$ *min. Plots (a), (b), (c) correspond to an average luminosity fill duration of 12 h and plots (d), (e), (f) to 2.5 h.*

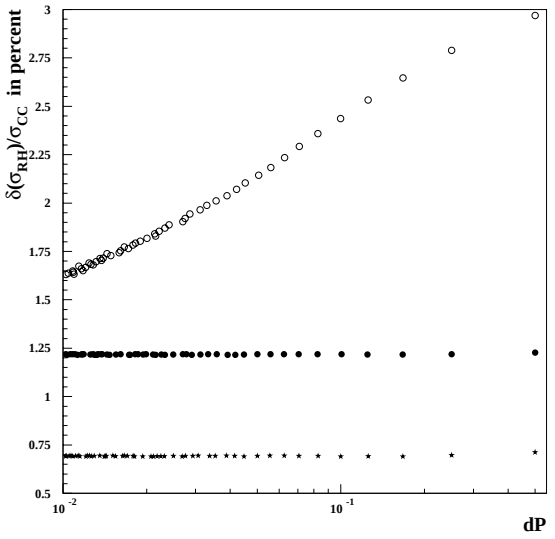

Figure 1.7: *Uncertainties on $\sigma^{e^-}_{RH}/\sigma_{SM}$ as a function of the polarisation bin width dP. These results are obtained from a χ^2 minimisation to two data samples $e^-_{\pm|P|}$ with $|P_\infty| = 0.5$, each corresponding to 250 pb^{-1}. The stars show the contribution of the statistical uncertainty; the full dots takes into account all systematic uncertainties (see text) and the open circle are the results of the calculations where the non-diagonal terms of the covariance matrix are neglected.*

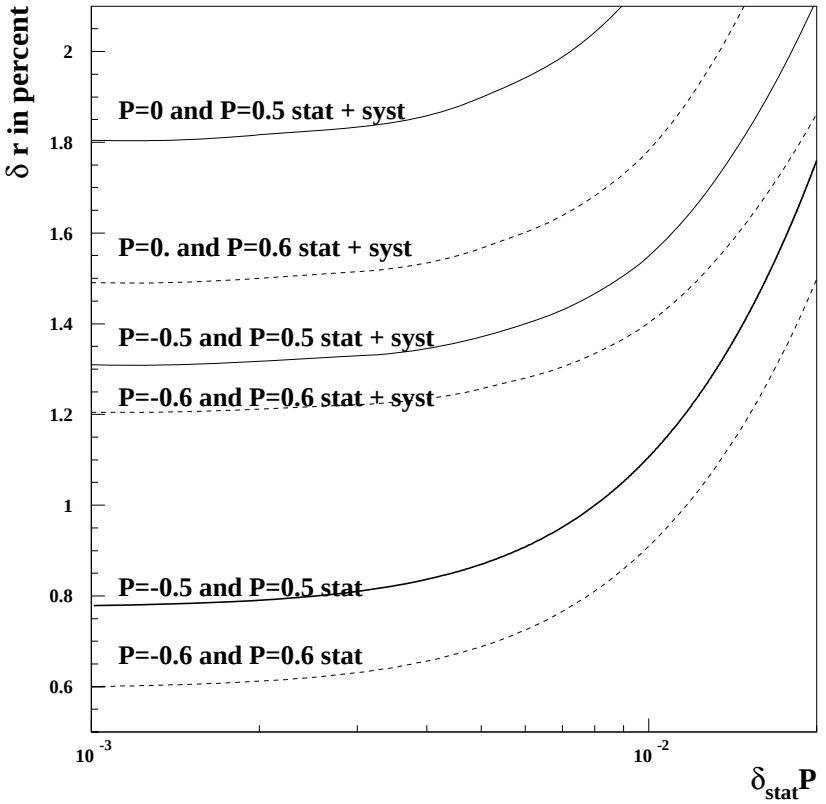

Figure 1.8: *Uncertainties on $\sigma^{e^-}_{RH}/\sigma_{SM}$ as a function of the polarisation statistical uncertainty δP. The curves for which the statistical and systematic uncertainties on the CC cross section are taken into account are obtained from a χ^2 minimisation to the two data samples $e^-_{\pm|P|}$ (for two cases $P = \pm 0.5$ and $P = \pm 0.6$), each corresponding to 250 pb^{-1}. The curves for which only the statistical uncertainty are considered have been determined as explained in section 1.1.1. For comparison, results of the χ^2 fit to the positive polarised and a 100 pb^{-1} unpolarised independent data samples are also shown (=curved denoted by $P = 0$ and $P \neq 0$).*

scenario permits a determination of RH CC better than the 2% level. The difference between the analysis [+/−], the optimum case, and this latter scenario decreases as the polarisation $|P_\infty|$ increases.

Effects of CC's uncertainties and polarisation's systematic uncertainties

We finally give an estimate of the effect due to a systematic shift of the polarisation measurement. Minimising the χ^2 (eq. 1.10) by taking the "true" value $\bar{P}_i$ to evaluate $\sigma^{e^-}_{obs,CC}$ and the shifted polarisation $\bar{P}_i + \delta_{add}(P)$ to compute the linear form, it is easy to show that, with $\sigma^{e^-}_{RH} = 0$, one gets the following fake RH CC

$$\delta_{syst}(a+b) = -\delta_{sys}(P)\sigma^{e^-}_{CC}\frac{1}{2}. \tag{1.17}$$

Taking $\delta_{add}(P) = \pm 0.01$, one gets $\delta_{add}(a+b) = \mp 0.25$ pb (i.e. 0.5% relative) using the previous example. This value is very close to the uncertainties estimated above. It is then important to keep the systematic uncertainty on the polarisation below 0.01.

If instead of an additive shift, a scaling shift $\bar{P}_i(1+\delta_{sca}(P))$ is used, the effect is also given by eq. 1.17.

Model dependent Limit on the RH CC

The present highest limit on the non-standard boson W_R (or W') mass has been determined by the D0 Collaboration from a peak search in the Jacobian distribution [14]. They obtain $M_{W_R} > 720$ GeV at 95 % CL. This is of course a model dependent search since it relies on Monte Carlo distributions where the W width is used for the W_R width. From the expression given in ref. [8] we estimate the limit on M_{W_R} using the measured cross section above a Q^2 threshold Q^2_{min} by simply integrating the propagators. In order to compare with the D0 result, the left and right couplings are taken to be the same and the mixing angle is neglected (i.e. $g = g'$ and $\zeta = 0$ in the notation of ref. [8]). From the [+/−] analysis discussed above, we obtain:

$$\sigma^{e^-}_{RH} < 2 \times \delta(\sigma^{e^-}_{RH}) \text{ at } 95\% \text{ CL } \Rightarrow \frac{(M^2_W + Q^2_{min})(M^2_W + s)}{(M^2_{W_R} + Q^2_{min})(M^2_{W_R} + s)} < 2 \times \frac{\delta(\sigma^{e^-}_{RH})}{\sigma^{e^-}_{CC}}\,. \tag{1.18}$$

Results are shown in fig. 1.9 for $Q^2_{min} = 1000\,\text{GeV}^2$ and various beam polarisation and luminosity values. It will be very hard to reach the D0 limit at HERA. As illustrated in this figure, to approach the D0 limit, a very high luminosity, a very high machine polarisation, a high polarisation accuracy and a complete control of all systematics are required.

However, unlike the Tevatron result, the HERA measurement will provide a model independent cross section measurement. To illustrate this point, let us take into account the W_R width [15] in eq. 1.18. We obtain

$$\int_{Q^2_{min}}^{s} \frac{(M^2_{W_R} + Q^2)^2}{((M^2_{W_R} + Q^2)^2 + \Gamma^2_{W_R} M^2_{W_R})^2} dQ^2 < \frac{2(s - Q^2_{min})}{(M^2_W + Q^2_{min})(M^2_W + s)} \times \frac{\delta(\sigma^{e^-}_{RH})}{\sigma^{e^-}_{CC}}$$

where the W width has been neglected. Using this expression, limits in the plane (Γ_{W_R}, M_{W_R}) can be computed. They are shown in fig. 1.10 where the uncertainty on the polarisation measurement is neglected. Values of Γ_{W_R} as large as 200 GeV will not

change significantly the limits on M_{W_R}. This is obviously not the case for hadron-hadron colliders.

In addition, it should be mentioned that the W's are produced in the t channel at HERA while they are produced in the s channel at the Tevatron.

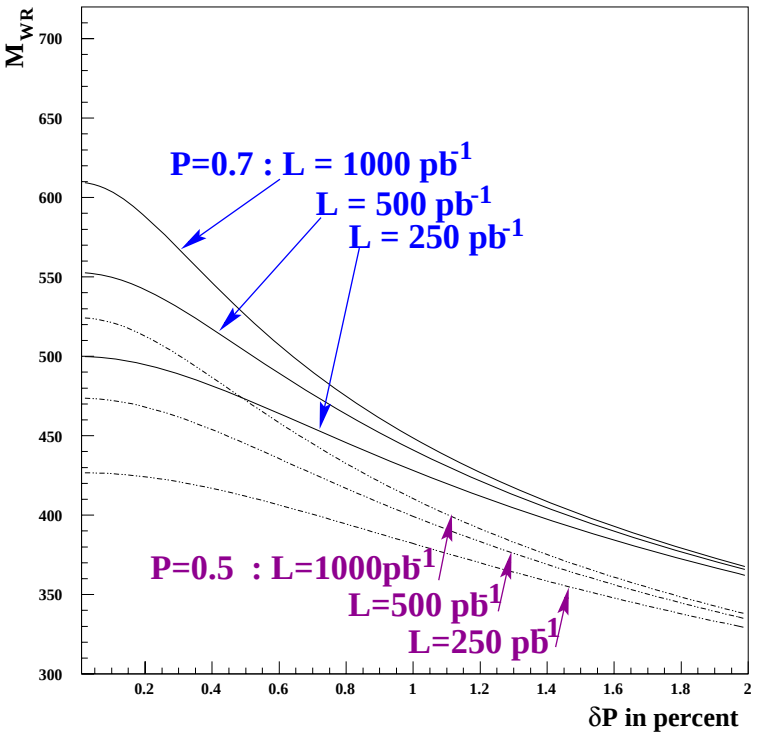

Figure 1.9: *95 % CL limits on M_{W_R} as a function of the statistical precision on the polarisation measurement for: $P = 0.7$ full curves and $P = 0.5$ dashed curves. Uncertainty on $\sigma^{e^-}_{RH}/\sigma_{SM}$ has been computed using eq. 1.8. For each group of curves, the upper one correspond to an integrated luminosity per charge samples of $1000pb^{-1}$, the middle one to $500pb^{-1}$ and the lower one to $250pb^{-1}$. Only the statistical accuracy on the CC cross section measurement has been taken into account.*

1.2 Propagation of the polarisation uncertainties to the CC cross section

The procedure of the previous section can also be used to extract the CC cross section integrated over Q^2. In practice one may be more interested in the single or double differential CC cross section. The qualitative features derived in this section should also apply to these observables.

From a statistical point of view, one can roughly estimate the required precision on the polarisation measurement by considering one data sample and a beam polarisation P:

$$\sigma^{e^-}_{obs} = \sigma^{e^-}_{CC}\frac{1-P}{2} \Rightarrow \frac{\delta\sigma^{e^-}_{CC}}{\sigma^{e^-}_{CC}} = \frac{\delta N_{obs}}{N_{obs}} \oplus \frac{\delta\mathcal{L}}{\mathcal{L}} \oplus \frac{\delta P}{1-P} ,$$

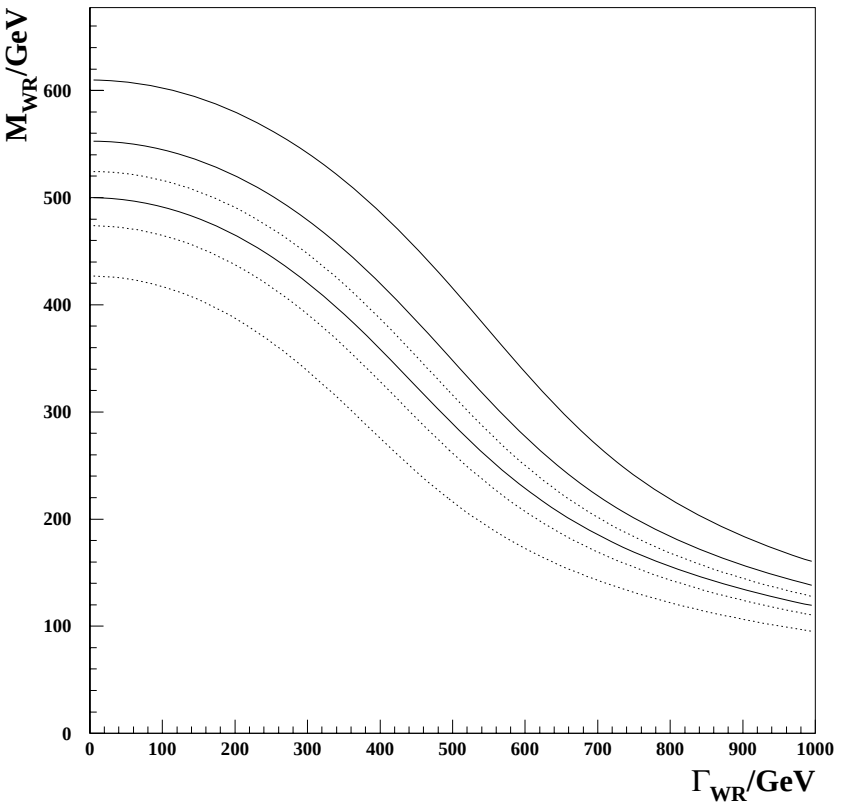

Figure 1.10: *95 CL limits in the plane* (Γ_{W_R}, M_{W_R}). *The six curves correspond to the six experimental conditions of fig. 1.9. Uncertainty on the polarisation measurement are neglected for this plot.*

which requires, taking the same numbers as in section 1.1.1, $\delta P < 1\%$.

Concerning the fit procedure, there are two possibilities:

- A two-parameters fit (see fig. 1.5) leading to $\sigma_{CC} = -a + b$. The derivative vector is here $\overrightarrow{\partial}\Sigma = (-1, 1)$ (see eq. 1.11).
- A one-parameter fit constraining $b = -a$ leading to $\sigma_{CC} = -2a \equiv 2b$. In this case one has $\delta\sigma_{CC} = 2/\sqrt{\partial^2\chi^2/\partial^2 a}$.

Effects of CC's uncertainties only

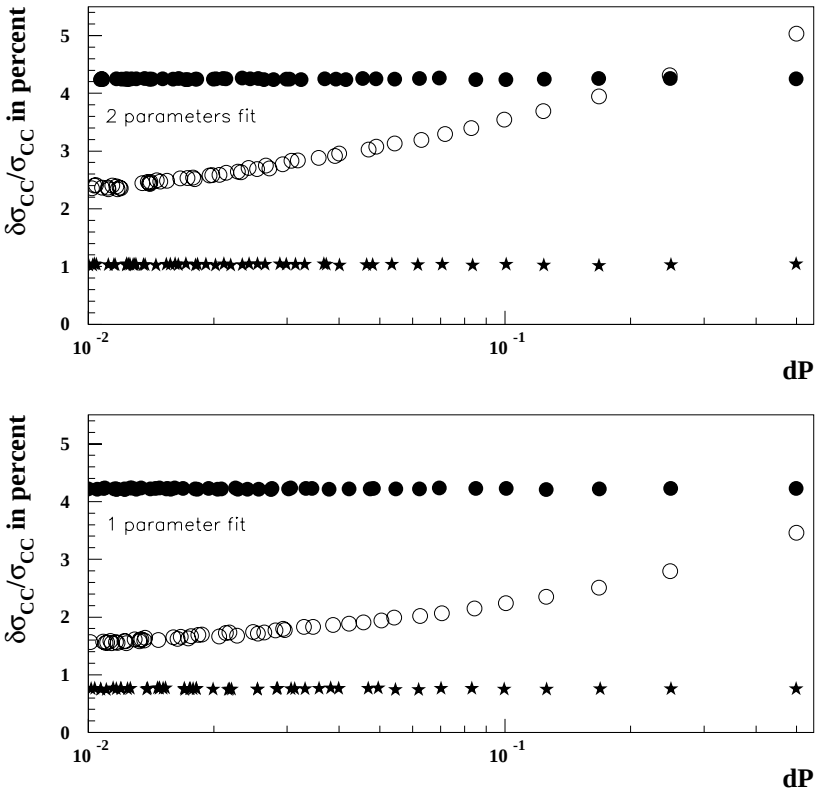

Figure 1.11: *Same as fig. 1.7 but for the CC cross section measurement. The results of the one parameter fit (see text) are shown in the bottom plot and the top plot shows the results of the two parameters fit.*

The numerical estimates of the previous section are repeated for these two new fits. Conclusions are the same as in the RH CC case (see section 1.1.2).

The bias obtained by neglecting the non-diagonal terms in the covariance matrix is also shown in fig. 1.11 for the two fits. Here $\delta(\sigma_{CC})$ is underestimated but the polarisation bin width influence is still overestimated. The statistical uncertainty contribution to $\delta(\sigma_{CC})$ is also shown and one can verify that the systematic uncertainty is effectively $\approx 4\% \oplus 1\% = \epsilon_{sca} \oplus \epsilon_{add}$.

Effects of CC's uncertainties and polarisation's uncertainties

As in the previous section, effects due to a systematic shift of the polarisation are estimated. For the two parameters fit one gets the same formula as eq. 1.17 but with an opposite sign. For the one parameter fit one gets

$$\delta_{add}(a) = -\sigma^{e^-}_{CC}\delta_{add}(P)\frac{\sum_{i,j}(1-\bar{P}_i)W_{ij}}{\sum_{i,j}(1-\bar{P}_i)(1-\bar{P}_j)W_{ij}} \tag{1.19}$$

$$\delta_{sca}(a) = -\sigma^{e^-}_{CC}\delta_{sca}(P)\frac{\sum_{i,j}(1-\bar{P}_i)\bar{P}_jW_{ij}}{\sum_{i,j}(1-\bar{P}_i)(1-\bar{P}_j)W_{ij}} \tag{1.20}$$

For a given polarisation shift and for the two analyses [+/−] and [−], the ratios on the right hand side of eq. 1.19 and 1.20 are of the order of 1/2 (same as in eq. 1.17). For the analysis [+], these factors reach ≈ 2 and ≈ 1 in eq. 1.19 and 1.20 respectively.

It is then also necessary to keep the systematic uncertainties of the polarisation below the percent level to enable a meaningful CC cross section measurement.

1.3 The neutral currents case: effect of the polarisation rise

Neutral Current (NC) measurements at high Q^2 permit the determination of the quark couplings to the Z^0 [3, 16, 17]:

$$a_q = I_3^q \text{ and } v_q = I_3^q - 2e_q \sin^2\theta_W$$

where I_3^q is the third component of the weak isospin of the quark flavour q. As usual we shall only distinguish the U (= u, c) and down D (= s, c, b) type of quarks so that $q = U$ or D in the above equation. Since the u and d contribution dominates at high Q^2 at HERA, the determination of $a_{U,D}$ and $v_{U,D}$ is complementary to the results of LEP heavy flavour measurements.

The NC cross section $d^2\sigma/dxdQ^2$ depends on the lepton charge and on the polarisation at high Q^2. Its expression is lengthy and can be found in ref. [18, 19]. We shall follow the work described in this article but in a much more simplified form. The reason is that we are looking at the gain of an analysis performed in bins of polarisation with respect to the same analysis performed with only two polarisation states $\pm|P|$. Our simplified procedure is the following

- the Born cross-section is used to compute $d^2\sigma/dxdQ^2$ (= no Monte Carlo generation is performed) for $Q^2 > 1000$ GeV^2
- the x and Q^2 bins of [10] are chosen so that the statistical error is estimated (by mean of the average theorem) to be

  $$\delta_{stat}(d^2\sigma) = \sqrt{\frac{d^2\sigma}{\mathcal{L}\Delta_x\Delta_{Q^2}}}$$

  where $d^2\sigma$ stands for $d^2\sigma/dxdQ^2$; Δ_x and Δ_{Q^2} are the bin widths and x ($x = 0.02, ..., 0.65$) and Q^2 ($Q^2 = 1000, ..., 30000$ GeV^2) the bin centres.

- A χ^2 is computed: $\chi^2 = \chi^2_{e^+} + \chi^2_{e^-}$ with

$$\chi^2_{e^\pm} = \sum_{i,x,Q^2} \frac{[d^2\sigma^{e^\pm}(\bar{P}_i; \delta a_q, \delta v_q) - d^2\sigma^{e^\pm}_{SM}(\bar{P}_i)]^2}{[\delta_{stat}(d^2\sigma^{e^\pm})]^2} \tag{1.21}$$

and $q = U, D$. In eq. 1.21 the "measurement" is $d^2\sigma^{e^\pm}_{SM}(\bar{P}_i)$ and the "theory" is $d^2\sigma^{e^\pm}(\bar{P}_i; \delta a_q, \delta v_q)$. The unknown parameters δa_U, δa_D, δv_U and δv_D are defined by

$$a_q = a_{q,SM} + \delta a_q \quad , \quad v_q = v_{q,SM} + \delta v_q$$

where the subscript SM stands for Standard Model. Here $d^2\sigma_{SM}$ is the "measurement" (i.e. $\delta a_q = 0$ and $\delta v_q = 0$) so that $\chi^2 = 0$ when the fit parameters vanish since the "measurements" are not smeared (we checked that applying a Gaussian smearing doesn't change the results).

As in the previous section we define a polarisation binning. We have considered, as in [19] an integrated luminosity of 250 pb^{-1} per type of beam and per polarisation sign. Taking $P = 0.7, 0.5$ and fixing a_U v_U (a_D and v_D fixed) we obtain, using MINUIT, the 1 σ contour plot shown in fig. 1.12. It is astonishingly close to the result of ref. [19] which includes electroweak higher order effects and detector simulation. The same kind of agreement is obtained for a_D and v_D (a_U and v_U fixed) and for the fit where the four couplings are free.

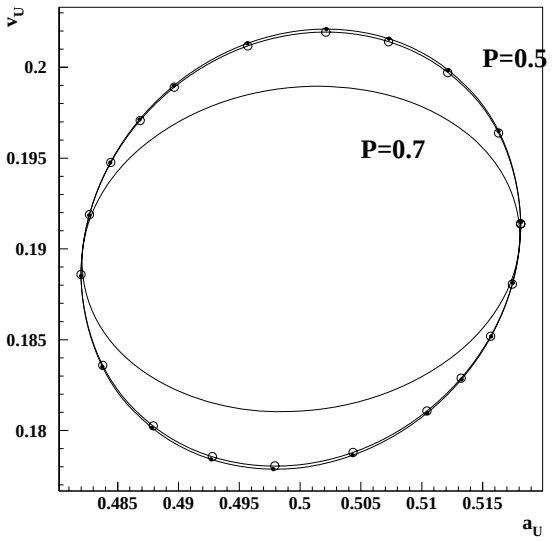

Figure 1.12: *1σ contour plot for v_U, a_U (v_D, a_D fixed) and $P_\infty = 0.7$ (inner curve), $P_\infty = 0.5$ (outer curves). The full dots indicate the result obtained with four data samples $e^\pm_{\pm|P|}$ and the open circles show the results obtained using the same data samples but in bins of polarisation (10 bins of width 0.05). As in ref. [3] (p. 185), we have considered 250 pb^{-1} for each data samples.*

As a result, when the four data samples $e^{\pm}_{\pm|P|}$ are included in the fit we find no significant differences between the fit with or without polarisation binning (see fig. 1.12). Even with a fine binning such $dP = 0.01$.

We have finally studied the effect of a systematic uncertainty on the polarisation measurement: in eq. 1.21 the "true" polarisation $\bar{P}_i$ is used to compute $d^2\sigma_{SM}(\bar{P}_i)$ and it is shifted by $\delta_{sys}(P)$ to compute $d^2\sigma$. Then the fit is repeated. The resulting shifts of the couplings are shown in figs. 1.13 and 1.14 for $\delta_{sys}(P) = \pm 0.01$ and ± 0.02. From these figures we conclude that it is crucial to control any systematic uncertainties at a level below 0.01. This is particularly important for the up quark couplings since the future HERA-II measurement will provide a precision comparable with LEP [20] as shown in fig. 1.15. In addition, the HERA-II and LEP measurements are complementary since the couplings to the heavy quarks c and b are determined at LEP.

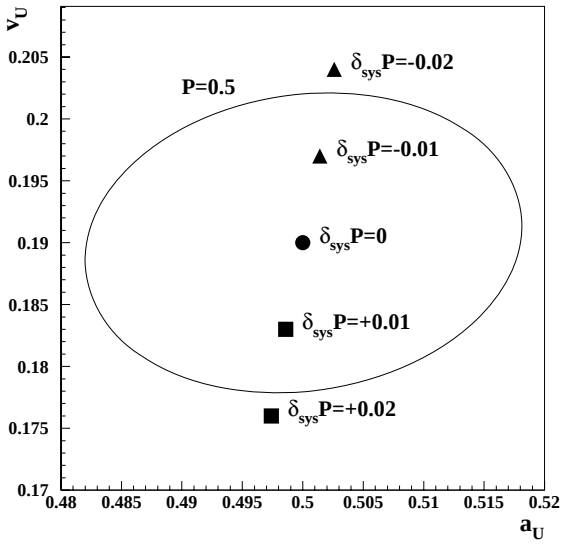

Figure 1.13: *The full curve shows the 1σ contour plot for v_U, a_U (v_D, a_D fixed) and $P = 0.5$ assuming a perfect polarisation measurement . The points show the ellipse centre shift observed when the polarisation is shifted by the values indicated on the plot. We have taken 250 pb^{-1} for each of the four data samples $e^{\pm}_{\pm|P|}$. The uncorrelated systematic uncertainties are not taken into account.*

1.4 Summary

The precision required for the polarisation measurement at HERA-II has been estimated for three topics, the RH CC, the CC cross section measurement and the extraction of the quark electroweak couplings. As a result a statistical precision and a systematic precision better than 0.01 (absolute) are needed.

We have shown that with only one beam charge and polarisation data sample, $e^{-}_{-|P|}$ or $e^{-}_{+|P|}$, the smaller the polarisation bin width, the better the statistical uncertainty on

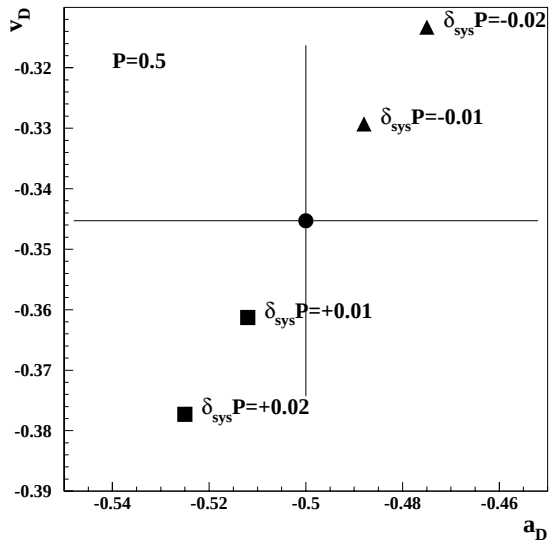

Figure 1.14: *The error bars show v_D, a_D (v_U, a_U fixed) obtained by the fit with $P = 0.5$ and a perfect polarisation measurement. The points show the central value shift observed when the polarisation is shifted by the values indicated on the plot. We have taken 250 pb^{-1} for each of the four data samples $e^{\pm}_{\pm|P|}$. The uncorrelated systematic uncertainties are not taken into account.*

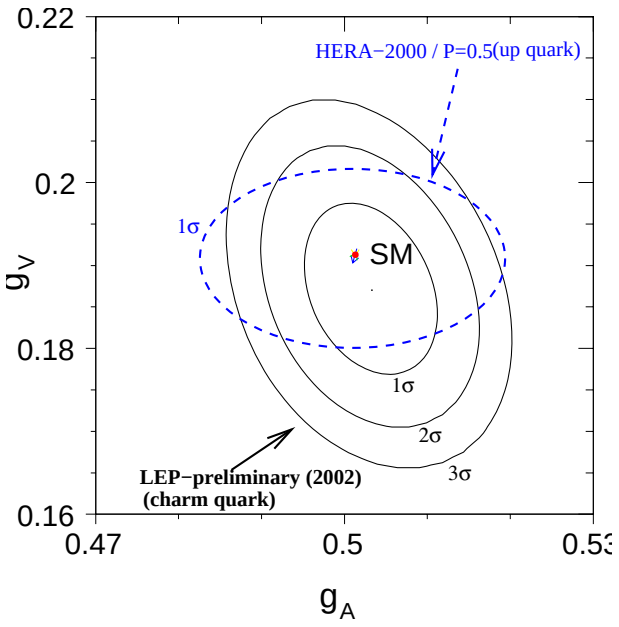

Figure 1.15: *Same as fig. 1.12 with the latest LEP results.*

the measurements of RH CC and CC cross sections. To some extent these features also apply for the electroweak coupling determination.

Let us stress that throughout this chapter we have assumed that the luminosity and the polarisation are uncorrelated. As it will be shown in chap. 2, this is only true when the polarisation is measured bunch by bunch within one minute approximately.

1.5 Appendix

In this appendix, an introduction to the deep-inelastic electron-proton scattering is given. This text is an updated and slightly modified version of a long proceeding written for the Ringberg Workshop on the new trends in HERA physics (1999).

1.5.1 Introduction

In the Deep Inelastic Scattering (DIS) processes observed at HERA, a lepton $\ell = e^{\pm}$ of 27.5 GeV interacts with a proton P of 920 GeV yielding a lepton ℓ' and a set of hadrons X in the final state. Following the nature of ℓ' the interaction proceeds via a neutral ($\ell' = e^{\pm}$) current (NC) or a charged ($\ell' = \nu_e, \bar{\nu}_e$) current (CC). DIS events are collected in the H1 and ZEUS experiments [21] which are located at the two $e^{\pm}P$ interaction points of HERA.

The kinematics of the DIS inclusive processes, $\ell(k) + P(p) \to \ell'(k') + X$, is determined by two independent kinematic variables, besides the energy of the incoming lepton and proton. One usually chooses them among the four Lorentz invariants[2]

$$Q^2 \equiv -q^2 = -(k - k')^2,\ x = \frac{Q^2}{2p \cdot q}\ ,\ y = \frac{p \cdot q}{p \cdot k},\ W^2 = (q + p)^2\ .$$

At HERA energies, one can neglect the lepton and proton masses so that the useful relation $Q^2 = xys$ holds. These kinematic variables are obtained experimentally by measuring the momentum and/or the hadronic energy, the direction of the scattered lepton and/or the hadronic energy flow.

In this Appendix we shall restrict ourselves to the cross section measurements at HERA in the medium 1.5 GeV$^2 \leq Q^2 <$ 150 GeV^2 and high 150 GeV$^2 \leq Q^2 \leq$ 30000 GeV^2 domains of the DIS regime. During the past, a large number of precise measurements have been performed in the medium Q^2 region by fixed target experiments [22]. With HERA, three major improvements may be noticed:

- an extension of the Q^2 domain to very high Q^2 (10^4 GeV^2) but also to very small x ($\approx 10^{-6}$) (see fig. 1.16);
- an almost hermetic (4π) detection of the final state leading to the determination of the energy and angle not only of the scattered lepton but also of the produced hadrons;
- an over constrained determination of the kinematic variable;
- from the previous items it follows that the detection of both NC and CC is feasible in the same detector and during the same data taking period;

The somewhat arbitrary distinction between medium and high Q^2 is related to different physics interests. In both regions perturbative Quantum-Chromo-Dynamics (pQCD) describe the HERA data [26, 27]. The pQCD analysis of medium Q^2 data is part of a long

[2] In the so called 'naive quark' model, x is the proton momentum fraction carried by the struck quark. In the reference frame where the proton is at rest, y is the inelasticity (=fraction of the incident electron energy transfered to the proton). W is the invariant mass of the final state hadronic system X.

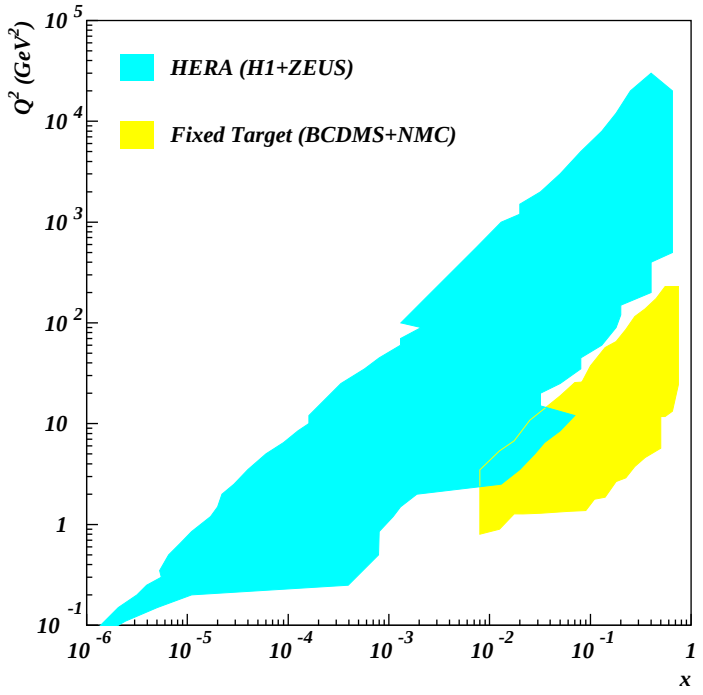

Figure 1.16: *Comparison of the HERA and fixed target kinematic domains. From [23]*

tradition [30] from which the parton distributions of the nucleon and the strong coupling constant α_s have been extracted. On top of that, very high Q^2 ($\approx M_Z^2$) NC and CC data open a field of research in electroweak physics.

The rest of this appendix is organized as follows. In section 1.5.2 the measurements of NC and CC differential cross sections are described. Section 1.5.3 is devoted to a phenomenological analysis of these measurements.

1.5.2 Measurement of NC and CC cross sections

Neutral current events, at medium and high Q^2, are basically identified by the presence of an electron (or a positron) in the final state. This is done by using tracking and calorimetric devices covering the range $7^o < \theta_e < 177^o$ and E'_e >4 GeV(at HERA the forward direction $\theta_e = 0^o$ corresponds to the direction of the incoming proton).

The differential cross section measurement is done by counting the number of events within a kinematic interval in, say x and Q^2. Therefore one of the experimental problems is to achieve a good reconstruction of these kinematic variables from the detector information. Both H1 and ZEUS, can use the outgoing lepton and hadronic final state information, namely polar angles, momenta and deposited energies. It is then possible to define the kinematics of each event by using different (and independent) combinations of experimental information.

In ZEUS the double angle method [24] is used

$$Q^2_{da} = 4E_e^2 \frac{\sin\gamma_h(1+\cos\theta_e)}{\sin\gamma_h + \sin\theta_e - \sin(\gamma_h+\theta_e)}, \quad y_{da} = \frac{\sin\theta_e(1-\cos\gamma_h)}{\sin\gamma_h + \sin\theta_e - \sin(\gamma_h+\theta_e)}$$
$$x_{da} = \frac{E_e}{E_p}\frac{\sin\gamma_h + \sin\theta_e + \sin(\gamma_h+\theta_e)}{\sin\gamma_h + \sin\theta_e - \sin(\gamma_h+\theta_e)}.$$

The hadronic polar angle γ_h is defined by $\tan\gamma_h/2 = \sum_i (E_i - p_{z,i})/P_{t,h}$, where E_i and $p_{z,i}$ are the energy and longitudinal momentum of the final state hadron i and where $P_{t,h}$ is the total transverse momentum of the hadronic final state particles.

Since $dx/x = 1/y d\dot{E}'_e/E'_e$, the electron method is used in H1 to determine Q^2 and x:

$$Q^2_e = \frac{(E'_e)^2\sin^2\theta_e}{1-y_e}, \quad y_e = 1 - \frac{E'_e}{E_e}\sin^2(\theta_e/2)$$

for $y > 0.15$, while for $y \leq 0.15$ the Σ method [25] is used

$$Q^2_\Sigma = \frac{(E'_e)^2\sin^2\theta_e}{1-y_\Sigma}, \quad y_\Sigma = \frac{\sum_i (E_i - p_{z,i})}{\sum_i (E_i - p_{z,i}) + E'_e(1-\cos\theta_e)}.$$

The reason for the differences between the methods used by H1 and ZEUS are related to the calorimeter performances: H1 possesses finely segmented electro-magnetic calorimeters and ZEUS a very good hadronic calorimetry.

The redundancy in the determination of the kinematic variables is a crucial point and presents many advantages: minimization of the migration between the 'true' and the measured kinematic variable by choosing one particular method; cross calibration of the various calorimeter devices, and studies of photon radiation from the lepton line by comparing leptonic and hadronic information.

Once the collected events are gathered in x-Q^2 bins, besides the subtraction of photoproduction background, correction factors are applied for: the efficiency of the event selection; detector acceptance; wrong reconstruction of the kinematics due to detector effects, and the contribution of higher order electroweak processes. When possible, these correction factors are determined and/or cross checked from the data themselves. If this is not possible, then they are determined from a full simulation of the DIS and background processes including the detector response.

For the medium Q^2 data we shall describe the results of the high statistics 1996-1997 data analysis [26]. For high Q^2, $e^\pm$ beam data published in ref. [27] will be presented.

At medium Q^2 and for the H1 measurements, the main systematic uncertainties are: the electron energy scale ($\approx 0.3\%$), the hadronic energy scale ($\approx 2-3\%$), the electron polar angle (≈ 0.3 mrad), the photoproduction background at high-y only ($\approx 3\%$ effect on the measurements) and the correction factors (see above) applied to the data (each one is of the order of 1-2%). The overall data normalization (including the luminosity measurement) uncertainty is 1.5 %. The systematic uncertainty is, in total, of the order of 3% and is larger than the statistical uncertainties which are at the level of 1 % for $Q^2 < 100$ GeV^2.

At high Q^2 the systematic uncertainties are similar. In ZEUS the statistic and systematic uncertainties amount to 3-5% for the kinematic range 400 GeV^2 $< Q^2 <$ 30000 GeV^2 considered in the analysis.

In charged current (CC) events, the outgoing neutrino escapes the detection. Such events are then characterized by missing transverse energy $p_{t,miss}$ (the analysis cut is $p_{t,miss} > 12$ GeV).

For the reconstruction of the kinematic variables, one can only use information from the hadronic final state, i.e. the Jacquet-Blondel method [28], giving,

$$y_{JB} = \frac{\sum_i (E_i - p_{z,i})}{2E_e}, \;\; Q^2_{JB} = \frac{p^2_{t,miss}}{1 - y_{JB}} \, .$$

The CC event statistics is still low, ≈ 900 events for $Q^2 > 400$ GeV^2 in ZEUS (and similar numbers for H1). However the systematic uncertainty, for both experiments, is dominated by the hadronic energy scale, which induces an effect of the order of 10%, except at very high Q^2 and very high x where the effect is above 20%. Other systematic sources related to the $p_{t,miss}$ cut, acceptance correction and photoproduction background subtraction (in the lowest Q^2 bins) lead to measurement uncertainties between 4% and 8%.

1.5.3 Phenomenological analysis of inclusive measurements at HERA

As mentioned in the introduction, we shall distinguish the phenomenological analysis of the medium Q^2 data from the high Q^2 data. As we are interested in the HERA data, it should be noted that we are considering the region of large $W^2 \gg 10$ GeV^2. Therefore, we will not be concerned by the non-perturbative effects and the higher twist effects appearing in the small W^2 region so that the symbol pQCD, appearing below, refers to the leading twist of pQCD.

For all the mathematical details which cannot be given here we refer to ref. [29] and references therein.

Analysis of the medium Q^2 NC data

In the one boson exchange approximation, the NC differential cross section reads

$$\frac{d\sigma^{e^\pm p}}{dxdQ^2} = \frac{2\pi\alpha_{em} Y_+}{xQ^4}\sigma_r, \;\; \sigma_r = F_2(x,Q^2) - \frac{y^2}{Y_+}F_L(x,Q^2) \mp \frac{Y_-}{Y_+}xF_3(x,Q^2)\,, \qquad (1.22)$$

where $Y_\pm = 1 \pm (1-y)^2$. The nucleon structure functions are modelled using the quark-parton model and pQCD. In the so called naive parton model one writes

$$F_2(x) = \sum_{i=1}^{n_f} A_i(Q^2) x[q_i(x) + \bar{q}_i(x)]\,, \; F_3(x) = \sum_{i=1}^{n_f} B_i(Q^2)[q_i(x) - \bar{q}_i(x)]$$

where q_i ($\bar{q}_i$)is the density function of the quark (anti-quark) of flavor i, n_f is the number of active flavors and $F_L = 0$ in the quark parton model. The functions A_i [18, 30] depend on the electric charge e_i ($A_i = e_i^2$ for $Q^2 \ll M_Z^2$) and embody the effects of the Z exchange and $\gamma - Z$ interference in their Q^2 dependence. The same holds for the functions B_i [30] except that they vanish at $Q^2 \ll M_Z^2$.

Going beyond the simple parton model, higher order contributions in α_s are taken into account. In doing so, mass singularities appear in the initial state of DIS processes

and cannot be regularised without resumming the whole perturbative series. This resummation is done in a restricted kinematic region where $\alpha_s \log Q^2$ is large [29]. This latter region is defined by $Q^2 \gg \Lambda^2 \approx 0.3^2$ GeV^2, and the pCDQ calculations are safe for Q^2 above a few GeV^2. In this domain, the parton density functions (pdf) are given by the solution of the DGLAP equations [29]:

$$\begin{aligned} M_F \frac{\partial q^{\pm}_{i,NS}(x, M_F^2)}{\partial M_F} &= P^{\pm}_{NS} \otimes q^{\pm}_{i,NS}(x, M_F^2) \\ M_F \frac{\partial}{\partial M_F} \begin{pmatrix} \Sigma(x, M_F^2) \\ g(x, M_F^2) \end{pmatrix} &= \begin{pmatrix} P_{qq} & n_f P_{qg} \\ P_{gq} & P_{gg} \end{pmatrix} \otimes \begin{pmatrix} \Sigma(x, M_F^2) \\ g(x, M_F^2) \end{pmatrix} \end{aligned} \tag{1.23}$$

with $A \otimes B \equiv \int_x^1 A(z)B(x/z)dz/z$ and where $\Sigma = \sum_{i=1}^{n_f}(q_i + \bar{q}_i)$ is the singlet quark density, $q^-_{i,NS} = q^v_i \equiv q_i - \bar{q}_i$ and $q^+_{i,NS} = q_i + \bar{q}_i - \Sigma/n_f$ are the two non singlet densities and g is the gluon density. The splitting functions $P_{i,j} = \alpha_s(M_R^2)P^{(0)}_{i,j} + \alpha_s^2(M_R^2)P^{(1)}_{i,j}$ describe the branching of parton j from parton i, and they can be computed with pQCD up to the second order. In eq. (1.23) M_F is the factorization scale (below which the mass singularity is resummed) and M_R is the renormalisation scale (related to the ultra-violet singularity). As the two scales must be chosen somehow arbitrarily, a natural choice for M_F is $\sqrt{Q^2}$, i.e. the virtual mass of the probe. We shall, as usual, also set $M_R = M_F$ for convenience. It is worth mentioning that the DGLAP equations are universal, i.e. that they are independent of the specific hard process.

Eq. (1.23) embodies the mass singularity resummation and therefore it only describes the so called light parton, i.e. the parton of flavour i and mass m_i such that $m_i^2/Q^2 \ll 1$. In the medium Q^2 range one can take the gluon, the up, down and strange quarks as the light partons. For the heavy quarks (charm and beauty) one needs to specify a particular scheme. We have chosen the fixed-flavor-scheme (FFS) [31] – suitable in the HERA medium Q^2 range – where beauty is neglected, and where the charm contribution is computed from the boson-gluon-fusion process $\gamma g \to c\bar{c}$ plus the α_s^2 corrections. In this scheme charm is produced 'outside' the hadron. The relation between the pdfs and the structure functions depends on the renormalisation scheme. In Next-to-Leading-Log-Approximation (NLLA) and in the $\overline{\text{MS}}$ scheme one ontains:

$$\begin{aligned} F_i(x, Q^2) =& x \sum_{j=1}^{n_f} \left[\left(1 + \frac{\alpha_s(Q^2)}{2\pi} C_{j,q} \right) \otimes e_j^2 (q_j(x, Q^2) + \bar{q}_j(x, Q^2)) \right. \\ & \left. + 2 \frac{\alpha_s(Q^2)}{2\pi} C_{j,g} \otimes g \right] + F_i^{c\bar{c}}(x, Q^2) \end{aligned}$$

for $n_f = 3$ and where $i = 1, 2$ (there is a similar expression for F_3 with $F_3^{c\bar{c}} = 0$); $C_{j,q}$ and $C_{j,g}$ are the coefficient functions depending on the hard process; $F_i^{c\bar{c}}$ is the charm contribution [32]. It suffices here to say that it depends on m_c^2 and on a renormalisation scale that we choose to be $\sqrt{m_c^2 + Q^2}$. Note that $F_L = F_2 - 2xF_1 \neq 0$ in the NLLA.

To solve the system of integro-differential equations (1.23), one must provide some initial conditions, i.e. some input functions of x at a given Q^2 for each pdf. Since these functions reflect some unknown non-perturbative mechanism, they must be parameterized with the help of a set of parameters. As we shall see below, these parameters are determined by comparing the calculations to the experimental data.

Concerning the data-theory comparison, from which the input pdfs have to be determined, both H1 and ZEUS use a χ^2 minimization procedure. The main steps of the fitting procedure are summarized below. For each iteration:

1. the pdfs are parameterized at a given value of Q^2 denoted Q_0^2, chosen to be 7 GeV^2 in the ZEUS fit and 4 GeV^2 in the H1 fit,

2. the DGLAP equations are solved numerically in the x-space [33].

3. the evolved pdf's are convoluted with the coefficient functions to obtain the structure functions.

4. Assuming that all experimental uncertainties are normally distributed a χ^2 is computed. A crucial point of the analysis is the χ^2 expression which permits the use of the correlations introduced by some of the systematic uncertainties. Details can be found in ref. [9].

Further details on the fit can be found in the H1 publication of ref. [26]. The result of the H1 fit is shown in fig. 1.17 together with the data. The agreement between data and pQCD is excellent. The gluon density obtained from this fit is shown in fig. 1.18. The error bands of the gluon density include the experimental error propagation as defined in ref. [9] and a theoretical uncertainty which includes the variation of all the fit ingredients (charm mass, Q_0^2, data rejection cuts, parameterisation forms, α_s, experimental error treatement). The theoretical uncertainties are now dominating the determination of gluon momentum xg, i.e. the third order splitting functions are needed.

Analysis of the high Q^2 NC and CC data

The fits applied to the high Q^2 data differ from the one described in the previous section by a different calculation of the contribution of the heavy quarks to the structure functions. As $m_c \approx 1.5$ GeV, one has $m_c/Q^2 \ll 1$ at high Q^2. The large term $\alpha_s^n \log^n(Q^2/m_c^2)$ – dominating the calculation of $F_2^{c\bar{c}}$ – must be resummed already at $Q^2 \approx 20$ GeV^2. The massless scheme is therefore used and only data with $Q^2 \geq 10$ GeV^2 are included in the fit [3]. In the massless scheme, charm and beauty are considered as partonic constituents of the proton and their density functions are obtained by solving the DGLAP equations with the initial conditions $c(x, Q^2 \leq m_c^2) = 0$ and $b(x, Q^2 \leq m_b^2) = 0$. Such fits describe the HERA NC and CC (see figs. 1.19 and 1.21) data above $Q^2 = 10$ GeV^2.

In fig. 1.19 one can observe the different behavior of e^-p and e^+p cross sections at very high Q^2. This is related to the different sign of the contributions of F_3 to σ_r. Fig. 1.20 shows $d\sigma/dx$ together with the results of two pQCD fits including or not the Z exchange and $\gamma - Z$ interference. With the present data, sensitivity to electroweak effects in NC is for the first time observed at HERA.

Up to now we have only described the NC cross sections and related structure functions. For CC processes, in the one boson exchange approximation, one has

$$\frac{d\sigma_{CC}^{e^\pm p}}{dxdQ^2} = \frac{G_F^2}{2\pi x} \frac{M_W^4}{(M_W^2 + Q^2)^2} \Phi_\pm(x, Q^2), \tag{1.24}$$

[3] This Q^2 threshold is indicative and it can been lowered

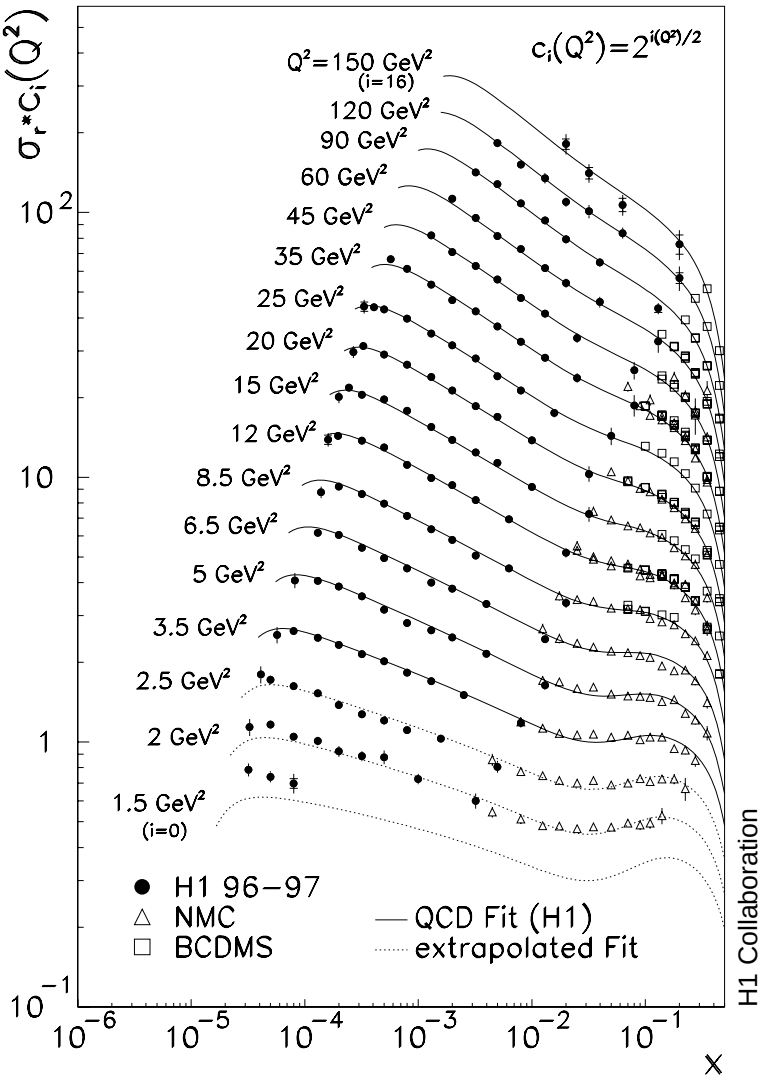

Figure 1.17: *H1 measurements of σ_r together with the result of a pQCD fit (see text). The dotted lines describe the fit result extrapolated in the region where the data are exculded from the fit (i.e. $Q^2 \leq 2.5$ GeV^2).*

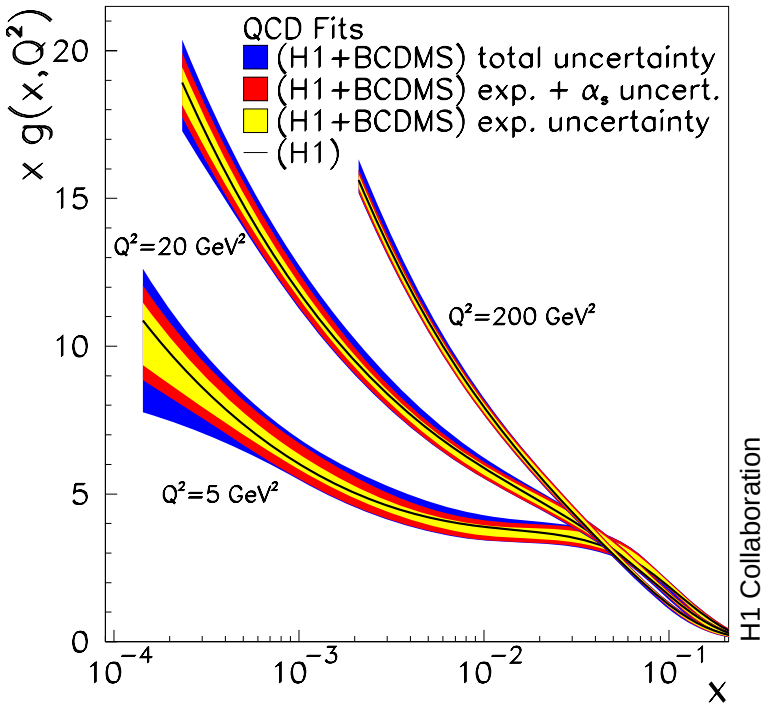

Figure 1.18: *xg extracted from the H1 fits.*

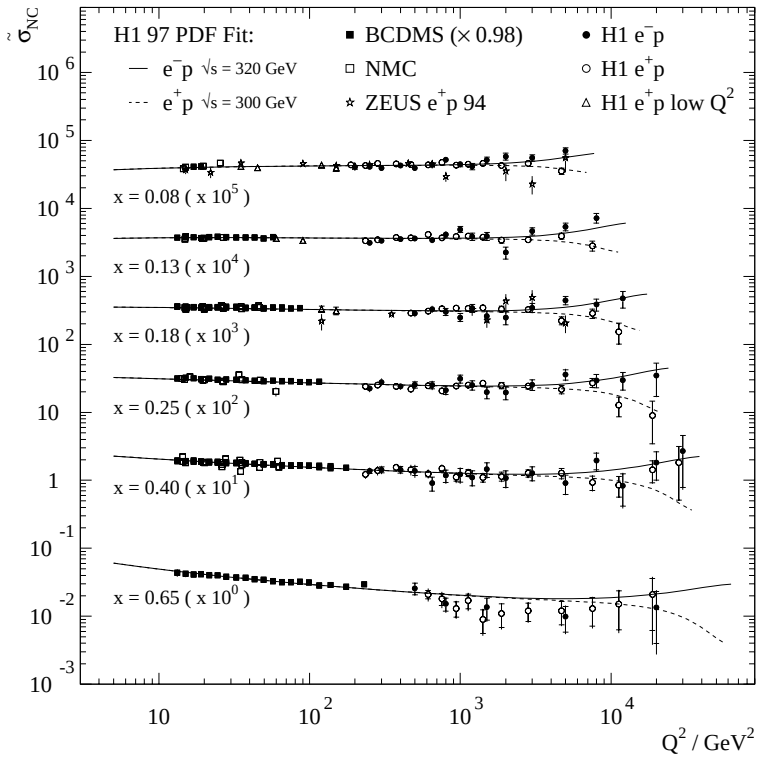

Figure 1.19: *High Q^2 H1 measurements of $\tilde{\sigma} \equiv \sigma_r$ (eq. 1.22) compared with pQCD fit results (see text).*

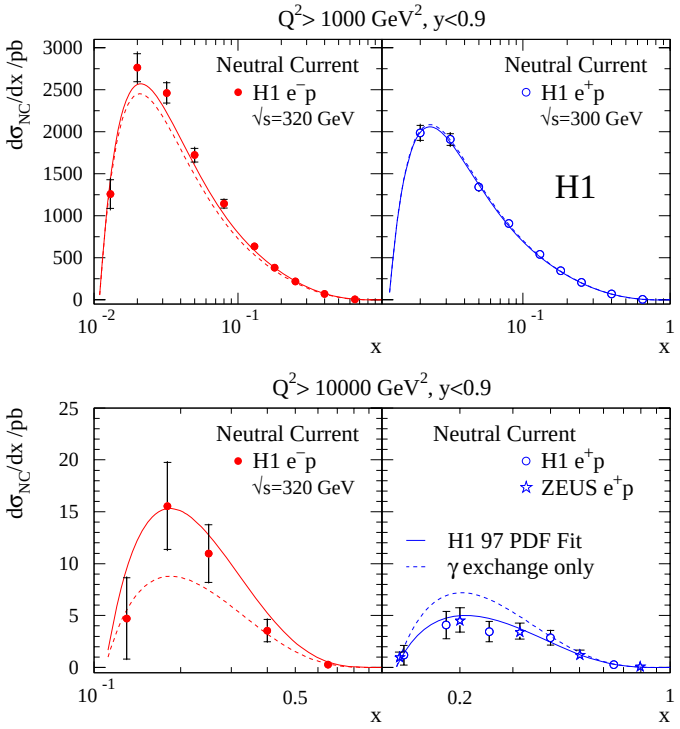

Figure 1.20: *H1 measurements of $d\sigma^{NC}/dx$ together with results from pQCD fits and different assumptions on electroweak contributions.*

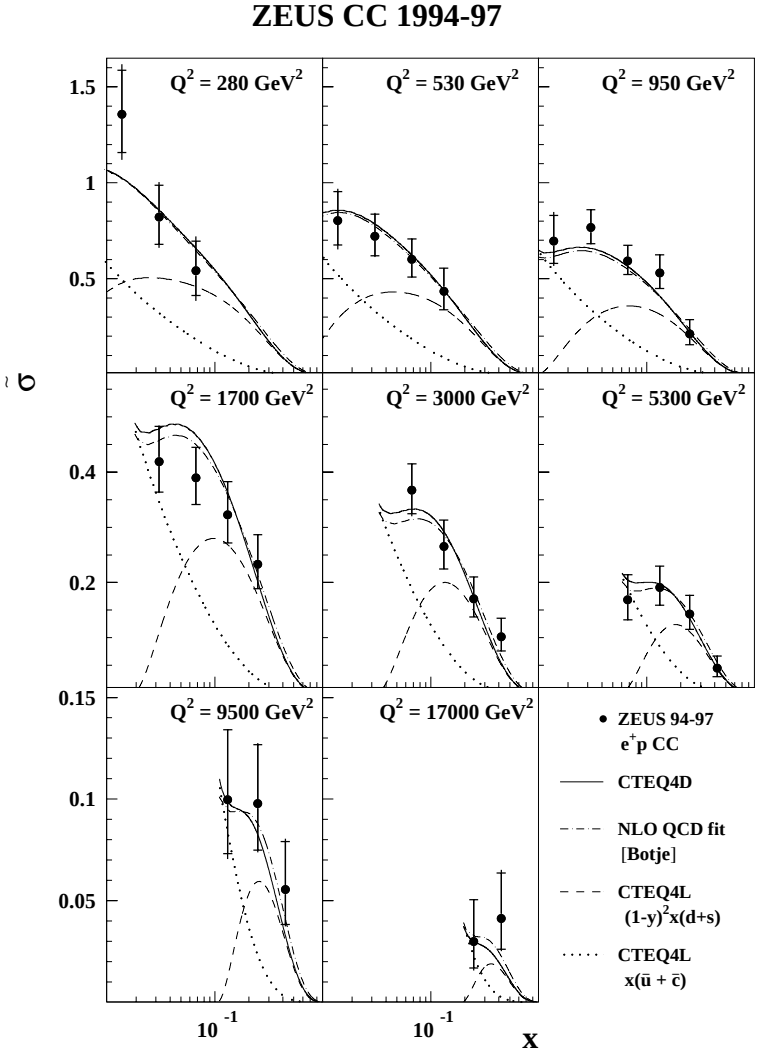

Figure 1.21: *ZEUS measurements of* $\tilde{\sigma} \equiv \Phi_+$ *together with various pQCD calculations (see text).*

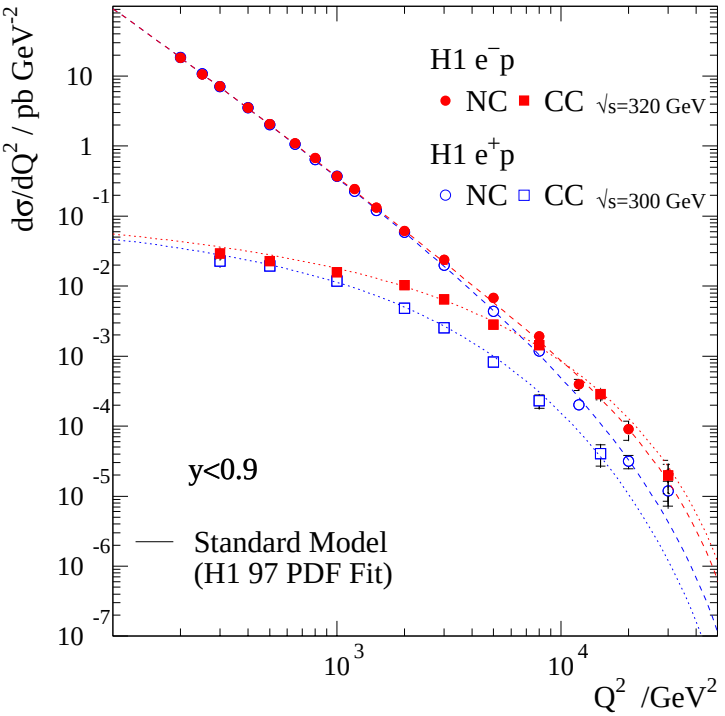

Figure 1.22: *H1 measurements of $d\sigma^{CC}/dQ^2$ and $d\sigma^{NC}/dQ^2$ together with the pQCD fit results.*

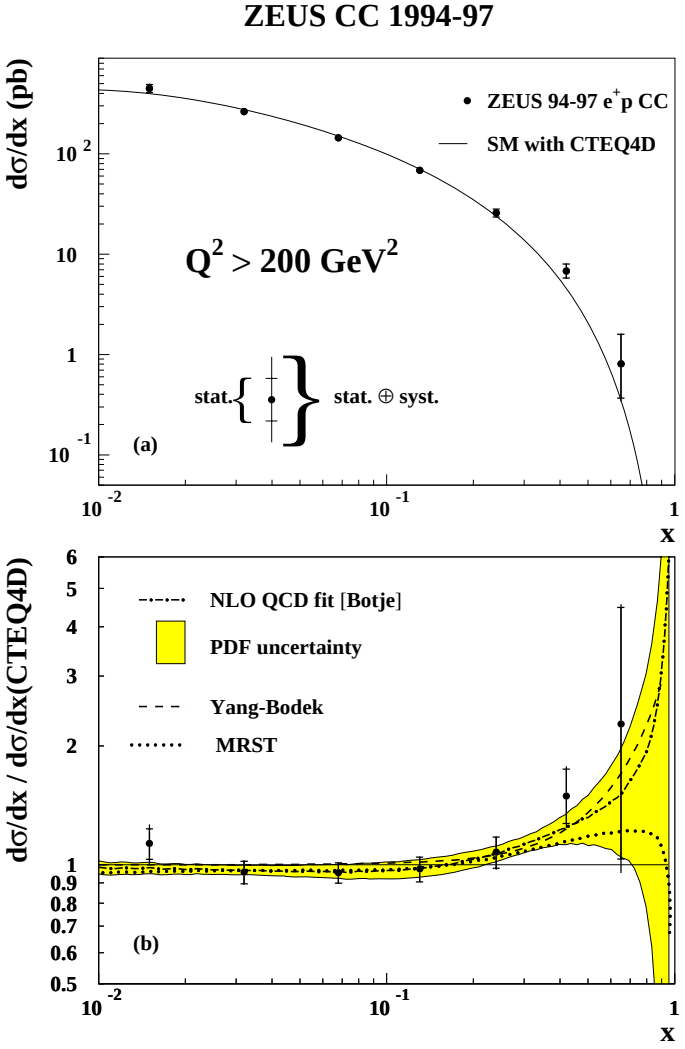

Figure 1.23: *ZEUS measurements of $d\sigma^{CC}/dx$ (for e^+p) together with various pQCD results (see text).*

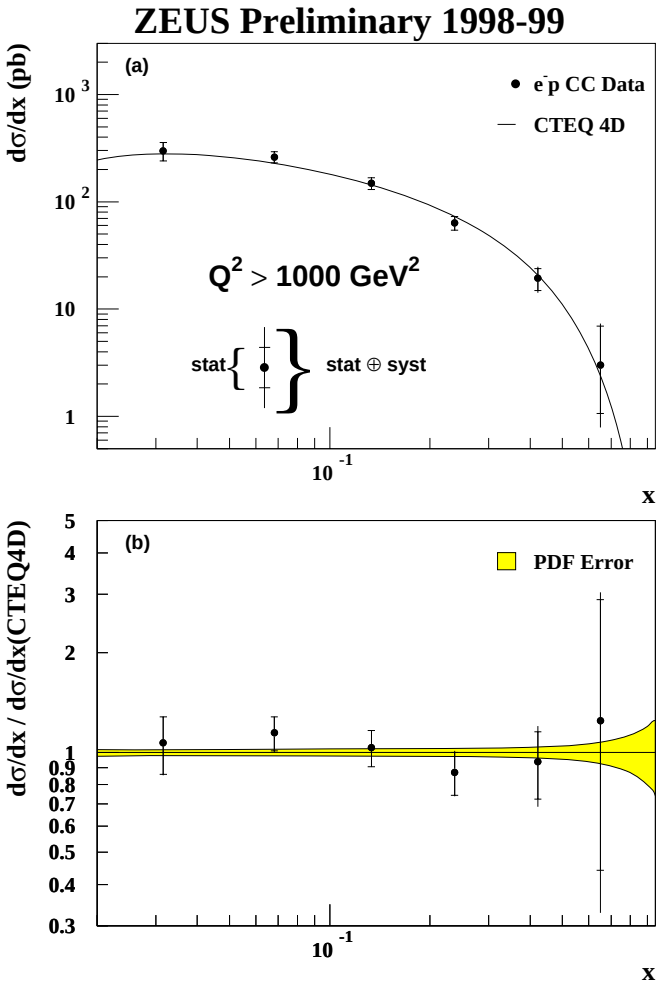

Figure 1.24: *ZEUS measurements of* $d\sigma^{CC}/dx$ *(for* e^-p*) together with the pQCD fit result.*

where G_F is the Fermi constant, and where the functions $\Phi_\pm$ depends on CC structure functions (see [30] for example). From eq. (1.24) one can first remark that the Q^2 slope of the CC differential cross section (see fig. 1.22) permits a determination of M_W, assuming (or not) the precisely measured value for G_F [34]. To extract M_W, H1 and ZEUS have used two different procedures. In H1, M_W is taken as an extra free parameter (G_F is fixed) of the pQCD fit and in ZEUS, the pdfs of CTEQ [35] are used in order to extract M_W and G_F (variations of the pdf choice is taken into account within the errors). The results are

$$\begin{aligned} \text{H1} : \mathrm{M_W} &= 80.9 \pm 3.3(stat.) \pm 1.7(syst.) \pm 3.7(theo)\,\mathrm{GeV} \\ \text{ZEUS} : \mathrm{M_W} &= 80.4^{+4.9}_{-2.6}(stat.)^{+2.7}_{-2.0}(syst.)^{+3.3}_{-3.0}(pdf)\,\mathrm{GeV} \end{aligned}$$

and treating G_F as free, ZEUS obtain

$$\begin{aligned} M_W &= 80.8^{+4.9}_{-4.5}(stat.)^{+5.0}_{-4.3}(syst.)^{+1.4}_{-1.3}(pdf)\,\mathrm{GeV}, \\ G_F &= [1.171 \pm 0.034(stat.)^{+0.026}_{-0.032}(syst.)^{+0.016}_{-0.015}(pdf)] \times 5 \cdot 10^{-5}\,\mathrm{GeV}^{-2}. \end{aligned}$$

Let us point out that, concerning the H1 result, the theoretical uncertainty is dominated by the variation of the results when varying the ratio $\bar{d}/\bar{u}$ in the pQCD fit, and by the choice of the nuclear corrections applied to the deuterium target data entering the fit. These results, in good agreement with the world average values [34], show that the standard model gives a good description of both space-like (CC in DIS) and time-like (W production in $p\bar{p}$ and e^+e^- collisions) processes.

In order to see the sensitivity of the CC cross section to the pdfs, we write $\Phi_\pm$ in LO

$$\Phi_+ = x\bar{U} + (1-y)xD; \;\; \Phi_- = xU + (1-y)x\bar{D}$$

with $U = u + c$ and $D = d + s$. From these expressions and from fig. 1.21 one can remark that: with positron (electron) beams one can determine d^v (u^v) at high x and small-y and $\bar{u}+\bar{c}$ ($\bar{d}+\bar{s}$) at small y. Let us mention that d_v and the sea quarks are basically determined in the global pQCD fits by μ-deuterium and $\nu(\bar{\nu})$-iron fixed target data, which require some nuclear corrections. Therefore, with the HERA $e^\pm p$ CC events one may have, with more statistics, a unique means to determine these quark densities.

In fig 1.23, $d\sigma/dx$ is shown together with the error band determined by the ZEUS pQCD fit (without the CC and NC data described in this appendix), and with the results of a recent analysis where an ansatz $d/u \neq 0$ as $x \to 1$ [36] was introduced. Although the statistics is still low, one can notice from fig. 1.23 that this latter hypothesis is not required by the HERA data.

In fig. 1.24, the measurement of $d\sigma^{e^-p}/dx$ is shown. The error band of the pQCD is much smaller than in fig. 1.23, therefore one can expect a better determination of electroweak parameters. The size of the error bands reflect that u^v is much better constrained than d^v in the pQCD fits.

Extraction of F_L

The longitudinal structure function is very hard to determine. It requires to combine data in a given x-Q^2 bin from different beam energies. However, from eq. (1.22), one observes that at high y the cross section receives a contribution both from F_2 and F_L.

Therefore, taking F_2 from the result of a pQCD fit (see previous section) applied to the low y ($y < 0.35$) data one can determine F_L at high y by subtracting F_2, extrapolated to high y. To reach lower Q^2, where pQCD is not reliable, another method is used. Writing

$$\frac{\partial \sigma_r}{\partial \log y} = \frac{\partial F_2}{\partial \log y} - 2y^2 \frac{2-y}{Y_+^2} F_L - \frac{y^2}{Y_+} \frac{\partial F_L}{\partial \log y},$$

neglecting $\partial F_L / \partial \log y$, and assuming that $\partial F_2 / \partial \log y$ is a linear function of $\log y$, one can determine F_L (these assumptions being justified by experimental onservations). $\frac{\partial \sigma_r}{\partial \log y}$ is shown in fig. 1.25 and F_L in fig. 1.26. This determination is consistent with the NLO calculation of pQCD. It should be pointed out that because of the high sensitivity of F_L to the gluon density xg, a precise measurement of F_L would provide a complementary determination of xg.

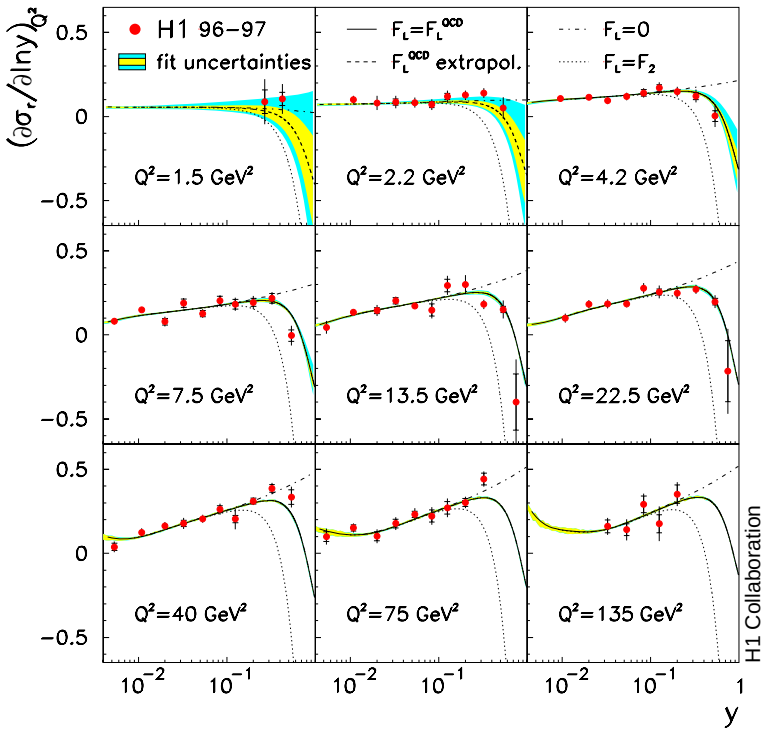

Figure 1.25: *H1 determination of* $\frac{\partial \sigma_r}{\partial \log y}$ *(see text). The sensitivity of this quantity to* F_L *is demonstrated by comparing QCD calculation in the two extreme cases* $F_L = 0$ *and* $F_L = F_2$.

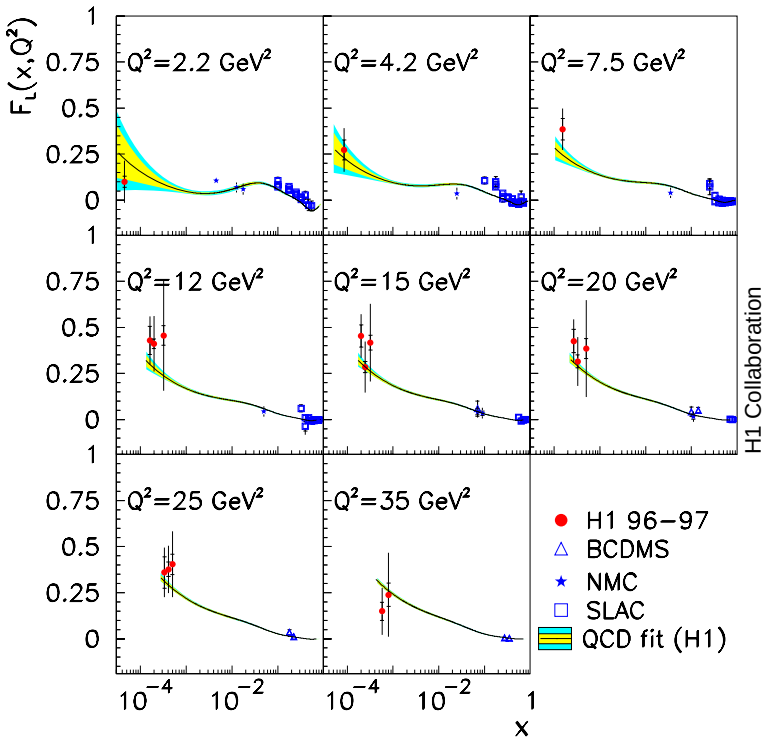

Figure 1.26: *H1 determination of F_L compared to fixed target measurements and to QCD calculations.*

Bibliography

[1] C.Y. Prescott et al., Phys. Lett. B 77 (1978) 347.

[2] A. Argento et al., Phys. Lett. B 140 (1984) 142.

[3] Proceedings of the 1995/1996 Future Physics at HERA Workshop, ed. G. Ingelman, A. De Roeck and R. Klanner (DESY, Hamburg, 1996).

[4] M. Klein, in 9th International Workshop on Deep Inelastic Scattering (Bologna 2001).

[5] P. Kroll, M. Schurmann and P.A.M. Guichon, Nucl. Phys. A 598 (1996) 435.; A. Freund and M. Strimann, Phys. Rev. D 60 (1999) 071501.

[6] E. Barrelet et al., *Proposal to upgrade the leongitudinal polarimeter*, DESY-PRC-00-06, 2000.

[7] Z. Zhang, *Nouveaux aspects de la structure du proton avec le collisionneur HERA*, Habilitation Thesis, Orsay, France, 2000. LAL report LAL 00-57/2000.

[8] Cornet and Rückl, P. 771 Vol. 2, in [16].

[9] C. Pascaud and F. Zomer, LAL 95-05/1995.

[10] H1 Coll., C. Adloff et al., Eur. Phys. J., C13 (2000) 609.

[11] G. D'Agostini, CERN Yellow Report 99-03

[12] D.P. Barber et al., Nucl. Instr. Meth., A338 (1994)166.

[13] G. D'Agostini and M. Raso,`hep-ex/0002056`.

[14] D0 Coll., Phys. Rev. Lett.76 (1996) 3271.

[15] M.A. Doncheski and J.L Hewett, Z. Phys. C (1992) 209.

[16] Proceedings of the 1987 HERA Physics Workshop, ed. R.D. Peccei (DESY, Hamburg, 1988).

[17] Proceedings of the 1991 HERA Physics Workshop, ed. W. Buchmuller and G. Ingelman (DESY, Hamburg, 1992).

[18] M. Klein and T. Reinmann, Z. Phys. C 24 (1984) 151.

[19] R. J. Cashmore et al. p. 163-207 in [3].

[20] Results from LEP, available on `http://lepewwg.web.cern.ch/LEPEWWG/` (2002).

[21] H1 Coll., Nucl. Instr. Meth. A336 (1997) 348; The ZEUS detector, status report DESY-1993.

[22] BCDMS Coll., Phys. Lett. B223 (1989) 485; Phys. Lett. B237 (1989) 592; NMC Coll., Nucl. Phys. B483 (1997) 3.

[23] Z. Zhang, private communication.

[24] S. Bentvelsen et al., p. 23 in [17], K.C. Hoeger, p. 43 *ibid.*

[25] U. Bassler and G. Bernardi, Nucl. Instrum. Meth. A 361 (1995) 197; Nucl. Instrum. Meth. A 361 (1999) 583.

[26] H1 Coll., Eur. Phys. J. C13 (2001)33; ZEUS Coll., DESY-01-064 (2001), accepted by Eur. Phys. J. C.

[27] ZEUS Coll.,Eur. Phys. J. C11 (1999) 427; ZEUS Coll., Eur. Phys. J. C12 (2000) 411; see ref. [10]; H1 Coll., Eur. Phys. J. C19 (2001) 269.

[28] A. Blondel and F. Jacquet, *Proceeding of the study of an ep facility in Europe*, ed. U. Amaldi, DESY 79/48 (1979) 391.

[29] W. Furmanski and R. Petronzio, Z. Phys. C1 (1982) 293.

[30] See for a recent review: A.M. Cooper-Sarkar, R.C. Devenish and A. De Roeck, Int. J. Mod. Phys. A13 (1998) 3385.

[31] M. Gluck, E. Reya and M. Stratmann, Nucl. Phys. B422 (1994) 37.

[32] E. Laenen et al., Nucl. Phys. B392 (1993) 162 and 229; Phys. Lett. B291 (1992) 325.

[33] C. Pascaud and F. Zomer, DESY 96-266; J. Blümlein et al., in ref. [3].

[34] Particle Data Group, Eur. Phys. J. C15 (2000) 1.

[35] CTEQ4 Coll., Phys. Rev. D55 (1997) 1280; MRS Coll., Phys. Rev. D51 (1995) 4756.

[36] U.K. Yang and A. Bodek, Phys. Rev. Lett. 82 (1999) 2467.

Chapter 2

Electron beam Polarisation and Polarimetry

In this chapter, the electron beam polarisation rise in storage rings and the polarisation measurement are described. The former topic has been covered by many review articles and text-books in the past ([1, 2, 3, 4]). Another very useful document is a thesis on the HERA polarisation after the HERA-II upgrade [5] where qualitative and quantitative aspects are much developed. Since I didn't contribute in this field, I will only give a very brief account on this very rich topic.

In this chapter I will therefore concentrate on the electron beam polarisation measurement. Moreover, with regard to the HERA machine I will only describe polarimetry experiments in high energy electron storage rings.

2.1 Electron beam polarisation

The definition of the polarisation of an electron bunch is not straightforward. We shall therefore start by the very basic definition in order to define precisely what is the "polarisation" that we do measure in the HERA ring.

As we shall later see in this chapter, the polarisation of an electron bunch can be measured by Compton scattering, i.e. via laser beam - electron beam interactions. The polarisation measurement thus gives access to an average value. In Quantum Mechanics, this measurement corresponds to a statistical system with missing information (i.e. the spin state of all electrons at a given time). To describe such a system the density matrix formalism [6] is the most useful one [3].

Let us first give the definition of the "spin vector" $\overrightarrow{S_k}$ attached to a single particle circulating on a given trajectory at a given energy. Giving the quantum state $|\Psi_k>$ describing this system, one gets, in the centre of mass of the electron:

$$\overrightarrow{S_k} = <\Psi_k| \overrightarrow{\mathcal{S}} |\Psi_k>$$

where $\overrightarrow{\mathcal{S}} = (\mathcal{S}_X, \mathcal{S}_Y, \mathcal{S}_Z)$ is the spin vectorial operator (in the basis of the eigen-vectors of the third Pauli matrix, $\overrightarrow{\mathcal{S}}$ is represented by the three Pauli matrices $\overrightarrow{\sigma}$). The direct axis system is chosen such Z coincides with the direction of motion and Y is the vertical axis, see fig. 2.1).

We can now define the spin polarisation of a mono-energetic electron bunch [3]:

$$\overrightarrow{P} = \frac{2}{\hbar}\sum_k p_k < \Psi_k | \overrightarrow{\mathcal{S}} | \Psi_k > \equiv \left\langle \frac{2}{\hbar}\overrightarrow{S} \right\rangle,$$

where p_k is the probability of a single particle state $|\Psi_k>$ to occur. Hence, the bracket stands here for the average of all possible one particle spin quantum states (i.e. ensemble average).

2.1.1 Polarisation build up in storage rings

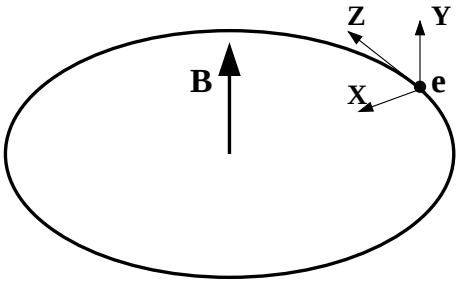

Figure 2.1: *Axis system and perfect circular orbit around a magnetic field.*

Unlike linear accelerators where polarised electrons are created and kept polarised up to the interaction point [7], in storage rings the polarisation is built up thanks to synchrotron radiation in the bending magnets. This is the so called Sokolov-Ternov effect [8].

Since this effect is the key point of polarisation at HERA, let us give here more details. An electron beam deflected around a magnetic field aligned along the Y axis radiates photons (see fig. 2.1). During this process, a flip of the projection of the electron spin along Y can occur. The spin-flip probabilities per unit of time $w_{\uparrow\downarrow}$ (spin up $\rightarrow$ spin down) and $w_{\downarrow\uparrow}$ (spin down $\rightarrow$ spin up) corresponding to an electron spin aligned and anti-aligned respectively with the magnetic field have been calculated in ref. [8]. Using the notations of ref. [2], one has:

$$w_{\uparrow\downarrow} = \frac{5\sqrt{3}}{16}\left(1 + \frac{8}{5\sqrt{3}}\right) c\lambda_c r_0 \frac{\gamma^5}{\rho^3}, \quad w_{\downarrow\uparrow} = \frac{5\sqrt{3}}{16}\left(1 - \frac{8}{5\sqrt{3}}\right) c\lambda_c r_0 \frac{\gamma^5}{\rho^3}$$

where γ is the electron Lorentz factor, ρ the bending radius of the magnetic field,

$$\lambda_c = \hbar/(m_e c) = 3.8616 \cdot 10^{-13}\,\mathrm{m}$$

is the reduced electron Compton wavelength and

$$r_0 = e^2/(4\pi\epsilon_0 m_e c^2) = 2.8179 \cdot 10^{-15}\,\mathrm{m}$$

is the classical electron radius.

The fact that $w_{\downarrow\uparrow} \neq w_{\uparrow\downarrow}$ implies that starting from an unpolarised beam, synchrotron radiation induces a transverse polarisation. Asymptotically, this polarisation is given by

$$P_{ST} = \frac{w_{\uparrow\downarrow} - w_{\downarrow\uparrow}}{w_{\uparrow\downarrow} + w_{\downarrow\uparrow}} = \frac{8}{5\sqrt{3}} \sim 92.4\%$$

and the time evolution reads

$$P_Y(t) = -P_{ST}\left(1 - e^{-t/\tau_{ST}}\right)$$

with

$$\tau_{ST} = \frac{1}{w_{\uparrow\downarrow} + w_{\downarrow\uparrow}} = \frac{8\rho^3}{5\sqrt{3}c\lambda_c r_0 \gamma^5},$$

where P_{ST} is often called equilibrium or asymptotic polarisation and the subscript ST refers to the Sokolov-Ternov effect. Note that the asymptotic polarisation is a constant, below 1 and anti-parallel with respect to the magnetic field (it is parallel for positron beams). At HERA for an electron beam energy $E_e \approx 27$ GeV one gets $\tau_{ST} \approx 40$ min. This very long time, reflecting the small spin-flip probability, must be compared to the time interval between two photon emissions $\sim 10^{-8}$ s.

These results are valid under the following assumptions: the magnetic field is homogeneous, after radiation the electron stays on its perfect circular orbit and synchrotron radiation is a random process. Although the latter assumption is justified, this is obviously not the case for the formers. We must now then look at the spin-orbit coupling effects.

2.1.2 Depolarisation effects

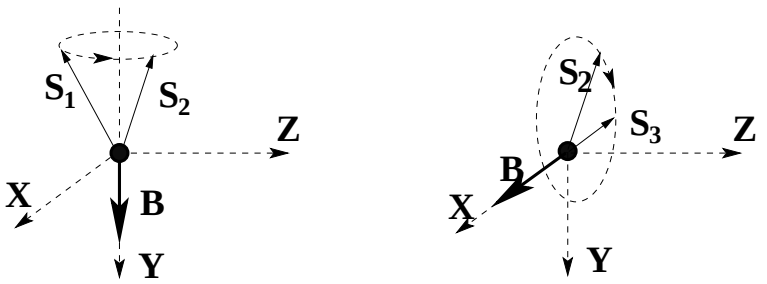

Figure 2.2: *Naive illustration of depolarisation effects. Left plot: precession of the spin vector around the magnetic field normal to the plane of motion. Right plot: precession around a magnetic field perpendicular to the beam direction and inside the plane of motion.*

The evolution of $\overrightarrow{S}$ inside homogeneous and inhomogeneous electromagnetic fields is described by a first order semi-classical differential equation, named the T-BMT equation (see [4] for an overview). One of the key features of the spin motion in magnetic fields is the spin-precession. It is illustrated in fig. 2.2: when the magnetic field experienced by

the electron is perpendicular to the plane of motion, the spin direction changes but its projection along Y remains constant while the precession around a magnetic field inside the plane of motion reduces the spin projection along Y.

Since the T-BMT equation is a linear differential equation containing a cross product between electromagnetic field vectors and the spin vector, electric and magnetic fields change the direction of a spin vector but not its absolute value, i.e. spins precess. We have already seen that synchrotron radiation in dipoles causes a build up of polarisation by the Sokolov–Ternov effect. However, it can also lead to depolarisation. This happens as follows: after a photon of synchrotron radiation is emitted, a particle jumps from its original orbit to another. A spin then "feels" magnetic fields in the quadrupoles which it would not have felt in the absence of photon emission and, by the T–BMT equation, its precession is modified. Then, since photon emission is stochastic, the spins in the bunches "diffuse". In the presence of depolarisation the asymptotic polarisation is reduced with respect to P_{ST}.

To get an idea of these dynamics one must look at the time scales. The orbit period is $\approx 10^{-5}$s at HERA and the betatron and synchrotron oscillations periods are $\sim 10^{-6}$ s and $\sim 10^{-4}$ s respectively. Once excited, these oscillations are damped within $\sim 10^{-2}$ s typically. If we now compare these time scales to the time scale for synchrotron emissions $\sim 10^{-8}$ s, we see that an electron bunch corresponds to a superposition of a large number of orbits.

The major effect of transverse perturbating magnetic fields is the resonant depolarisation. In a perfectly flat machine, the number of 2π spin precessions around the vertical direction per turn is given by $\nu_0 = a\gamma$ with $a = (g-2)/2$ the electron gyro-magnetic anomaly. This is the so called "naive spin tune"[3] ($\nu_0 = 62.5$ at HERA). In a real machine, the spin tune is not given by this simple formula (although in HERA the real "spin tune" is still approximately proportional to the beam energy[3]) but the important point is that, when the spin tune and the frequency of the perturbating magnetic field are the same, then the spin is coherently kicked at each turn. To optimise the beam polarisation, one obviously has to choose a beam energy far from depolarisation resonances.

Another source of depolarisation is the effect of the proton bunch charge on the electron bunch polarisation. This phenomenon, named beam-beam effect, can be viewed as a quadrupole magnet effect on the electron beam. There is no clear statement about the importance of this depolarisation source for HERA-II, though some experience was gained after the 2000 proton focusing upgrade. With the HERA-II upgrade, it is then expected that beam-beam effect will further reduce the polarisation.

An important point for polarimetry must be noted here. Comparing the polarisation build up characteristic time ($\approx$ 40 mn) to the other process time scales, one sees that polarisation is varying very slowly and is therefore the same, in absolute value but not in direction, all over the ring.

2.1.3 Spin rotators and longitudinal polarisation at HERA

From what has been described in the previous sections, one sees that the electron beam is vertically polarised at HERA. To convert this polarisation into a longitudinal polarisation, spin rotators must be supplied.

In principle a spin rotator is a simple device. Making use of the spin precession, a set of transverse magnetic fields can transform a transverse to a longitudinal polarisation.

These spin rotators are located around the electron-proton interaction points (in the arcs of HERA) and longitudinal polarisation must be transformed back to transverse polarisation before the arcs in order not to depolarise the beam. That's why rotators always appear by pairs.

In practice one has to face many problems for the rotator design: the space constraints (e.g. solenoids are space consuming and are weak spin rotators unlike bending magnets), the beam orbit stability, sensitivity of the field design to the beam energy, facility to switch from e^- to e^+ and the optimisation of the beam polarisation.

The mini-rotator solution [9] has been chosen for HERA. It consists in three series of horizontal bending magnets interleaved with vertical bending magnets as shown in fig 2.3.

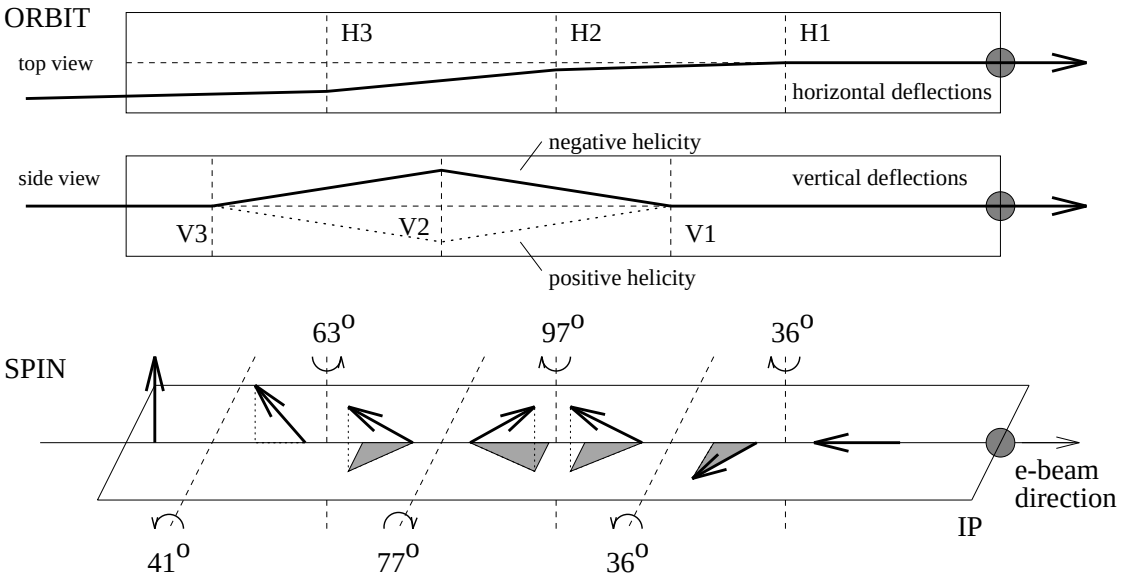

Figure 2.3: *Mini rotator at HERA. A schematic view of the orbit motion is shown in the two top plots and changes of the spin direction in the bottom plot. Symbols V and H refer to vertical and horizontal bending magnets respectively. The total length of the spin rotator is 56 m.*

2.1.4 Optimisation of the polarisation at HERA

When nothing is done to counteract depolarisation effects, the equilibrium transverse polarisation, written here P_∞ with $P_\infty < P_{ST}$, is very low [10]. A description of the complex techniques used to optimise the polarisation in a ring like HERA is outside the scope of this document.

With regard to the performances of the polarimeter, it is however necessary to mention one of these techniques, the "closed orbit spin matching" [11]: eight ensembles of magnets (named the harmonic bumps) are located in the HREA straight sections in order to minimise the effects of the distortion of the closed orbits on the polarisation. [11]

To optimise the harmonic bumps, an empirical procedure is adopted: an operator varies the kick amplitudes of the beam inside the magnets constituting the harmonic

bumps and then observes the expected asymptotic polarisation. If the polarisation increases then the variation is continued, if not the process is stopped (see also fig. 2.9). Therefore a very fast and accurate polarisation measurement would help to optimise the polarisation at HERA.

2.1.5 Polarisation operations at HERA

Before the year 2000, HERA operated with two spin rotators around the HERMES experiment. After the HERA upgrade, spin rotators have been installed around H1 and ZEUS experiments (see fig. 2.4). Thus the HERA ring now contains three pairs of spin rotators.

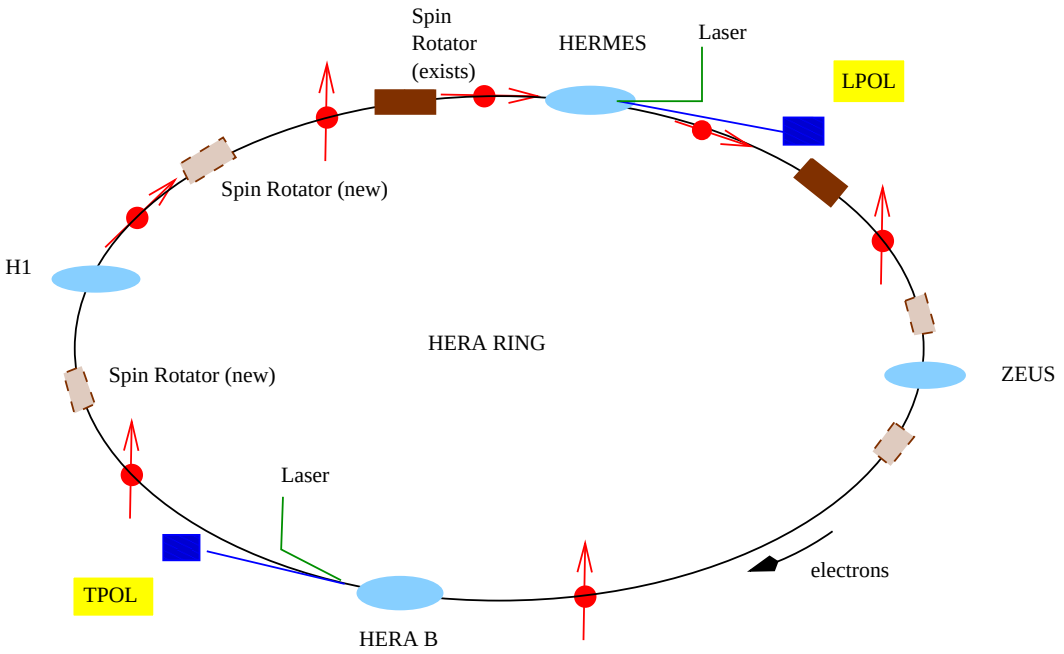

Figure 2.4: *Schematic view of the HERA ring. Before 2000, two spin rotators where installed around HERMES. Since the 2000 shutdown, pairs of spin rotators have been installed around the H1 and ZEUS experiments. Positions of the TPOL and LPOL Compton polarimeters are also indicated.*

Two polarisation measurements are currently performed at HERA (see section 2.2): the longitudinal polarisation (LPOL) measurement is performed after the HERMES interaction point (IP) and the transverse polarisation (TPOL) is measured in the west hall close to the HERAB experiment[1]. Both measurements agree within their measurement uncertainties and their accuracies are indicated in tab. 2.1. The variation of polarisation with time is shown in fig. 2.5 for three different machine fills. These measurements provide an illustration of the behaviour of the polarisation at HERA: rise time of the order of 40 min, non-reproducibility of polarisation variations from a fill to another.

[1]The reason why no polarimeter is located after H1 or ZEUS is that not enough space is available around the experiments and that it is not needed.

	Laser beam power	$\Delta P_{stat.}$	$\Delta P_{syst.}$
LPOL	33 MW (pulsed)	1%/min (all bunches) 1%/bunch over 30 min	$\approx 2\%$
TPOL	10 W (continuous)	1%/min (all bunches)	$\approx 2\%$

Table 2.1: *Main characteristics of the existing HERA polarimeters: laser beam power, statistical and systematic uncertainties.*

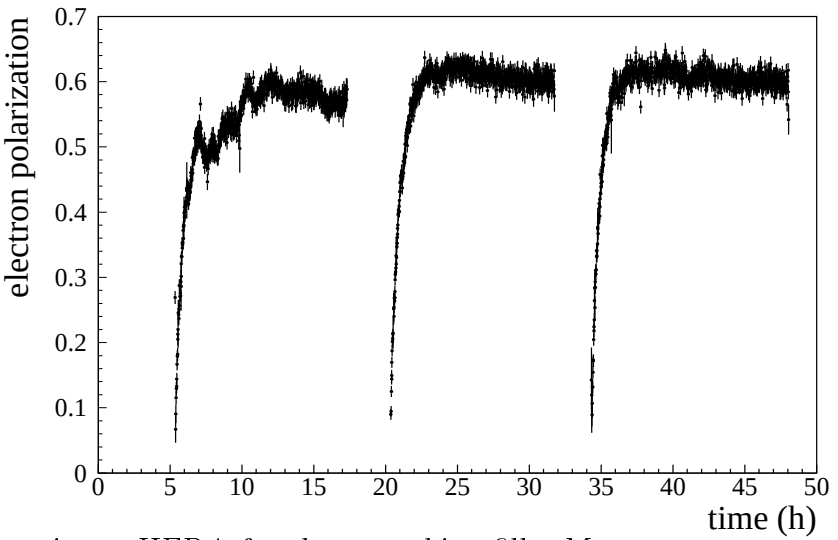

Figure 2.5: *Polarisation rise at HERA for three machine fills. Measurements come from the HERA-LPOL setup [12].*

There are approximately two hundred electron bunches circulating in the HERA ring (the beam current is around 50 mA) and some of them do not collide with protons. Hence, they do not suffer from beam-beam effects and their polarisation is often different from that of the colliding bunches. Typical differences between the polarisation of colliding and non-colliding bunches are shown in fig. 2.6. The two plots of this figure correspond to different machine fills and one can see that relative difference of polarisation between colliding and non-colliding beams varies from fill to fill and can reach $10 - 50\%$.

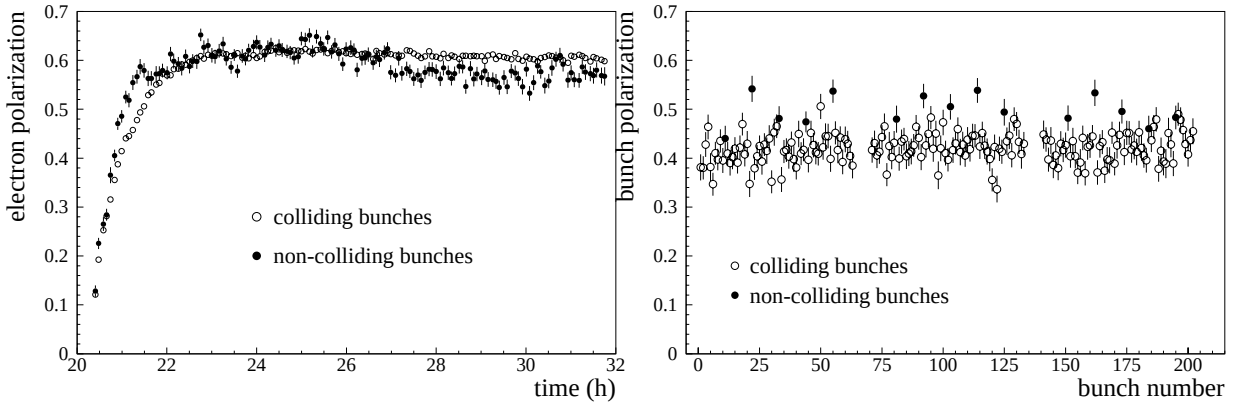

Figure 2.6: *Left plot: polarisation as a function of time measured by the HERA-LPOL [12]. Right plot: polarisation as a function of the bunch number measured by the HERA-LPOL [12]. In both plots, polarisation of the colliding and non-colliding bunches are shown separately.*

To further illustrate the unpredictable aspect of the polarisation behaviour, an online measurement performed after the TPOL data acquisition system upgrade [13] is shown in fig. 2.7. The structure of the three trains of bunches is clearly visible and the bunch to bunch polarisation variation inside one train is attributed to the interaction between the electron beam and its associated wake-field and the RF cavities (which vanishes between two trains of bunches). Variations of the equilibrium polarisation also appears naturally because of the slow drift of the beam orbit[2] inside the magnetic fields during a run duration (typically 10 h). Fig. 2.8 shows that such variations can be as large as $\sim 10\%$.

Finally, an illustration of the tuning of the harmonic bumps is shown in fig. 2.9. This tuning was performed after a change of the beam optics. The optimisation steps are clearly visible ("bumps" in the polarisation rise-up). As mentioned above, a fast and precise polarimeter would certainly help to avoid the decrease of the equilibrium polarisation.

2.1.6 Polarisation and physics analysis

Two important topics are described here: the value of the longitudinal polarisation at the H1 IP and the systematic uncertainty on physics measurements due to the uncertainty in the knowledge of the polarisation. The results reported below were produced for the LPOL upgrade proposal [14].

As mentioned in the Introduction, the increase of luminosity at HERA is achieved by further squeezing of the electron and proton beams at the IP. This stronger focusing is

[2]For example, this can happen when the machine group optimises the orbit to increase the luminosity for one of the HERA experiments.

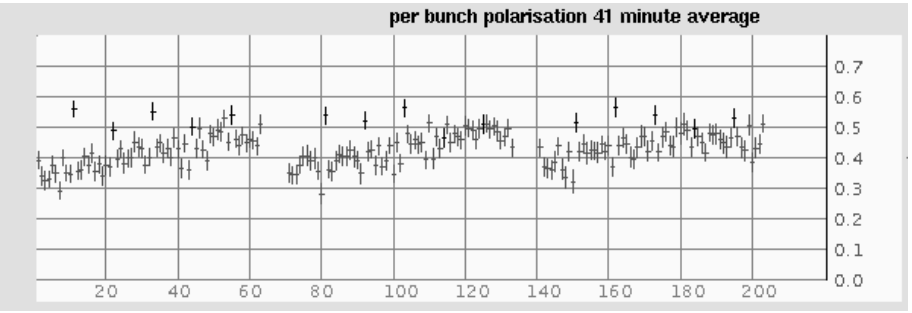

Figure 2.7: *On-line polarisation measurement as a function of the bunch number. Data come from the upgrade TPOL setup. Isolated points above* 0.5 *correspond to the non-colliding bunches.*

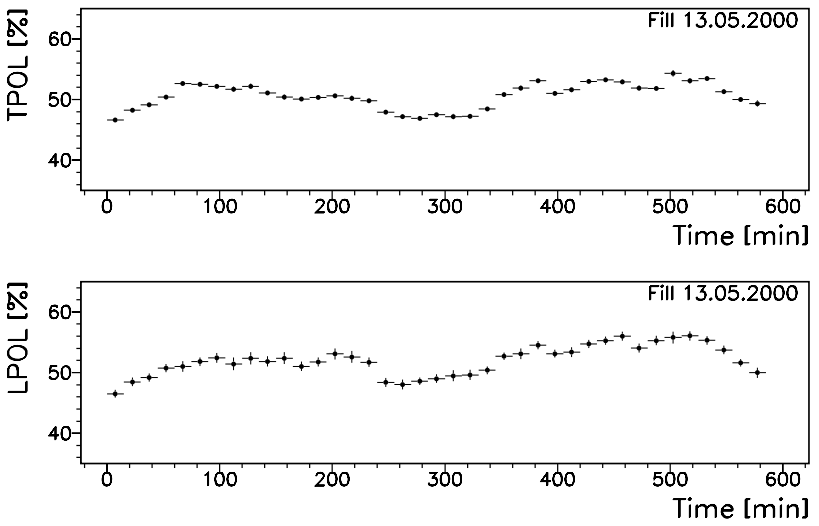

Figure 2.8: *Off-line TPOL and LPOL polarisation measurement as a function of time. Polarisation is averaged over all bunches.*

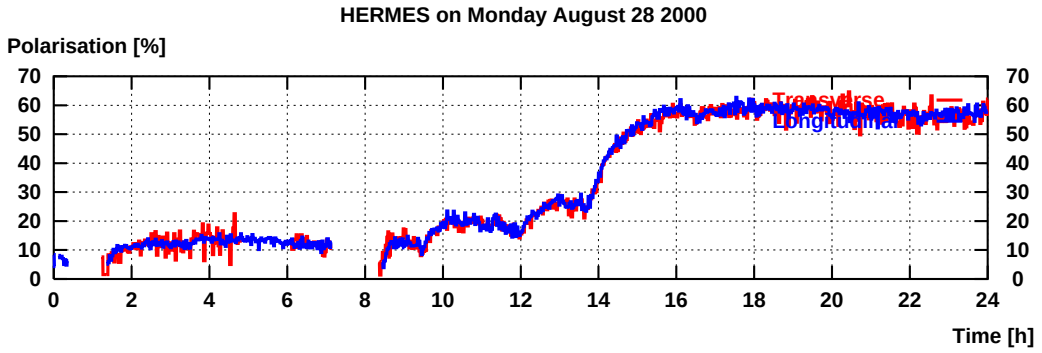

Figure 2.9: *Optimisation of the harmonic bumps after a machine modification. The tuning procedure of the bump is clearly visible.*

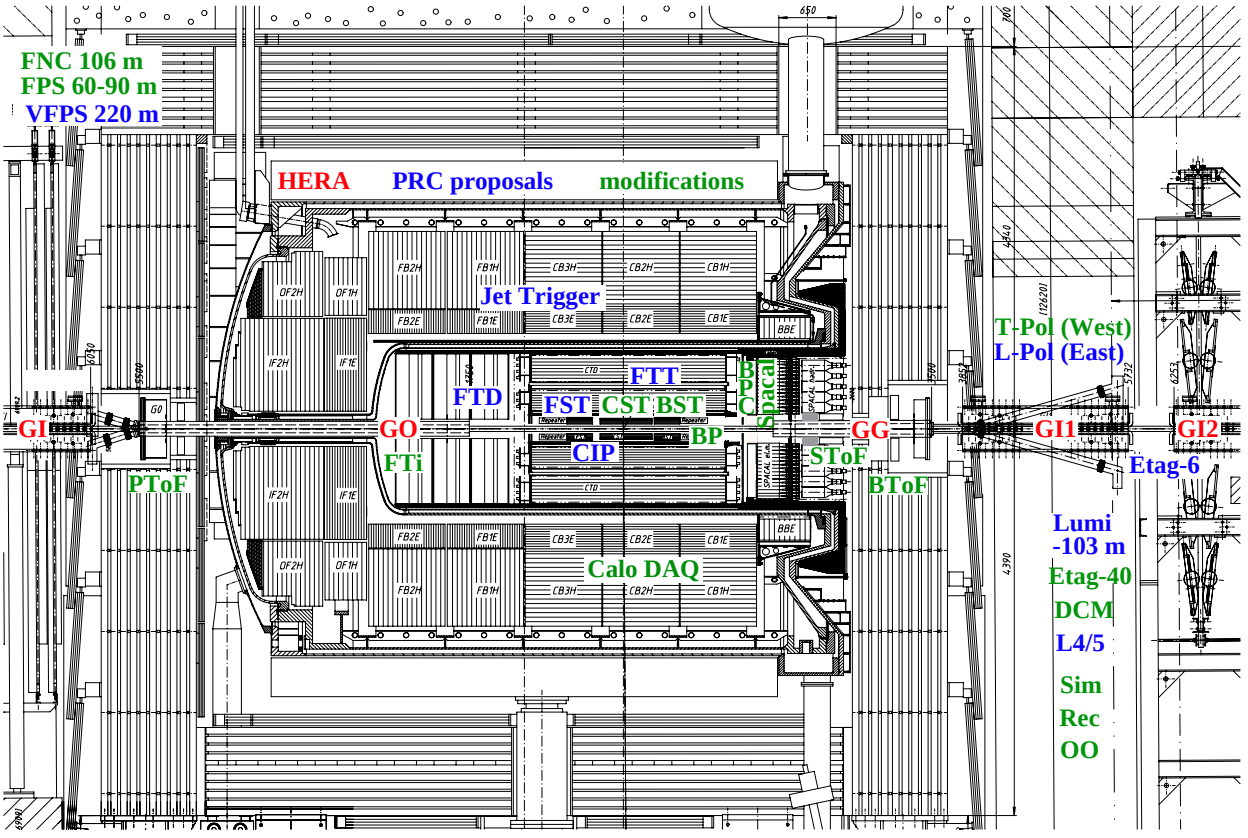

Figure 2.10: *Side view of the H1 detector. The various upgrades performed for HERA-II are indicated. The two new elements increasing the luminosity are the combined function super-conducting magnets GG and GO.*

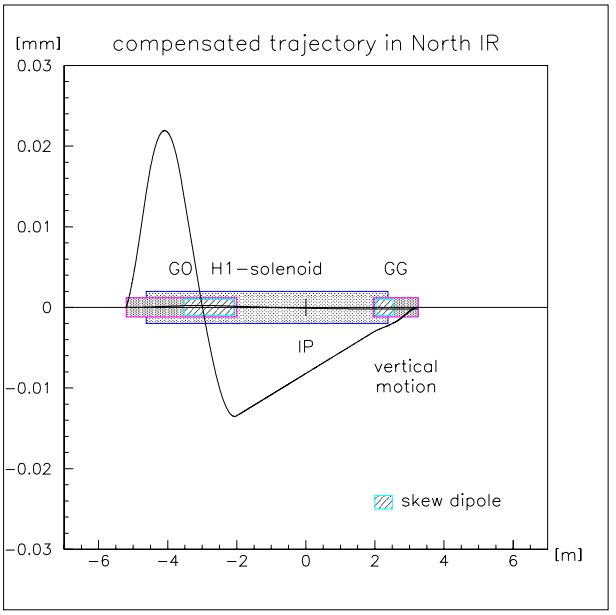

Figure 2.11: *Schematic view of the corrected orbit in the horizontal plane inside the H1 solenoid. GO and GG are the combined function long supra-conducting magnets. From [5]*

obtained by installing, among other optical elements, two long combined function superconducting magnets (for vertical beam focusing and electron-proton beam separation) inside the ZEUS and H1 experiments [15]. While these $\sim$ 2 m long magnets fit well outside the ZEUS solenoid the situation is different in H1 where one of the magnets (on the upstream electron beam side) is located inside the solenoid (see fig. 2.10). Then the direction of polarisation changes between the H1 entrance and the H1 IP (see fig 2.11) so that the rotators must be slightly retuned to ensure that the polarisation axis remains vertical in the arcs and extra depolarisation is avoided [5]. The new layout also precludes the use of compensating solenoids. Thus the resulting effects on the optics have been neutralised with skew quadrupoles. This, together with the new, more complex fields at the ends of the H1 solenoid causes extra depolarisation.

The second topic is related to the question of what polarisation inputs are needed for physics analysis. When N_{run} machine fills are combined, what is indeed needed is not the absolute beam polarisation but the luminosity weighted polarisation:

$$\overline{P} = \frac{\sum_{r=1}^{N_{run}} \int_{t_{min,r}}^{t_{max,r}} \sum_{b=1}^{N_{bunch}} P(r,b;t)\mathcal{L}(r,b;t)dt}{\sum_{r=1}^{N_{run}} \int_{t_{min,r}}^{t_{max,r}} \sum_{b=1}^{N_{bunch}} \mathcal{L}(r,b;t)dt} \tag{2.1}$$

where $(t_{max,r} - t_{min,r})$ is the duration of the r^{th} run, N_{bunch} is the number of colliding bunches and $\mathcal{L}(r,b;t)$ and $P(r,b;t)$ are the instantaneous luminosity and polarisation of the b^{th} bunch of the r^{th} machine fill respectively.

From eq. (2.1) it appears that two systematic sources can propagate to the physics measurements: the space and time correlations between luminosity and polarisation. The time correlation effect is important when data taken at the beginning of the machine

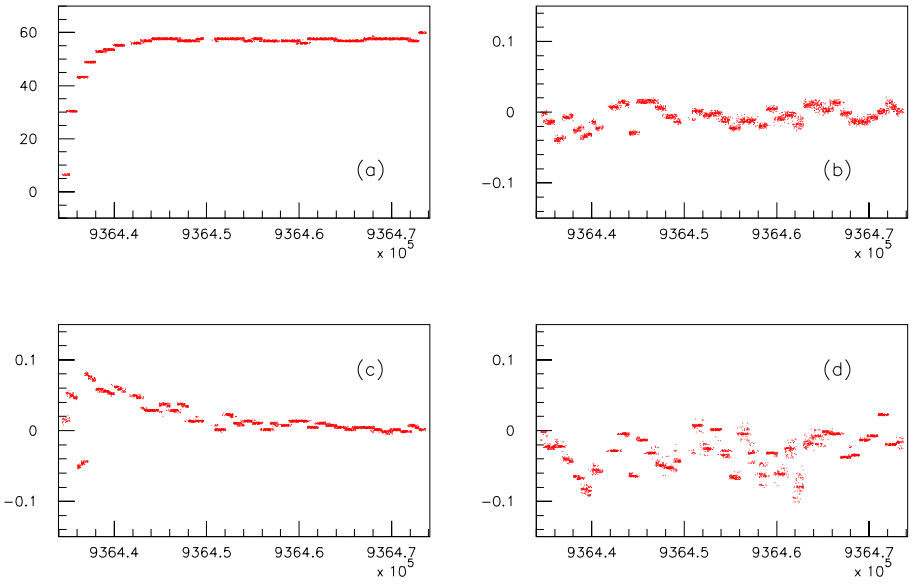

Figure 2.12: *Polarisation (a), $C^t(P,L)$ (b), $C^t(P,I_e)$ (c) and $C^t(P,I_p)$ (d) versus the time for one typical fill. From ref. [14].*

fills are kept in the analysis. During this period the electron beam current is maximum but luminosity and polarisation are 100% anti-correlated: luminosity decreases with time and polarisation rises up. However, as indicated in section 2.1.5, one cannot correct accurately using a model for the polarisation rise-up. Therefore, to precisely control the correlations between polarisation and luminosity during this period, a fast polarimeter must be operated. A precise estimate of the required time for polarisation measurement depends strongly on the shape of the non-reproducible polarisation rise-up and of the "t_0", i.e. the H1 and ZEUS Data Acquisition Systems start up.

The second effect is related to a possible bunch to bunch correlations between polarisation and luminosity. That is, for a given run r and at a given time t

$$\frac{1}{N_{bunch}} \sum_{b=1}^{N_{bunch}} P(r,b;t)\mathcal{L}(r,b;t)$$

is not *a priori* the same as

$$\frac{1}{N_{bunch}^2} \sum_{b=1}^{N_{bunch}} P(r,b;t) \sum_{b=1}^{N_{bunch}} \mathcal{L}(r,b;t)\,.$$

To quantify such a correlation, let us introduce the time evolution of the bunch to bunch correlation coefficient $C^t(P,X)$ between the polarisation and a variable X. It is defined by:

$$C^t(P,X) = \frac{\Sigma_{b=1}^{N_{bunch}}(P_b - < P >)(X_i - < X >)}{\sqrt{\Sigma_{b=1}^{N_{bunch}}(P_b - < P >)^2 \Sigma_{b=1}^{N_{bunch}}(X_i - < X >)^2}}$$

with $< P >= 1/N_{bunch} \times \Sigma_{b=1}^{N_{bunch}} P_b$ and $< X >= 1/N_{bunch} \times \Sigma_{b=1}^{N_{bunch}} X_b$. Here, X can be e.g. the luminosity $\mathcal{L}$, the lepton beam intensity I_e or the proton beam intensity I_P.

In fig. 2.12(a) the polarisation as a function of time is shown for a typical HERA fill. For this fill the correlations to the luminosity, the electron and the proton current are shown in fig. 2.12(b), 2.12(c) and 2.12(d) respectively. The luminosity and the current intensity are measured every 10 s and the polarisation corresponds to an average over 10 min. Although correlations seems to exist in the early part of the fill no conclusive statement can be drawn with the current level of accuracy. These studies show anyhow that a fast and precise polarimeter would be useful to measure the luminosity-polarisation correlations, if they exist.

2.2 Polarisation measurement: Compton scattering

Several methods exist for measuring an electron beam polarisation at high energy (see refs. [10, 16] for examples). Among them, the most accurate one at high energy is Compton polarimetry. We therefore concentrate on this method in the following sections. Since interactions between polarised electrons and polarised light are involved, we start with a general and brief introduction to laser light polarisation.

2.2.1 Jones and Stokes-Mueller Formalism in optics

For a detailed introduction to optics and light polarisation we refer to refs. [17, 18]. We summarise here the Jones and Stokes-Mueller formalism.

The electric field vector $\mathbf{E}$ of an electromagnetic wave is obtained by solving the Maxwell equations with the appropriate boundary conditions. For monochromatic and not too divergent waves, the plane wave approximation holds: in isotropic media, $\mathbf{E}$ is located in a plane perpendicular to the wave vector $\mathbf{k}$, with $|\mathbf{k}| = k = 2\pi/\lambda$ and λ the wavelength.

Introducing a direct system of coordinates $\{x, y, z\}$ and a corresponding unit vector basis $\{\hat{\mathbf{x}}\ ,\hat{\mathbf{y}}\ ,\hat{\mathbf{z}}\ \}$ such that $\mathbf{k} = k\hat{\mathbf{z}}$, one can write $\mathbf{E} = E_x\hat{\mathbf{x}} + E_y\hat{\mathbf{y}}$ and define the polarisation by the time evolution of (E_x, E_y). The beam intensity is defined by the Poynting vector. That is, for plane waves in homogeneous and non-absorbing media[19]:

$$I = I_x + I_y = \frac{1}{2} n\epsilon_0 c(|E_x|^2 + |E_y|^2)$$

with n the optical index of the medium, ϵ_0 the vacuum dielectric constant and c the light velocity. This is the energy per unit area per unit time. Since we shall only consider beam intensities in the air, the constant factor in the intensity expression will be skipped so that we shall write $I = I_x + I_y = |E_x|^2 + |E_y|^2$.

Working in the complex space – i.e. E_x, $E_y \in \mathbb{C}$ [3] – and concentrating on the polarisation, the effect of a perfect [4] optical component can be described by a 2×2 matrix $\mathcal{M}_J$ called Jones matrix [21]

$$\begin{pmatrix} E'_x \\ E'_y \end{pmatrix} = \mathcal{M}_J \begin{pmatrix} E_x \\ E_y \end{pmatrix}$$

[3] The electric field being given by the real part of the complex field. The use of the complex field to solve the Maxwell equation easier with complex fields (see ref. [20] for example).

[4] By perfect we mean that transmission of plane waves through the optical element does not generate interferences. I.e., multiple internal reflections, if existing, are neglected.

where (E_x, E_y) and (E'_x, E'_y) are the electric field components before and after the optical element respectively. Jones matrices of the commonly used elements (retardation plate, linear and circular polarisers, rotators ...) can be found in textbooks [18, 22, 23].

To describe light polarisation, an alternative approach is the Stokes vector and the Mueller matrix formalism. The Stokes vector is defined by

$$S = \begin{pmatrix} S_0 = |E_x|^2 + |E_y|^2 \\ S_1 = |E_x|^2 - |E_y|^2 \\ S_2 = E_x E_y^* + E_x^* E_y \\ S_3 = i(E_x E_y^* - E_x^* E_y) \end{pmatrix} = \begin{pmatrix} I \\ I_x - I_y \\ I_{+\pi/4} - I_{-\pi/4} \\ I_L - I_R \end{pmatrix} \tag{2.2}$$

where the symbol * refers to the complex conjugate. I is the beam intensity; I_x, I_y, $I_{+\pi/4}$ and $I_{-\pi/4}$ are the intensities measured after a linear polariser oriented along $\hat{\mathbf{x}}$, $\hat{\mathbf{y}}$, $\hat{\mathbf{x}} + \hat{\mathbf{y}}$ and $\hat{\mathbf{x}} - \hat{\mathbf{y}}$ respectively; I_L and I_R are the intensities after circular left and right polarisers respectively. For polarised light, the following relation holds:

$$S_0 = \sqrt{S_1^2 + S_2^2 + S_3^2}.$$

In the forthcoming chapters, we shall often designate S_3 as the degree or level of circular polarisation.

The relation between the Stokes vectors before and after an optical element is also linear and is then described by a 4×4 matrix (called Mueller matrix).

Both formalisms are in principle equivalent and are related by well known mathematical transformations. Essential differences are:

- Partially polarised light is directly described by the Mueller formalism but not in a straightforward way by the Jones formalism.

- When multiple reflections inside anisotropic parallel plates are taken into account together with the Gaussian nature of the laser beam, only the Mueller matrix can be defined (see appendix A).

- As written in ref. [24]: "*The quantum theoretical treatment of electromagnetic radiation fits in very well with the treatment of optics by means of the Stokes parameters. This is quite natural since the Stokes parameters are actually the "observable" quantities in phenomenological optics.*"

This later statement is of prime importance in our case since we are going to collide a high energy electron beam with a laser beam and then observe scattered photons.

In the rest of this document, both formalisms will be used.

2.2.2 Laser beam-electron beam interaction

Interaction between a free photon and a free electron takes place by the well known "Compton scattering" process. However, going from this elementary process to the laser beam – electron interaction is not that simple. To understand this point one has to return to former works (see [24, 25, 26] for ex.). Briefly summarising:

- The two helicity states ± 1 of the photon correspond to circular left and right wave polarisations. In Quantum Field Theory (QFT), the photon field operator can be modified, according to a unitary 2×2 matrix transformation, to describe elliptically polarised radiation (see Zeeman effects in arbitrary oriented magnetic field for ex.).

- The Stokes parameters have the same form in wave optics and in QFT. However the physics interpretation is different: in QFT, $|E_x|^2/\hbar w$ and $|E_y|^2/\hbar w$, with w the light wave angular frequency, are the number of photons per unit area unit time observed when the beam passes through linear polarisers (i.e. filters) oriented along $\hat{\mathbf{x}}$ and $\hat{\mathbf{y}}$ respectively. In wave optics $|E_x|^2$ and $|E_y|^2$ are the light intensities as stated above.

- For currently used laser beams one can assume that the photons are independent and all in the same quantum state. The laser beam-electron interaction is then reducible to the photon-electron elementary process.

To simplify our model for the laser beam-electron beam interaction, we shall further assume a mono-energetic and mono-directional electron beam. In this way, and according to the above items, the electron-photon Compton cross section will be used to describe the interaction of the two mono-energetic beams. The electron beam energy spread (of the order of one per mille of the nominal beam energy at HERA) and the beam angular spread will be taken into account in a future work.

The number of scattered photons per unit of time and solid angle in the electron rest frame (with the Z axis along the direction of motion of the electron) is given by [10]:

$$\begin{aligned}\frac{d^3 n_\gamma}{dt d\Omega} = \mathcal{L}_{\gamma e} C \Big\{ & [1 + \cos^2\theta + 2(k_i - k_f)\sin^2\frac{\theta}{2}] \\ & - [S_1 \cos 2\phi + S_2 \sin 2\phi]\sin^2\theta \\ & - 2\sin\theta \sin^2\frac{\theta}{2} S_3 [P_Y \sin\phi - P_X \cos\phi] \\ & - 2\cos\theta \sin^2\frac{\theta}{2}(k_f + k_i) S_3 P_Z \Big\}. \end{aligned} \tag{2.3}$$

where $\mathbf{k_i} = k_i \hat{\mathbf{k}}_\mathbf{i}$ and $\mathbf{k_f} = k_f \hat{\mathbf{k}}_\mathbf{f}$ are the momenta of the incident and scattered photon in the electron rest frame; θ is the angle between $\mathbf{k_i}$ and $\mathbf{k_f}$ in the electron rest frame; ϕ is the azimuthal angle (e.g. orientation of the projection of $\mathbf{k_f}$ in the plane XY) $\overrightarrow{P} = P_X \hat{\mathbf{x}} + P_Y \hat{\mathbf{y}} + P_Z \hat{\mathbf{z}}$ is the electron polarisation vector introduced in section 2.1; S_3 is the level of laser light circular polarisation; $\mathcal{L}_{\gamma e}$ is the luminosity for the laser beam-electron beam interaction (see eq. (2.4) in the next section). The global factor C reads

$$C = \frac{1}{2}\left(\frac{e^2}{m_e c^2}\frac{k_f}{k_i}\right)^2$$

where e, m_e and c are the electron electric charge, the electron mass and the light velocity respectively.

Kinematics and angular distribution of the scattered photons are extensively described in refs. [27, 28]. From these studies we see that with a high energy electron beam, the photons are scattered within a cone of a few hundreds of μrad in the direction of the

electron beam. Therefore the energy distribution can be measured completely within a small calorimeter.

Since Compton scattering is a two body[5] process, the $\cos\theta$ distribution in the electron rest frame is linearly related to the scattered photon energy distribution in the laboratory frame. Hence, from eq. (2.3) one sees that:

- For best determination of the components of $\overrightarrow{P}$ one must maximise the level of laser circular polarisation (i.e. $S_3 \rightarrow \pm 1$) and thus minimise the level of linear polarisation (i.e. $\sqrt{S_1^2 + S_2^2} \rightarrow 0$).

- Knowing the laser beam polarisation, the electron longitudinal polarisation can be determined by a fit to the distribution of the scattered photon energy (after integration over the azimuth angle). To determine the transverse polarisation, one must measure both the energy and the azimuth angle ϕ although it is expected to be very small in the region where the longitudinal polarisation is measured (between a pair of spin rotators).

For obvious reasons, an accurate measurement of the longitudinal polarisation is easier to perform.

2.2.3 Polarisation measurement modes

Assuming a Gaussian shape for the electron beam and the laser beam intensity, expressions for the laser beam-electron beam luminosity $\mathcal{L}_{\gamma e}$ have been calculated in ref. [27]. For a non-vanishing electron-laser beam crossing angle α, they obtained the total luminosity (integrated over the space variables):

$$\mathcal{L}_{\gamma e} \approx \frac{1}{\sqrt{2\pi}} \frac{1+\cos\alpha}{\sin\alpha} \frac{I_e}{ec} \frac{P_{laser}\lambda}{hc} \frac{1}{\sigma_{ex}^2 + \sigma_\gamma^2} \tag{2.4}$$

where σ_{ex} and σ_γ are the electron beam radius along the x axis and the laser beam radius (see appendix 3.6.1 of chap. 3) respectively; P_{laser} is the laser beam power; I_e is the electron beam current. Note that eq. 2.4 assumes that the plane of interaction of the electron and laser beams is vertical (along y).

In a storage ring where electron bunches are separated by Δt in time, the number of back-scattered photons per bunch in then given by

$$n_\gamma/bunch = \Delta t \iint \frac{d^3 n_\gamma}{dt d\Omega} d\Omega.$$

Depending on the value of n_γ, one can define three different measurement modes:

- Single photon mode: $n_\gamma \ll 1$

- Few photon mode: $n_\gamma \approx 1$

- Multi photon mode: $n_\gamma \gg 1$.

[5] At HERA the centre of mass energy of the Compton process is below the pair mass threshold (i.e. e^+e^- pair cannot be created).

When $n_\gamma \gg 1$, the statistical uncertainty on the measurement of the longitudinal polarisation is better as well as the ratio of the signal to background. But, in fact, high values of n_γ induce large systematics on the scattered photon energy measurement and therefore the few photon mode appears to be a good compromise between the single and the multi photon modes. In addition, a high energy pulsed laser beam in needed for the multi photon mode and the laser beam transport and diagnostics are not easy for such beams so that additional systematic bias may thus appear.

Mathematical details of the statistical analysis leading to the determination of P_Z in these three modes are given in appendix 2.3. In this section, we briefly discuss the advantages and disadvantages of these three modes. A detailed description of the few-photon mode polarisation measurement is given in section 2.2.4. This mode was not considered by previous experiments, this is our original contribution in this field.

For the three modes of polarisation measurement, one must supply an experimental setup similar to the one shown in fig. 2.13, that is: a photon extraction line and a calorimeter to measure the energy and beam position if the determination of P_X and/or P_Y is foreseen. In such experiments, the two main backgrounds are: beam-gas bremsstrahlung and beam-blackbody radiation Compton scattering (see section 2.2.4 for details).

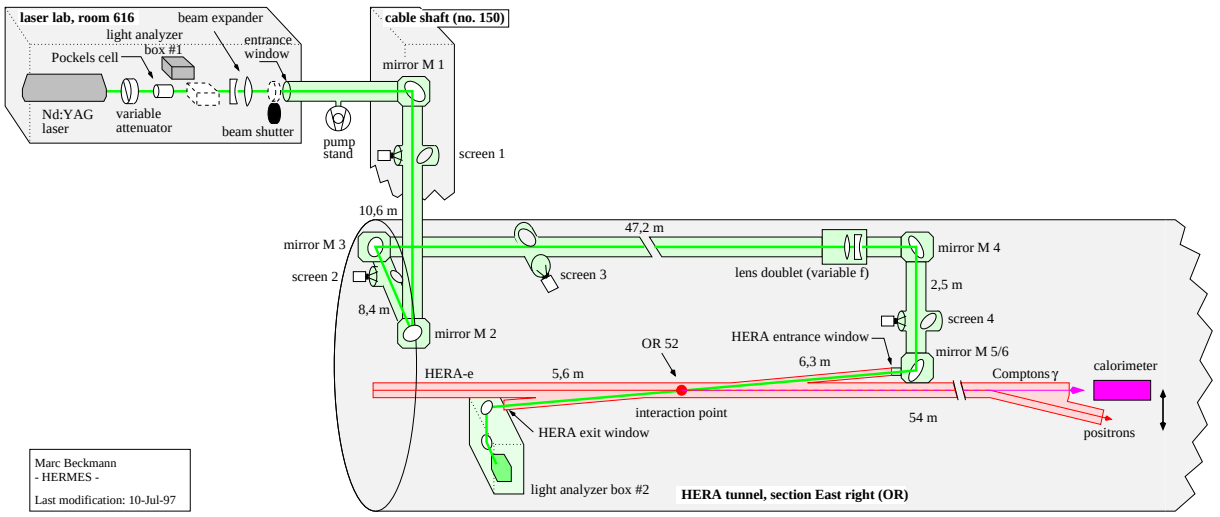

Figure 2.13: *Layout of the present longitudinal polarimeter at HERA. The laser beam is brought inside the electron vacuum beam pipe by an entrance window. Compton photons are scattered in the direction of the electron beam within a very narrow angular cone. Back-scattered photons escape the beam pipe through an exit window located at the end of the right section and enter a calorimeter ≈ 60 m downstream from the laser beam-electron beam interaction point (IP). An optical bench is located on the other side of the IP to stop the laser beam and to measure the light polarisation.*

Single photon mode

In this mode, the probability that two Compton scatterings occur within a single bunch crossing is negligible. Therefore eq. (2.3) can be used to fit the experimental data.

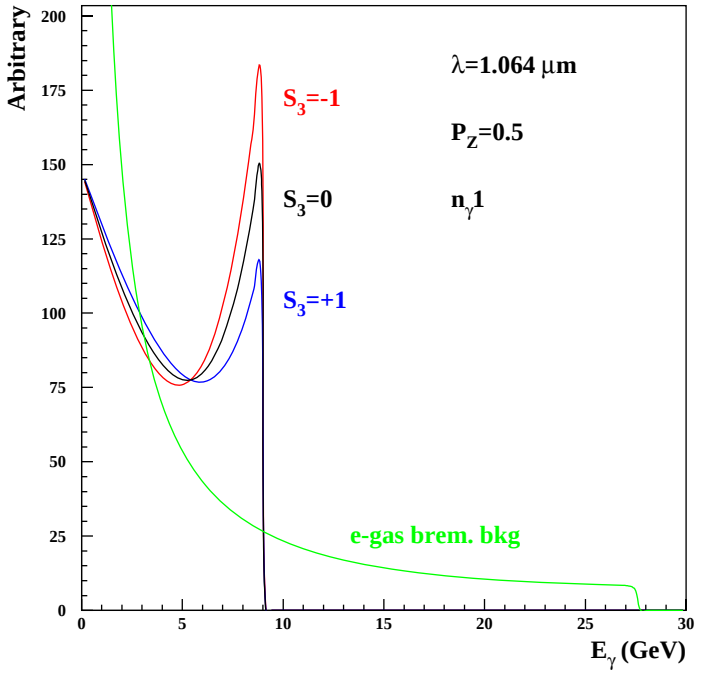

Figure 2.14: *Back-scattered Compton photon energy spectra for three values of the laser degree of circular polarisation $S_3 = 0, \pm 1$. Also shown is the electron beam - gas bremsstrahlung background for an electron beam energy of 27.5 GeV. Relative normalisations between Compton and bremsstrahlung spectra are arbitrary and no detector effect has been taken into account.*

Fig. 2.14 shows the energy distributions calculated with eq. (2.3) for $P_Z = 0.5$ and $S_3 = \pm 1$ using the HERA electron beam energy (27.5 GeV) and the ND:YAG laser beam wavelength $\lambda = 1.064\mu$m. From this figure one sees that the sensitivity to P_Z is mainly located in the high energy region of the spectrum. Calorimeters operating in the range 1-10 GeV are then required. In fig. 2.14, the edge of the Compton energy distribution comes from the kinematic limit of the Compton scattering.

To discuss the performance of the single photon mode, let us describe the present TPOL measurement setup at HERA [10]. A 10 W laser with green light is used and $n_\gamma \approx 0.01/bunch$. The calorimeter is segmented in two parts in the vertical direction so that the total photon energy and the vertical position of the photon impact can be reconstructed simultaneously.

A description of the data analysis leading to the measurement of P_Y is outside the scope of this work (see[10]) . What is interesting to mention here is that P_Y is measured at a few percent level. This accuracy is limited by: the knowledge of the electron beam shape, the determination of the y position from the energy measurements, the statistics. Currently, the statistical precision of the HERA-TPOL measurement is $\approx 10\%$ per bunch and per minute.

The advantage of the single photon mode is that one can calibrate the calorimeter absolutely using the Compton edge (and the bremsstrahlung edge, see fig. 2.14). With the recent upgrade of the HERA-TPOL data acquisition system, the accuracy on the absolute calibration is below 0.5% and controlled on a 1 min time base. The disadvantage of this mode is the low statistics due to low luminosity. In the case of large background levels, the signal may also be too diluted thereby reducing the polarisation measurement accuracy.

From the performances of the TPOL measurement in the single photon mode, one sees that the accuracy of the longitudinal polarisation measurement would be limited by statistics in this mode.

Few photon mode

To extract the longitudinal polarisation, one proceeds as in the single photon mode except that we must now consider a Poissonian superposition of back-scattered photons. Multi-convolutions of eq. (2.3) must then be calculated and a fit has to be performed to the experimental data. Fig. 2.15 shows the energy distributions in the few photon modes. Comparing with the single photon mode one can remark the presence of the double Compton edge and a high energy tail. This means that one gets three points to perform an absolute calibration of the calorimeter: the two Compton edges (and the bremsstrahlung edge, see fig. 2.14). This allows a survey of the calorimeter linearity.

For longitudinal polarisation, we proved that non-linear fits are numerically stable and reproduce the experimental distributions (within the accuracy of these measurements, see appendix 2.3)

Experimentally one must use a very high continuous laser beam power (typically a few kW) to reach $n_\gamma/bunch \approx 1$. Nevertheless, special experimental setups are feasible as will be shown in chap. 3.

With respect to the single photon mode, advantages of this method are threefold: first the statistics is large, second the ratio signal to background is better and third single and double Compton edges can be used to calibrate the calorimeter. Very precise longitudinal

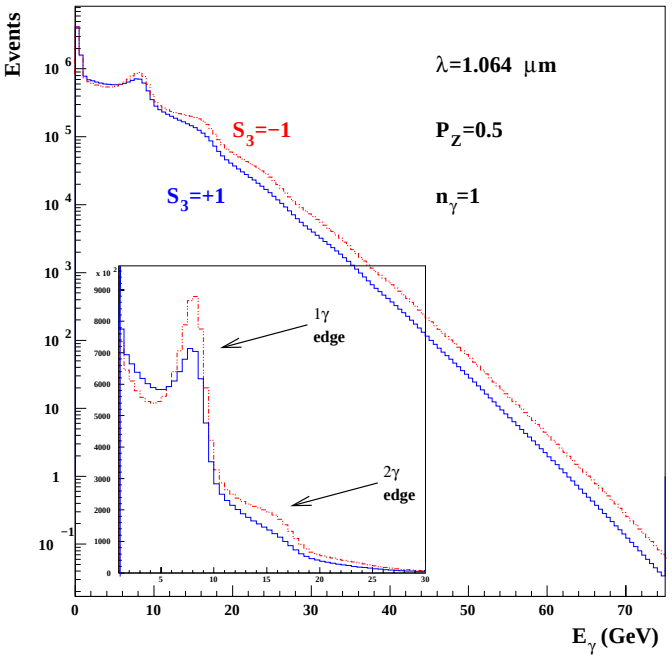

Figure 2.15: *Compton energy spectra for $S_3 = \pm 1$ in the few photon mode ($n_\gamma/bunch = 1$). Distributions are shown on linear and logarithmic scales to exhibit the long energy tail. Gaussian smearing of the photon energy has been applied as indicated in appendix 2.3.*

polarisation measurement (below $1\%/bunch/min$) can then be achieved in principle. The disadvantage is that one has to perform a non-linear fit, but it turns out that this is more a numerical difficulty than a disadvantage.

Multi photon mode

When the background is large, or when the polarisation needs to be known after a single bunch crossing (i.e. at linear colliders), high energy pulsed lasers are used. After a bunch-laser beam interaction a large number photons are back-scattered, typically $\approx 1000/bunch$.

One can then apply the limit theorem so that $\overrightarrow{P}$ is obtained from the measurement of the average energy and average impact position in the calorimeter. The averages are linear forms of the $\overrightarrow{P}$ components. To illustrate the measurement of P_Z in this mode, experimental energy distributions taken by the HERA-LPOL are shown in fig. 2.16. The longitudinal polarisation is linearly proportional to the difference between the two distributions obtained with a laser beam polarised circular left and right.

The disadvantage of this mode is that a total energy ~ 10 TeV is seen by the calorimeter. Since the energy calibration of the calorimeter is done using low energy beam electrons (and the single photon Compton edge), the polarisation measurement is affected by a systematic uncertainty of the order of a few percent [6]. Another difference compared with the

[6] At LEP, the transverse polarisation was measured in the multi-photon mode [29] and an overall systematic uncertainty of 15% was quoted [30] (which was not a limiting factor since the polarimeter was

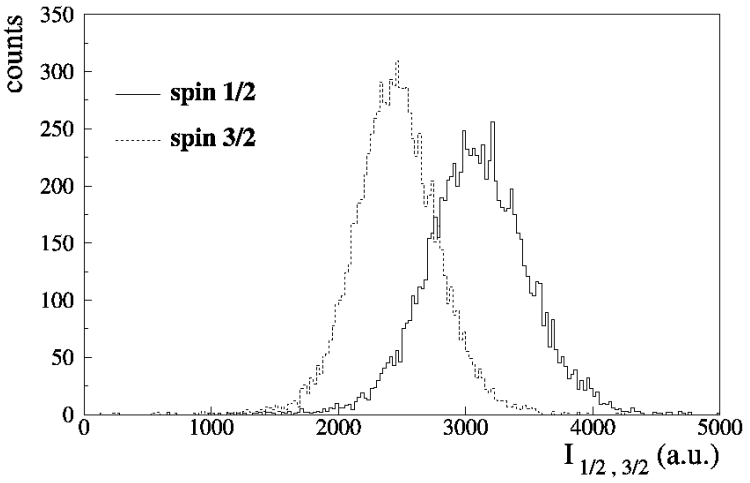

Figure 2.16: *HERA-LPOL experimental photon energy distributions for $S_3 = +1$ (spin 3/2 in the plot) and $S_3 = -1$ (spin 1/2 in the plot). From [12].*

two other modes is that one cannot extract the polarisation without combining the two photon energy spectra corresponding to the laser beam left and right polarisation. The statistics is limited by the laser pulse frequency (100 Hz maximum for the HERA-LPOL) this leads to a statistical precision of the present HERA-LPOL comparable to the one of the HERA-TPOL (see above).

Before ending this section, it should be mentioned that in linear colliders it is possible to detect the scattered electron instead of the scattered photons. The advantage is twofold: the polarisation information is carried by the lower part of the electron energy spectrum and the use of a spectrometer leads to a measurement of both the scattered angle and the energy. This redundancy led to the high precision longitudinal polarisation measurement at SLAC-SLC [7] using a high power pulsed laser.

Since we are detecting the scattered photons at HERA, in order to reach the per mille level on the statistical and systematic accuracies on the longitudinal polarisation measurement, we choose to use the few photon mode. The rest of the chapter is devoted to a more detailed description of the few photon mode.

2.2.4 Polarisation measurement in the few photon mode

In this section we present the basic formula used in our studies. Our "experimental setups" are also described there. Next, a numerical study, describing the performance of the LPOL measurement in the few photon mode is presented. This study was performed for our proposal of the LPOL ugrade.

Signal

For a longitudinally polarised electron beam, the Compton scattering differential cross-section is obtained from eq. (2.3). In the laboratory rest frame and as a function of the

used to measure the beam energy by depolarisation resonances [31]).

back-scattered Compton photon (BCP) energy one gets (see eq. (8) of [10], we won't give here the complete expression which is obtained by elementary algebra from eq. (2.3)):

$$\frac{d\sigma_c}{dE_\gamma} = \frac{d\sigma_0}{dE_\gamma} + S_3 P \frac{d\sigma_Z}{dE_\gamma} \tag{2.5}$$

where $S_3 = -1$ for a circular-right polarised laser beam and $S_3 = +1$ for a circular-left laser beam; P is the electron beam LPOL; E_γ is the BCP energy in the lab. frame. $d\sigma_0/dE_\gamma$ and $d\sigma_z/dE_\gamma$ are two functions of E_γ and of the lepton and laser beam energies, E_e E_λ respectively.

In our numerical studies we shall use $E_\lambda = 1.165$ eV (the ND:YAG laser energy) and E_e =27.5 GeV.

Beam Gas bremsstrahlung background

The differential cross section $d\sigma(e + g \to e + g + \gamma)/dE_\gamma$ - where g stands for the residual gas in the beam pipe - is described by eq. (1) of ref. [32]:

$$\frac{d\sigma_{eg}}{dE_\gamma} = 4\alpha r_e^2 \frac{E_{e'}}{E_e E_\gamma}\left[\left(\frac{E_e^2 + E_{e'}^2}{E_e E_{e'}} - \frac{2}{3}\right)[Z^2 \ln(184.15 Z^{-1/3}) + Z \ln(1194 Z^{-2/3})] + \frac{1}{9}(Z^2 + Z)\right] \tag{2.6}$$

where $E_{e'} = E_e - E_\gamma$; r_e is the electron classical radius and $\alpha = 1/137$. The mean atomic number of the residual gas nucleus is taken to be $Z = 4.2$ [32].

A more complete formula [33] has also been implemented in our numerical program.

Compton-blackbody scattering background

This background is extensively described in ref. [34] where it has been studied using the TPOL set-up. It consists of blackbody photons radiated by the beam pipe (T≈ 310 K). A rate of 0.013/bunch for a current of 0.3mA/bunch has been reported. However, the LPOL interaction point is located after 50m of an HERA straight section (to be compared to 7.3m for the TPOL where a weak dipole deviates the beam). Therefore, with an electron beam current of 40 mA and 190 bunches, one expects a rate of ≈ 0.06 photons per bunch for LPOL.

To describe this background we shall follow the calculations of ref. [34] to which we refer for more details.
The blackbody energy spectrum (in the lab. frame) is given by:

$$\frac{dn(E_\lambda)}{dE_\lambda} \propto \frac{E_\lambda^2}{e^{E_\lambda/k_B T} - 1}$$

where k_B is the Boltzmann constant. The energy distribution of the blackbody photon scattered by the electron beam (in the lab. frame) is given by

$$\frac{dn(E_\gamma)}{dE_\gamma} \propto \int_{(\cos\theta_\lambda)_{min}}^{1} \int_{E_{\lambda,min}}^{E_{\lambda,max}} \frac{dn(E_\lambda)}{dE_\lambda}(1 + \beta\cos\theta_\lambda)\frac{d\sigma_c}{dE_\gamma} dE_\lambda d\cos\theta_\lambda \tag{2.7}$$

where:

- θ_λ is the angle between the incoming blackbody photon and the electron beam direction in the lab. frame;
- $\beta \approx 1$ is the electron beam velocity;
- $E_{\lambda,max}$ is infinite in principle but it suffices – for the numerical computation of the integral – to take $E_{\lambda,max} \approx E_{\lambda,min} + 12 \times k_B T$;
- $d\sigma_0/dE_\gamma$ is the unpolarised Compton differential cross-section (c.f. eq. (2.5)) including both E_λ and θ dependences;
- the lower bound of the integral is given by the kinematic relations:

$$(\cos\theta)_{min} = \frac{m_e k_{i,min}}{\beta\gamma E_{\lambda,max}} - \frac{1}{\beta} \; ; \; E_{\lambda,min} = \frac{m_e k_{i,min}}{\gamma(1+\beta\cos\theta_\lambda)}$$

  with $\gamma = 1/\sqrt{1-\beta^2}$ and $k_{i,min} = E_\lambda/2(E_e - E_\lambda)$.
- the proportionality factor is not important since we normalised the amount of events to the integral over the energy (from 0 to 3 GeV).

The maximum energy reached by the scattered blackbody photon is given by

$$E_{\gamma,max} = \frac{E_e}{1 + \frac{m_e}{2\gamma E_{\lambda,max}(1+\beta)}}$$

and amounts to ≈ 3 GeV for $E_{\lambda,max} = 0.3$ eV.

Synchrotron radiation background

All details concerning the synchrotron radiation around the IP of the LPOL can be found in ref. [35]. Here we just briefly summarise the main features related to this background.

The IP is located inside the HERA 90BH bending magnet. The calorimeter is then illuminated by synchrotron radiation which is made of a large number of low energy photons (the total reaches ≈ 1 TeV). A lead plate is located in front of the calorimeter so that only 100 MeV is seen in the detector. We shall not consider this background in the present study since it appears as an energy pedestal in the calorimeter and can thus be determined experimentally [34]. The effect of the lead plate on the resolution will be studied by varying the energy resolution of the calorimeter.

Measurement set-up

To extract the electron longitudinal polarisation, we shall adopt the usual measurement procedure. The following three measurements are performed successively:

1. Laser off: background energy distribution is measured (eqs. (2.6,2.7)).
2. Laser beam circular left polarised (=Laser left): signal measurement with $S = +1$ (eq. (2.5), pile-up with backgrounds of (eqs. (2.6,2.7)) is included.
3. Laser beam circular right polarised (=Laser right): signal measurement with $S = -1$ (eq. (2.5), pile-up with backgrounds of (eqs. (2.6,2.7)) is included.

With a 10 MHz data acquisition system, one can consider at most $\approx 3 \cdot 10^6$ records per minute for each electron bunch and each of the three experiments. These records contain any kind of background or signal photons and even electronic noise (e.g. electronic pedestals).

Note that, once the backgrounds are understood, only one experiment (laser left or right) is required in principle to determine the polarisation.

2.2.5 Numerical studies

Mathematical expressions of the statistical estimators that can be used to extract the longitudinal polarisation are given in appendix 2.3.

We shall concentrate here on the few photon mode and therefore use the estimator #1 of the appendix 2.3 (= a Likelihood fit to the scattered photon energy spectrum). A fitting programme has been written and tested with experimental data of the HERA-LPOL. These data were taken by "reducing" the power from the HERA-LPOL pulsed laser. However, since the electronics, the laser operation mode (i.e. pulse delay) and the calorimeter are designed for the multi photon mode, the data quality is not optimum for the single and the few photon modes. This feature is illustrated by the top plots of figs. 2.17 and 2.18 where the background fits are compared to the laser off measured energy distributions. The very large Gaussian centred at 0 is the pedestal distribution which extends up to the bremsstrahlung edge. In any case, by fitting these distributions one finds $P \approx -0.55$ and $n_\gamma \approx 1.5$, 6 for figs. 2.17 and 2.18 respectively. Fit results are shown together with experimental data and it is important to note that the high energy tails are well described. Notice that the two laser-on distributions of fig. 2.18 are not Gaussian.

We have performed a series of studies to estimate the accuracy of a longitudinal polarisation measurement in the few photon mode considering a ND:YAG laser (wavelength $\lambda = 1.064\mu$m). Laser off, left and right energy histograms for one electron bunch are computed varying n_γ and P. The number of entries correspond to 6s DAQ period, i.e. $\approx 6 \cdot 10^6$ DAQ events. Next a fit using estimator #1 is performed and both P and its uncertainty are determined.

The absolute statistical accuracy ΔP obtained from this analysis is presented in fig. 2.19 for $P = 0.5$ and two bremsstrahlung background rates describing the range presently observed in the HERA-LPOL region. For $n_\gamma > 0.3$ one sees that a statistical accuracy below $1\%/bunch/min$ is reached. However, using eq. (2.4) one finds that this number corresponds to a ND:YAG laser power of $\approx 20kW$ for a 1 mA electron beam current (that is $\approx 500W$ for 40 mA) and a laser-electron crossing angle of 58 mrad.

Using our numerical programme, we can also estimate the main systematic uncertainties. To do so, the calorimeter energy response is modelled by a Gaussian of width $\sigma = 14.4\%\sqrt{E} \oplus 0.435\%E$ corresponding to the new calorimeter. Three Compton rates $n_\gamma/bunch = 0.1$, 1, 2 and eight values of the electron beam polarisation $P = 0, 0.1, ..., 0.8$ are chosen. The following effects have been studied:

- Uncertainty on the linear calibration constant: taking a scale uncertainty of 0.5%[7], the systematic shifts of the polarisation measurements are below 0.1%.

- Uncertainty due to non-linearity: taking a non-linearity of 1% at 20 GeV, the systematic shifts of the polarisation measurements are shown in fig. 2.20. The effect is

[7] This is the present uncertainty quoted by the HERA-TPOL, see section 2.2.3

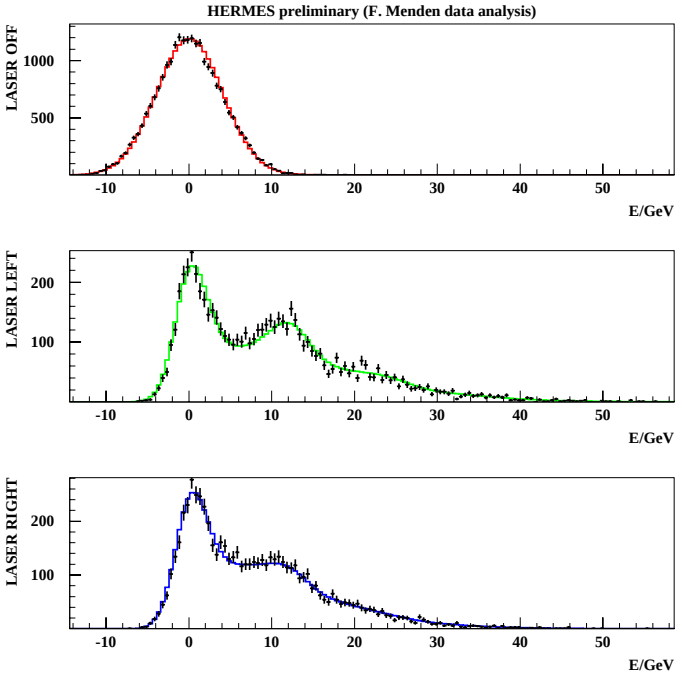

Figure 2.17: *Data taken at the HERA-LPOL by the HERMES Collaboration (crosses). Upper plot is the observed laser off energy distribution, lower plots are the laser on experiments. Laser wavelength is* $\lambda = 0.5\mu$m *and electron beam energy* $E_e = 27.5GeV$. *Full lines show the results of a fit to the experimental data.*

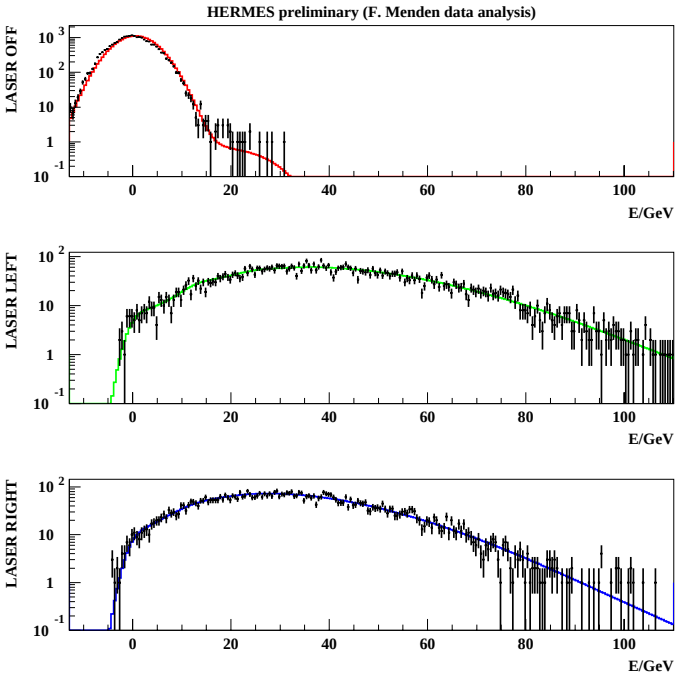

Figure 2.18: *As fig. 2.17 but for a higher laser pulse energy and a vertical logarithmic scale.*

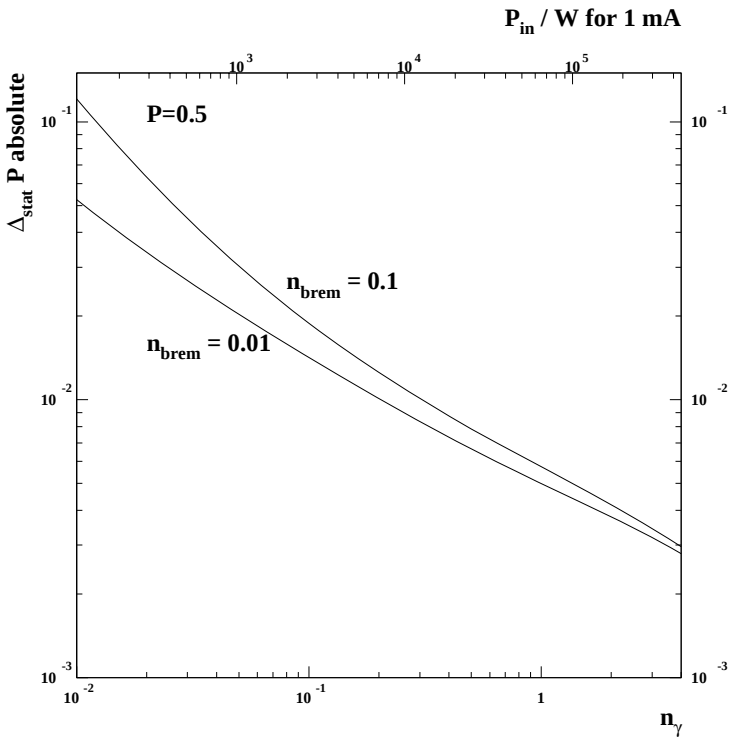

Figure 2.19: *Statistical uncertainty of the polarisation per bunch and per minute as a function of the number of back-scattered photons, n_γ. Two curves are shown for two different background levels of 1% and 10%. Also shown is the laser power needed to obtain a given number of back-scattered photons, assuming a crossing angle of 58 mrad.*

large, especially for a large event rate. Fig. 2.21 shows the numerical derivative of the energy distributions with and without 1% non-linearity. Using the three points (1γ, 2γ and bremsstrahlung kinematic edges), such an effect can be controlled at a few per mille level so that the remaining systematic uncertainty on the polarisation measurement can be reduced at a few per mille level as well.

- Uncertainty due to the knowledge of the dead material in front of the calorimeter: to estimate this effect we have generated the energy spectra taking into account 2X0 of lead (model of ref. [36] is used) and perform the fits without it. The systematic shifts obtained for the polarisation measurements are shown in fig. 2.22. This is an important effect. Our example is not realistic but it shows that a precise control and modelling of effects of dead materials is necessary.

From this study we conclude that an accuracy at the few per mille level can be achieved in the few photon mode. A longitudinal polarimeter operating in this mode is then adequate for the HERA-II physics programme. A precise control of the calorimeter response and material is however mandatory.

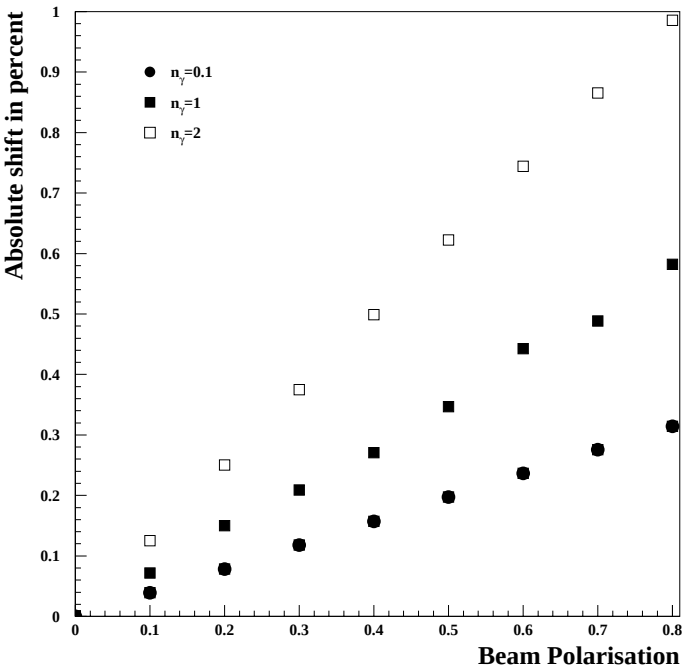

Figure 2.20: *Systematic shift of the polarisation measurement induced by 1% calorimetric non-linearity at 20 GeV.*

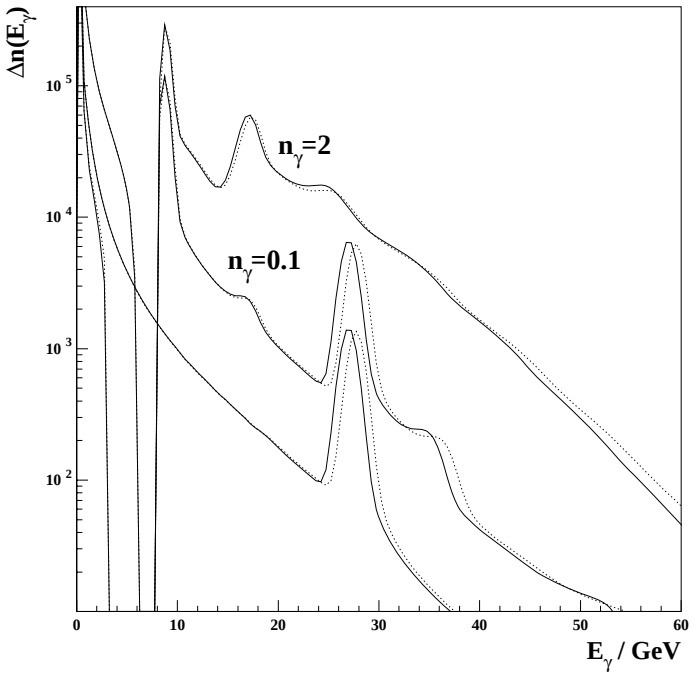

Figure 2.21: *Numerical derivatives of the energy distributions for a perfect detector (full curves) and including a 1% non-linear calibration factor (dashed curves). The lower curve is the laser-off distribution. The numerical deivatives shown in this figure are simply obtained by subtracting the containts of all pairs of adjacent bins of the photon energy spectra.*

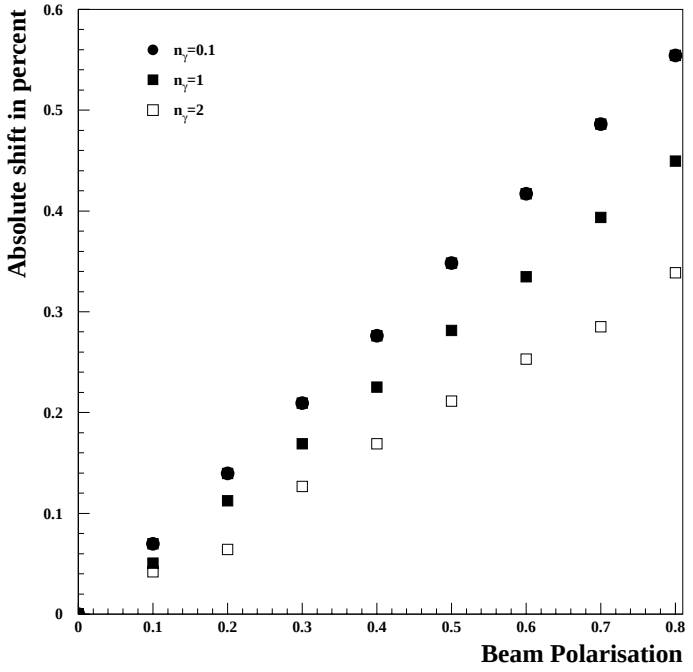

Figure 2.22: *Systematic shift of the polarisation measurement induced by ignoring the two radiation lengths of lead in the fit (see text).*

2.3 Appendix

This appendix is a revised version of an internal note written by C. Pascaud and myself. It describes the statistical analysis of the back-scattered Compton photons (BCP) energy distribution in the three modes defined in section 2.2.3. We thus construct some statistical estimators from a model of the BCP energy spectrum. Since our statistical treatment for the few photon mode cannot be found in the literature, details are given here.

2.3.1 Statistical estimators

Notations

In order to introduce our notations let us first consider the single-photon mode. Let us also consider one of the three experiments defined in the previous section. In this case there is, at most, one photon observed in the calorimeter. Then, after one period T_{DAQ} of Data Acquisition (DAQ), the average number of events of energy between E and $E + \Delta E$ is:

$$n_{1\gamma}(i, n, e, E) = \sum_{k=1}^{3} a_k(n, i) \times \epsilon_k^e \times f_k(E) \tag{2.8}$$

where i stands for the bunch number; n is the number of DAQ periods accumulated since the beginning of the luminosity run ($n \times T_{DAQ}$ is the total elapsed time); e is the experiment index ($e = 1, 2, 3$); the constants a_k will be determined by the fit, they are defined by

$$\begin{aligned} a_1(n, i) &= \mathcal{L}_B(n, i) \times T_{DAQ} \\ a_2(n, i) &= \mathcal{L}_c(n, i) \times T_{DAQ} \\ a_3(n, i) &= P(n, i) \times \mathcal{L}_c(n, i) \times T_{DAQ}\,; \end{aligned} \tag{2.9}$$

$\mathcal{L}_B(n, i)$ and $\mathcal{L}_c(n, i)$ are the background (electron beam - residual gas and electron beam - blackbody photons interactions) [8] and electron beam-laser beam luminosities respectively, they are defined for each bunch i and are functions of the elapsed time nT_{DAQ}. $f_1(E)$ is the background energy distribution; $f_2(E)$ is the energy distribution for unpolarised electrons; $f_2(E) + f_3(E)$ is the energy distribution for totally polarised electrons and laser beam circular left polarised ($P = +1$); ϵ_k^e characterises the three experiments described in the previous section and has the following values:

- $\epsilon_k^1 = 1, 0, 0$ Laser off;
- $\epsilon_k^2 = 1, 1, 1$ Laser left;
- $\epsilon_k^3 = 1, 1, -1$ Laser right.

f_1, f_2 and f_3 can be determined by a full simulation of the detector response to the BCP and to the background. To be explicit we give here the expressions of these functions

[8] In fact there is one parameter a per background source. In order to simplify the presentation we choose to gather all these parameters into a single one.

in the case of the single-photon mode. Neglecting for now any detector effects, one has:

$$\begin{aligned} f_1(E) &= \int_E^{E+\Delta E} \frac{d\sigma_B}{dE'} dE' \\ f_2(E) &= \int_E^{E+\Delta E} \frac{d\sigma_0}{dE'} dE' \\ f_3(E) &= \int_E^{E+\Delta E} \frac{d\sigma_Z}{dE'} dE' \end{aligned} \tag{2.10}$$

However, in the general case the number of photons observed in the detector is not fixed. Some complex mixtures are expected: one (or more) BCP can occur together with one (or more) background event. We shall now turn to the description of this general case.

Probability for the number of photons per bunch-crossing

We drop now the bunch and elapsed time indexes. The average number of photons observed in the detector after **one bunch-crossing** for one experiment set-up e is given by

$$M_e = \int_0^{\infty} \frac{dm_e(E)}{dE} dE \tag{2.11}$$

where $dm_e(E)/dE$ is simply obtained by dropping the integral over the energy in the expressions of f_k (see eq. (2.10)).

The fluctuations of M_e following a Poissonian law, one has:

- $\mathcal{P}_0 = e^{-M_e}$ is the probability to have 0 photons when one expects M_e;
- $\mathcal{P}_N = e^{-M_e} \frac{M_e^N}{N!}$ is the probability to have N photons when one expects M_e.

In the following we shall drop the experiment index e.

Probability for an energy measurement per bunch-crossing

Once a given photon i is observed, the probability to find it with an energy between E_i and $E_i + \Delta E_i$ is $m(E_i)/M$. Hence, the probability to get N photons of energies between E_i and $E_i + \Delta E_i$, $i = 1, \ldots, N$ is :

$$\mathcal{P}_N \prod_{i=1}^{N} \frac{m(E_i)}{M} = \frac{e^{-M}}{N!} \prod_{i=1}^{N} m(E_i) \tag{2.12}$$

In our case only the total energy $E = \sum_1^N E_i$ is measured. Using eq. (2.12), we can write the probability to get N photons with total energy between E and $E + \Delta E$ as follows

$$e^{-M} \frac{m_N(E)}{N!}$$

with

$$
\begin{aligned}
m_i(E) &= \int_E^{E+\Delta E} \frac{dm_i(E')}{dE'} dE' \,, \\
\frac{dm_i(E)}{dE} &= \int_0^{E_e} \cdots \int_0^{E_e} \delta(E - \sum_{k=1}^{i} E_k) \prod_{k=1}^{i} \frac{dm(E_k)}{dE_k} dE_k \,.
\end{aligned}
\tag{2.13}
$$

Explicitly, we have

$$
\begin{aligned}
m_1(E) &= \int_E^{E+\Delta E} \frac{dm(E')}{dE'} dE' \\
m_2(E) &= \int_E^{E+\Delta E} \int_{max(0,E'-E_e)}^{min(E_e,E')} \frac{\partial m(E'-E'')}{\partial E'} \times \frac{dm(E'')}{dE''} dE'' dE' \equiv m \otimes m \\
&\vdots \\
m_N(E) &= \int_E^{E+\Delta E} \int_{max(0,E'-N\times E_e)}^{min(E_e,E')} \frac{\partial m_{N-1}(E'-E'')}{\partial E'} \times \frac{dm(E'')}{dE''} dE'' dE' \equiv m \otimes m ... \otimes m
\end{aligned}
\tag{2.14}
$$

where we have used $dm(E'-E'')/d(E'-E'') = \partial m(E'-E'')/\partial E'$ and where the symbol $\otimes$ is introduced for convenience.

Finally the probability to receive in the detector an energy between E and $E+\Delta E$ is:

$$
\int_E^{E+\Delta E} \frac{d\mathcal{P}(E')}{dE'} dE' = e^{-M} \sum_{i=1}^{\infty} \frac{m_i(E)}{i!}. \tag{2.15}
$$

The detector response is modelled by a Gaussian of width $\sigma_E = \alpha\sqrt{E} + \sigma_p$ where σ_p represents the pedestal effect. Possible bias of the energy scale is taken into account by using two real parameters β and γ (see eq. (2.16)). Functions m_i must then be replaced by the smeared functions:

$$
\frac{d\tilde{m}_i(E)}{dE} = \int_0^{+\infty} \frac{dm_i(E')}{dE'} \times \frac{e^{-\frac{[E(1+\beta+\gamma E]-E')^2}{2\sigma_{E'}^2}}}{\sqrt{2\pi}\sigma_{E'}} dE'. \tag{2.16}
$$

Even when no photon enters the calorimeter, because of pedestal, one may measure a non-vanishing energy. We must then extend the range of the index i down to 0 and introduce

$$
\frac{dm_0}{dE} = \delta(E)
$$

in eqs. (2.13,2.14). With this change and extensions, the probability to "measure" in the detector an energy between E and $E+\Delta E$ is:

$$
\int_E^{E+\Delta E} \frac{d\mathcal{P}(E')}{dE'} dE' = e^{-M} \sum_{i=0}^{\infty} \frac{m_i(E)}{i!} = \mathcal{P}_0 \times \int_E^{E+\Delta E} \frac{d\Psi(E')}{dE'} dE', \tag{2.17}
$$

where the last equality serves as a definition of the function Ψ that we shall use below. Eq. (2.17) is normalised as follows:

$$\int_0^\infty \frac{d\mathcal{P}(E)}{dE} dE = 1\,. \tag{2.18}$$

Proof:
Integrating eq. (2.13) and using eq.(2.11) one gets

$$\int_0^\infty \frac{dm_i(E)}{dE} dE = \prod_{k=1}^{i} \int_0^{E_e} \frac{dm(E_k)}{dE_k} dE_k = M^i \tag{2.19}$$

so that

$$\int_0^\infty \frac{d\mathcal{P}(E)}{dE} dE = e^{-M} \sum_{i=0}^{\infty} \frac{M^i}{i!} = e^{-M} \times e^M = 1\,. \tag{2.20}$$

Estimator #1: Likelihood of the energy distributions

This first estimator is a likelihood maximisation of the energy distributions. In order to simplify the mathematical expressions, let us consider one of the three experiments described in section 2.2.4. During one DAQ period T_{DAQ} we assume that there is a sampling of S measurements (per electron bunch), S being fixed and known. The Likelihood density δL of such an experiment is given by:

$$\delta L = \prod_{i=1}^{S} \frac{d\mathcal{P}(E_i)}{dE_i}\,. \tag{2.21}$$

To show how this likelihood density is normalised we turn to the dimensionless likelihood and reformulate eq. (2.21) as follows:

$$L = \prod_{i=1}^{S} \left\{ \sum_{k=0}^{K} \mathcal{P}_k h_i^k \right\}$$

with

$$\mathcal{P}_k = \int_{E_k}^{E_{k+1}} \frac{d\mathcal{P}(E)}{dE} dE\,,$$

where the E_k are a set of energies increasing with k and ranging from $-\infty$ for $k = 0$ to $+\infty$ for $k = K$.
The integer variable h_i^k characterises the i^{th} event: $h_i^k = 1$ if the measured energy is between E_k and E_{k+1} and 0 otherwise. For an event i there is only one value of k such $h_i^k \neq 0$; this can be expressed by:

$$\sum_{k=0}^{K} \mathcal{P}_k h_i^k = 1 \tag{2.22}$$

then eq. (2.18) may be rewritten:

$$\sum_{k=0}^{K} \mathcal{P}_k \mathcal{P}_k = 1$$

We see that L is as a function of the variables h_i^k. Its normalisation is obtained by summing over the h_i^k under the constraint of eq. (2.22):

$$\sum_{h_1^0=0}^{1}\sum_{h_1^1=0}^{1}\cdots\sum_{h_S^0=0}^{1}\sum_{h_S^1=0}^{1}\cdots\prod_{i=1}^{S}\left\{\sum_{k=0}^{K}\mathcal{P}_k h_i^k\right\} = 1 \tag{2.23}$$

Proof:
We start by performing all the sums related to a given event j. As only the factor concerning the event j depends on that variable we may rewrite eq. (2.23) as follows:

$$\left\{\sum_{h_1^0=0}^{1}\sum_{h_1^1=0}^{1}\cdots\sum_{h_S^0=0}^{1}\sum_{h_S^0=1}^{1}\cdots\prod_{i\neq j}^{S}\left[\sum_{k=0}^{K}\mathcal{P}_k h_i^k\right]\right\}\left\{\sum_{h_j^0=0}^{1}\sum_{h_j^1=0}^{1}\ldots\left[\sum_{k=0}^{K}\mathcal{P}_k h_j^k\right]\right\} = 1$$

Using $\{\ h_j^k = 1 \Rightarrow h_j^l = 0 \text{ for } l \neq k\}$ we obtain

$$\sum_{h_j^0=0}^{1}\sum_{h_j^0=1}^{1}\ldots\left[\sum_{k=0}^{K}\mathcal{P}_k h_j^k\right] = \sum_{k=0}^{K}\mathcal{P}_k\mathcal{P}_k$$

which is equal to 1. Finally, working out all the events we arrive at the expected result of eq. (2.23).

Let us now look at the practical use of eq. (2.21). To be explicit, let us re-introduce the experiment index. Instead of δL we shall consider

$$\delta W \equiv -2\ln\delta L = 2\sum_{e=1}^{3}\left\{S_e M_e - \sum_{i=1}^{S_e}\ln\left(\frac{d\Psi_e(E_i)}{dE_i}\right)\right\}.$$

In fact the measured events will not be kept individually by the acquisition system but rather put in an histogram. H bins covering the energy range E_0 to E_H are then defined. With

$$\Psi'_k = \frac{\int_{E_{k-1}}^{E_k}\Psi(E)dE}{E_k - E_{k-1}},$$

we get

$$\boxed{W = 2\left(SM - \sum_{h=1}^{H} N_h \ln\Psi'_h\right),} \tag{2.24}$$

where N_h is the number of events contained in the bin h (this quantity is measured experimentally). Notice that in eq. (2.24) there is an implicit sum over the three experiments.

In eq. (2.24) we have omitted two contributions which do not depend upon the parameters a_k:

- a combinatorial factor $\ln(S!\prod_{h=1}^{H} N_h!)$, which comes from the fact that one would get the same histogram from two experiments differing only by interchange of events i and j;

- a sum over the bin widths $\ln(E_h - E_{h-1})$.

The parameters to be determined by minimising eq. (2.24) are – for each bunch and each DAQ period – a_1, a_2 and a_3 (which are directly related to P, $\mathcal{L}_c$, $\mathcal{L}_{bg}$). In order to reach this goal we search for the maximum likelihood. In eq. (2.24) N_h and S are taken from the experimental energy histogram and the variations of W with a_k are all contained in $\Psi(E_h)$ and M.

The maximum of W corresponds to the following set of partial differential equations (obtained by differentiating eq. (2.24):

$$W'(a_k) = \frac{\partial W}{\partial a_k} = 2S\frac{\partial M}{\partial a_k} - 2\sum_{h=1}^{H} N_h \frac{1}{\Psi'}\frac{\partial \Psi'}{\partial a_k} = 0\,. \tag{2.25}$$

In order to solve this system we use a classical iterative scheme similar to a χ^2 minimisation procedure. We define

$$\hat{W}_{ij} = \frac{1}{2}\frac{\partial^2 W}{\partial a_k \partial a_j} = \sum_{h=1}^{H} N_h \frac{1}{(\Psi')^2}\frac{\partial \Psi'}{\partial a_k}\frac{\partial \Psi'}{\partial a_j} - \sum_{h=1}^{H} N_h \frac{1}{\Psi'}\frac{\partial^2 \Psi'}{\partial a_k \partial a_j} \tag{2.26}$$

and we write a_k some initial values of the unknown parameters. We then search for a set of parameters $a_k + \delta a_k$ such that all the derivatives vanish. Writing a first order expansion for $W'(a_k)$

$$W'(a_k + \delta a_k) = W'(a_k) + \hat{W}_{ij}\delta a_j \tag{2.27}$$

we obtain

$$\delta a_k = -\sum_{i=1}^{3} \hat{W}_{ki}^{-1} \times W'(a_j)\,. \tag{2.28}$$

and we iterate until the solution is reached.

Finally the uncertainty on the determination of a_k is as usual given by:

$$\Delta a_k = \hat{W}_{kk}^{-1/2} \tag{2.29}$$

Note: in the single-photon mode Ψ' being a linear function of the unknown a_k, the second term of eq. (2.26) disappears and $\hat{W}$ is positive definite.

Estimator #2: the average energy

This estimator makes sense for the multi-photon mode, i.e. in the limit $M \to \infty$ where the energy distribution becomes Gaussian. However, even outside this limit the average energy can always be taken as an estimator to measure the polarisation. In this section we derive the expressions of the average and of the width of the energy distribution.

Let us define the average energy of a photon entering the calorimeter (here again we drop the experiment index):

$$\mathcal{E} = M^{-1} \int_0^\infty \frac{dm(E)}{dE} E dE$$

and its variance

$$(\Delta\mathcal{E})^2 = M^{-1} \int_0^\infty \frac{dm(E)}{dE} E^2 dE - \mathcal{E}^2.$$

For N photons entering the calorimeter after a bunch-crossing, the average energy is given by

$$< E >_N = N\mathcal{E}$$

with $E = \sum_{i=1}^N E_i$. Defining $E^2 = \sum_{i=1}^N \sum_{j=1}^N E_i E_j$, one gets

$$< E^2 >_N = N(\Delta\mathcal{E})^2 + N^2\mathcal{E}^2.$$

Finally, introducing the Poissonian law to describe the probability that N photons are produced one obtains:

$$< E >= \sum_0^\infty e^{-M} \frac{M^N}{N!} < E >_N = M\mathcal{E}.$$

Notice that one could have also derived this expression more directly since

$$< E >= \int_0^\infty \frac{d\mathcal{P}(E)}{dE} E dE = M\mathcal{E}\,.$$

For the variance, writing

$$< E^2 >= \sum_0^\infty e^{-M} \frac{M^N}{N!} < E^2 >_N = M(\Delta\mathcal{E})^2 + M(M+1)\mathcal{E}^2$$

we get

$$(\Delta E)^2 = M(\Delta\mathcal{E})^2 + M\mathcal{E}^2$$

where one should remark the presence of the often forgotten extra term $M\mathcal{E}^2$.

To build an estimator from the measured average energy we shall consider the limit $M \to \infty$. In this limit the energy distribution is Gaussian:

$$\frac{d\mathcal{P}(E)}{dE} = \frac{\exp -\frac{(E - M\mathcal{E})^2}{2(\Delta E)^2}}{\sqrt{2\pi}\Delta E}\,,$$

and the Likelihood function is then given by:

$$W \equiv -2\ln L = \sum_{e=1}^{3} \sum_{h=1}^{H} \frac{(E_h^e - M^e\mathcal{E}^e)^2}{(\Delta E^e)^2} + \ln[(\Delta E^e)^2]\,, \tag{2.30}$$

where the factors containing π have been removed and where E_h^e is the energy measured in the bin h. To simplify eq. (2.30) we use

$$\sum_{h=1}^{H} \frac{(E_h^e - M^e\mathcal{E}^e)^2}{(\Delta E^e)^2} = \frac{1}{(\Delta E^e)^2}\left(H(M^e\mathcal{E}^e)^2 + \sum_{h=1}^{H}(E_h^e)^2 - 2M^e\mathcal{E}^e \sum_{h=1}^{H} E_h^e \right),$$

so that introducing the average and the variance of the measured energy distribution

$$E_m^e = \frac{1}{H}\sum_{h=1}^{H} E_h^e \ , \ (\Delta E_m^e)^2 = \frac{1}{H}\sum_{h=1}^{H}(E_h^e)^2 - H(E_m^e)^2 \ ,$$

one finds the following expression for the estimator

$$\boxed{W = \sum_{e=1}^{3} H^e \left\{ \frac{(E_m^e - M^e\mathcal{E}^e)^2 + (\Delta E_m^e)^2}{(\Delta E^e)^2} + \ln[(\Delta E^e)^2) \right\}.} \tag{2.31}$$

The unknown parameters a_k are finally determined by minimising eq. (2.31).

Estimator #3: χ^2 for the average energy

By assuming that, in the previous estimator, $(\Delta E_m)^2$ is a good estimator of $(\Delta E)^2$ one may transform the likelihood estimator into a χ^2 estimator:

$$\boxed{\chi^2 = \sum_{e=1}^{3} H^e \frac{(E_m^e - M^e\mathcal{E}^e)^2}{(\Delta E_m^e)^2}}. \tag{2.32}$$

This estimator is just a simplified version of the previous one and is usually used experimentally.

Estimator #4: Asymmetry

For a given bin h of the energy distribution, the energy asymmetry is defined by

$$A_h^m = \frac{N_h^2 - N_h^3}{N_h^2 + N_h^3 - 2N_h^1} \ ,$$

where the upper-scripts refer to the experiment number. In the single-photon mode this quantity is described by $P \times A_h^T$ with $A_h^T = f_3(E_h)/f_2(E_h)$ (see section 2). Because A_h^m is directly proportional to P, one usually takes it as *the* LPOL estimator. However, this is only true for the single-photon mode since the relation between A_h^m and P is no longer linear in the few-photon mode. In the latter case it is of course possible to describe consistently A_h^m but then the relation becomes complicated because the denominator also depends on P. Therefore we shall define an estimator using the energy asymmetry only for the single-photon mode. A straightforward estimator is then

$$\chi^2 = \sum_{h=1}^{H} \frac{(A_h^m - P \times A_h^T)^2}{(\Delta A_h^m)^2}$$

where ΔA_h^m is the experimental uncertainty of the measurement of A_h^m. From the condition $\partial\chi^2/\partial P = 0$ we obtain:

$$\boxed{P = \frac{\sum_{h=1}^{H} \frac{A_h^m A_h^T}{(\Delta A_h^m)^2}}{\sum_{h=1}^{H} \frac{(A_h^T)^2}{(\Delta A_h^m)^2}}\,.} \tag{2.33}$$

Bibliography

[1] J. Buon, in *Advances of accelerator Physics and Technologies*, World Scientific, 1993; LAL report 92-28/1992.

[2] B.W. Montague, Phys. Rep. 113 (1984)1.

[3] D.P. Barber, 15th Advanced Beam Dynamics Workshop, Monterey, U.S.A. 1998; DESY report 98-096/1998.

[4] D.P. Barber and G. Ripken, in the Handbook of Accelerator Physics and Engineering, Eds. A.W. Chao and M. Tigner, World Scientific, 2002.

[5] G.Z.M. Berglund, *Spin-orbit maps and electron spin dynamics for the luminosity upgrade project at HERA*, Ph.D. Thesis, DESY-THESIS-2001-044.

[6] C. Cohen-Tannoudji, D. Diu and F. Laloe, *MECANIQUE QUANTIQUE, Tome I* (Hermann, Paris 1977).

[7] R.C. King, *A precise measurement of the left-right asymmetry of Z boson production at the SLAC linear collider*, Ph.D. Thesis, SlAC-452, 1994.

[8] A.A. Sokolov and I.M. Ternov, "Synchrotron radiation", Akademie-Verlag, Berlin 1968.

[9] J. Buon and K. Steffen, Nucl. Instr. and Meth. A245 (1986) 248.

[10] D.P. Barber et al., Nucl. Instr. and Meth., A329 (1993) 79.

[11] See D.P. Barber et al., Nucl. Instr. and Meth., A338 (1994) 166 and references therein.

[12] M. Beckmann, Nucl. Instr. Meth., A479 (2002) 334.

[13] V. Andreev et al., DESY-PRC 98-07; for an update of the Polarization 2000 project see `http://pia.desy.de:9999/TWDM/fcgi/twdmdoc`.

[14] E. Barrelet et al., DESY PRC 00-02.

[15] R. Bacher et al. *The HERA luminosity upgrade*, document available on `http://www.desy.de`.

[16] B. Wagner et al., Nucl. Instrum. Meth. A294 (1990) 541.

[17] M. Born and E. Wolf, *Principle of Optics*, third eds. Pergamon press, Oxford, England, 1965.

[18] S. Huard, *Polarisation de la lumière* (Masson, Paris, 1993).

[19] J.D. Jackson, *Classical electrodynamics*, third eds. John Wiley and sons, New-York 1999.

[20] P. Yeh, *Optical waves in layered media* (Wiley, New-York, 1988).

[21] R. C. Jones, J. Opt. Som. Am. 37 (1947) 107.

[22] E. Collett, *Polarized light: Fondamentals and applications* (Marcel Decker Inc., 1993).

[23] R.M.A. Azzam and N.M. Bashara, *Ellipsometry and polarized light*, Amsterdam, Noth-Holland, 1977.

[24] U. Fano, J. Opt. Soc. Am., 39 (1949) 859.

[25] G. Araki, Prog. Theo. Phys., 1 (1946)125; Phys. rev., 74 (1948) 472.

[26] R.J. Glauber, Phys. Rev. 130 (1963) 2529; Phys. Rev. 131 (1963) 2766.

[27] G. Bardin et al., *Conceptual design report of a Compton polarimeter for Cebaf Hall A*. Document vailable on `http://www.cebaf.gov/Compton`.

[28] N. Falleto, *Etude, conception et réalisation d'une cavité Fabry-Perot pour le polarimètre Compton de TJNAF*, Ph.D. Thesis, Université J. Fourier Grenoble 1, 1999.

[29] M. Placidi and R. Rossmanith, Nucl. Instr. and Meth. A274 (1989) 79.

[30] L. Knudsen et al., Phys. Lett. B270 (1991) 97.

[31] L. Arnaudon et al., Phys. Lett. B284 (1992) 431.

[32] K. Piotrzkowski, hep-ex/9504003.

[33] Y.S. Tsai, Rev. Mod. Phys. 46 (1974)815.

[34] M. Lomperski, DESY 93-045.

[35] HERMES Collaboration; W. Lorenzon et al., *A proposal to DESY for a longitudinal Electron Polarimeter at HERA-EAST Section*, (1995).

[36] G. Grindhammer in *Proceedings of the workshop on calorimetry for supercolliders*, Tuscaloosa, 1989. G. Grindhammer, privite communication.

Chapter 3

A Fabry-Perot Cavity for an upgrade of the HERA longitudinal polarimeter

In chap. 1, it has been shown that a fast and precise polarimeter is necessary to reach a high precision on the physics results produced after the HERA upgrade. In chap. 2, we have shown that a solution for a high accuracy Compton polarimetry is the use of a high power continuous laser.

In this chapter, we describe the experimental solution leading to a high Compton scattering rate, namely the Fabry-Perot[1] optical resonator.

3.1 A Fabry-Perot cavity for polarimetry

The formal aspects of optical resonators are the subjects of numerous monographes and articles. In order not to repeat what has already been described elsewhere I refer to refs. [2, 3]. Only the main features concerning laser Gaussian beams and cavity modes are summarised in appendix 3.6.

Details on the use of a Fabry-Perot cavity for polarimetry are given in the very complete ref. [4] (see also [5]) and in CEA-Saclay technical notes [6].

3.1.1 Principle of Fabry-Perot cavities

In its simplest version, a Fabry-Perot cavity consists in two spherical mirrors located opposite to each other. When an incident plane wave arrives in the cavity in phase with the plane waves circulating inside the cavity, the interference is constructive and the power inside the cavity increases. This is a resonance phenomena and since the phase shift of a plane wave after a round trip between two mirrors is $k \times 2L$, with L the distance between the two mirrors and k the wave vector, the resonance condition simply reads

$$\lambda = \frac{2L}{q} \Longleftrightarrow \nu = q\frac{c}{2L} \tag{3.1}$$

[1] According to the French administration, there is no accent on the letter e of Perot [1].

for $q \in \mathbb{N}^*$ and where $\lambda = 2\pi/k$ and $\nu = kc/2\pi$ are the laser wavelength and frequency respectively.

In practice one has to deal with laser beams which are not plane waves but usually almost Gaussian beams. Fortunately, the eigen-modes of a spherical resonator are also not plane waves. They are determined by the solutions of the paraxial Maxwell equations with the proper boundary conditions. The fundamental mode of these solutions is Gaussian so that, in order for a Gaussian laser beam to propagate inside a cavity, one must add to the frequency matching condition of eq. 3.1 the spatial mode matching conditions (i.e. one must match the cavity/laser waist in size and position).

If the laser beam axis of propagation coincides with the cavity optical axis (see appendix 3.7) and if the laser beam is perfectly Gaussian and mode matched, then there exists only one resonance frequency (modulo 2π) and the full power of the laser beam is efficient. If the mode matching is not perfect (laser beam ellipticity for example) or/and if the laser/cavity alignment is not perfect, then the cylindrical symmetry is broken and, depending on the new geometrical configuration, higher order modes can propagate (see appendix 3.6). The resonance frequencies for these excited modes are all different for stable cavities so that the net effect of such faults is a loss of power in the fundamental mode of the cavity.

Applying the continuity conditions for the electromagnetic field on the cavity mirrors one gets the expression of the field inside the cavity and therefore the corresponding power:

$$P_{in} = P_0 \times G\,,\ G = \frac{T}{(1-R)^2} \times \frac{1}{1 + \frac{4R}{(1-R)^2}\sin^2\frac{2\pi\Delta\nu L}{c}}\,,$$

where P_0 is the incident power, G is the cavity gain, $\Delta\nu$ is the difference between the laser and cavity resonance frequencies, R and T are the reflection and transmission coefficients (for intensity) of the mirror coatings (see appendix 3.7.1). G is shown in fig. 3.1 for a 2 m long cavity with R and T given in table 3.2 of appendix 3.7.1.

From this figure and from the above expression, one defines the following useful quantities:

- the Free Spectral Range $FSR = c/(2L)$ (frequency distance between two longitudinal modes of the cavity);
- the Full Width at Half Maximum $FWHM$ (width of the resonance peak).
- the Finesse $F = FSR/FWHM \approx \pi\sqrt{R}/(1-R)$ (the number of round trips of a plane wave inside the cavity is thus given by F/π [2]);
- the characteristic time or filling time of the cavity. For a high finesse, it reads as [4]

$$\tau \approx \frac{LF}{\pi c}.$$

For a 2 m long cavity and for a Nd:YAG laser ($\lambda = 1064$ nm) one gets

$$\frac{FWHM}{\nu} \approx 10^{-11}$$

[2] This the number of round trip of a plane wave until the intensity vanishes. This is simply obtained using $\sum_0^\infty r^n = 1/(1-r)$ with $r = \sqrt{R}$ the amplitude reflection coefficient.

with the above formula and using the numbers given in table 3.2 of appendix 3.7.1. One also gets the following cavity filling time $\tau \approx 60\mu$s.

In other words, if one wants to keep such a cavity at the resonance, one must match the cavity length and the laser beam frequency at 10^{-11} level. Clearly, a fast feedback system is required in order to ensure this condition.

A feedback loop can act on the cavity length (piezo-electric transducer moving the mirrors) or on the laser beam frequency (frequency continuously tunable laser). For practical reasons, explained in the next section, we have chosen the second solution.

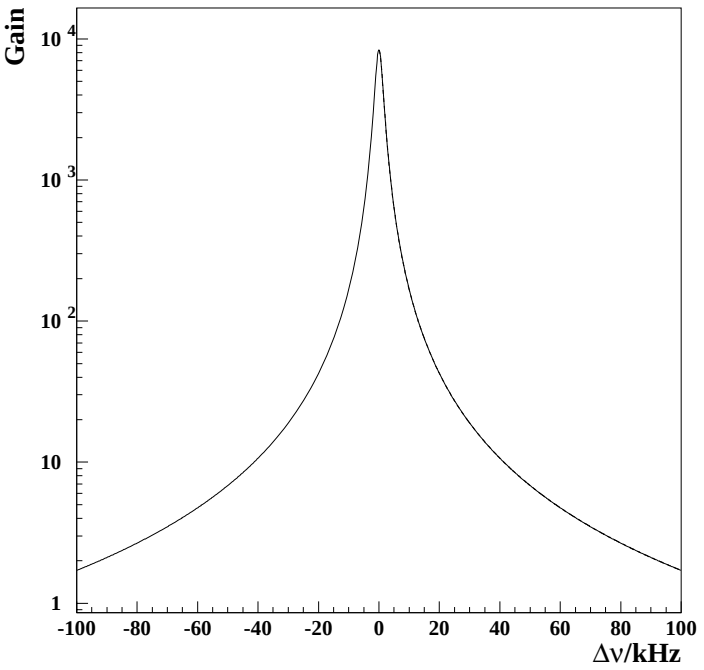

Figure 3.1: *Gain of a 2 m long cavity as a function of the difference between the laser and cavity resonance frequencies. Values of the cavity mirror reflection and transmission coefficients are those given in appendix 3.7.1.*

3.1.2 Choice of the cavity geometry for HERA

The principle of the implementation of a cavity around an electron beam pipe is described in fig. 3.2. The cavity mirrors are introduced inside the cavity, near the electron beam pipe and the laser and all the other optical components are located on the optical table close to the cavity. Since the mirrors are located inside an ultra high vacuum region ($\approx 10^{-9}$ Tor), it is not convenient to use actuators for the feedback. The solution of a monolithic cavity has therefore been chosen. This experimental set-up has been operated successfully at Jefferson Laboratory on the CEBAF accelerator [4, 7, 8] and we have taken advantage of the experience accumulated there.

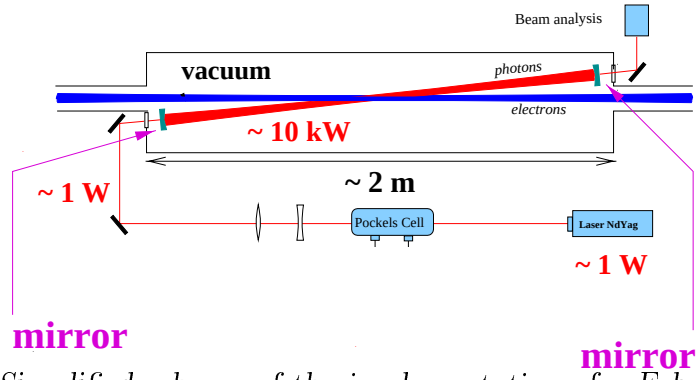

Figure 3.2: *Simplified scheme of the implementation of a Fabry-Perot cavity inside the electron beam pipe. The optical elements and the laser are located close to the beam pipe. From [4].*

The exact layout of the cavity is determined by the total distance between the two mirrors, the radius of curvature of the mirrors and the crossing angle between the laser beam and the lepton beams. This angle is given by $\alpha \approx 2d + \Phi/L$, where L is the cavity length, d is the distance between the electron beam axis and the edge of the mirror and Φ is the mirror diameter. To avoid synchrotron radiation, the laser beam must cross the electron beam in the vertical plane, i.e. along the y axis (see fig. 2.1 of chap. 2). The minimum value for d is then fixed by the machine requirements, that is 2 cm. One must also add 2.5 cm for mechanical purposes. The cavity waist (see appendix 3.6.1 for a definition), i.e the laser beam waist, depends on the mirror radius of curvature R_c. In section 3.7.2 we show that, for confocal cavities $R_c = L$, the mechanical stability is optimum. Considering a confocal cavity with $d = 4.5$ cm and $\Phi = 25.6$ mm and using eq. 2.4 of chap. 2 for the laser beam/electron beam luminosity, one can determine the Compton event rate as a function of the remaining free parameters, the cavity length and the light power inside the cavity. This rate is shown in fig. 3.3 for a 1 mA electron beam intensity and various values of the light power inside the cavity. The grey hatched area corresponds to the scattered photon rate of 1 to 2 photons per interaction for an electron current of 40 mA (typical value for the HERA running). In chap. 2 we have shown that with this event rate the polarisation measurement accuracy is much below 1 per mille per bunch and per minute. Therefore, from this figure it can be seen that a 2 m long cavity intersecting the lepton beam at 3.3 degrees (58 mrad) will deliver the needed luminosity provided a laser beam power of the order of a few kW is supplied, that is 3 kW to fix a number.

In summary, a 2 m long confocal cavity has been chosen for HERA on the basis of mechanical and luminosity constrains. This is twice longer than the CEBAF cavity.

3.2 Mechanical design of the cavity

3.2.1 Constraints

One of the main considerations when designing the cavity is that wake fields from the passing electron beam should not disturb the cavity operation, and that the cavity should

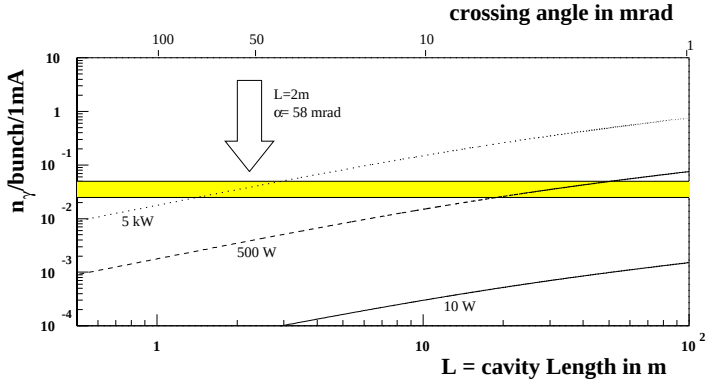

Figure 3.3: *Event rate per bunch normalised to a total electron current of 1 mA as a function of the cavity length (bottom scale) and the crossing angle (top scale). For the plot it is assumed that the separation between the beam axis and the mirror centre is kept constant at 5.75 cm.*

not perturb the electron beam. The mutual perturbation is minimised by the introduction of a 15 mm diameter tube, which is used to suppress the propagation into the cavity of high frequency modes from the passing beam. Numerical calculations indicate that this tube should extend ±80 cm from either side of the hole in the beam pipe (see figs. 3.4 and3.5). By making the hole for the laser beam in the beam pipe as small as possible the power loss through electromagnetic heating is also reduced to an almost negligible level (18 W during injection, less than 0.1 W during normal beam operation [9]).

Another constraint comes from the presence of the small tube around the laser beam inside the cavity. The laser beam must pass 'far away' from the tube surface in order not to loose intensity by diffraction. In appendix 3.7, the determination of the mechanical tolerances is described. The laser beam tube size defines in fact the maximum tolerable angular and axial relative misalignment between the two cavity mirrors. For 15 mm diameter, it is safe to require angular and position tolerances of 1 mrad and 1 mm. Under these conditions, the cavity optical axis crosses the mirrors within 3 mm, at most, from their centres. Of course, once the mirrors are mechanically aligned, one has to align and mode match the laser. But with these tight tolerances, we ensure that losses induced by diffraction are negligible.

Another constraint comes from the laser itself. Once turned on, one should not change its frequency by more than ≈ 70 GHz. Above this threshold, the longitudinal mode of the laser changes and this may induce some perturbation on the feedback operations. This frequency threshold induces a constraint on the maximum variation of the distance between the two mirrors. This distance must not exceed 70 μm once the cavity has been locked.

3.2.2 Mechanical design

From the constraints given above, the cavity must consist in a cylindrical vacuum vessel surrounding a beam pipe section on which two small tubes are soldered. The mirrors also have to lay in the vacuum and therefore inside the vessel but, because of heat effects

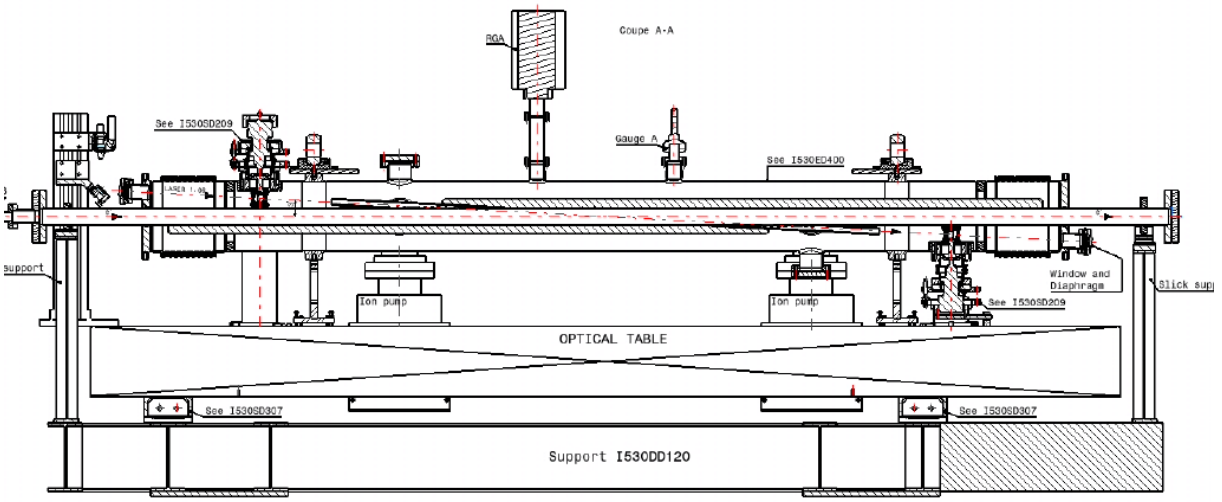

Figure 3.4: *Technical drawing (longitudinal view) of the cavity. See text for comments. From [10].*

Figure 3.5: *Picture of beam pipe inside the cavity (half is shown). Above the elliptic electron beam-pipe, a circular tube is soldered to reduce the wakefield excitations.*

and possible vibrations propagating along the beam pipe, they cannot be mounted rigidly on the vessel. The solution adopted is to mount the mirrors in a post holder fixed to a plate resting on two big cylindrical legs clipped on the optical table (see table 3.10). The post holders are linked to the vessel through metal bellows thus filtering the remaining vibrations. In this way, the cavity mirrors are completely part of the optic table which supports all the optics.

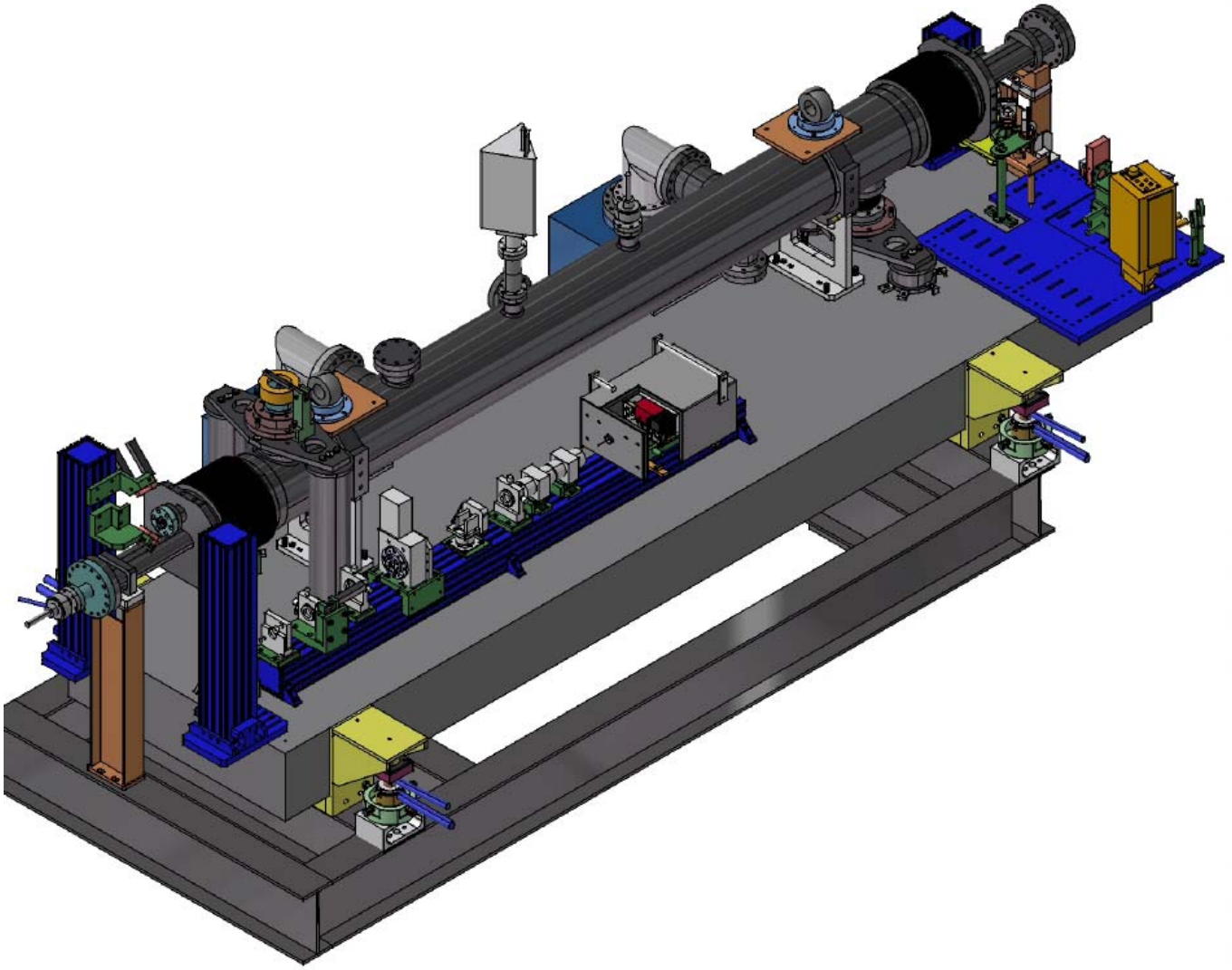

Figure 3.6: *Three dimension technical drawing of the cavity and of the optical scheme. See text for comments. From [10].*

The mechanical scheme is shown in figs. 3.4 and 3.6 and a picture taken during the installation is given in fig. 3.7. All components are made of stainless-steel. To reduce the vibrations coming from the beam pipe, the beam pipe inside the cavity is isolated from the rest of the HERA beam pipe by two standard HERA bellows (not visible on figs 3.4 and 3.6). The cavity vessel is isolated from the beam pipe inside the cavity by two other bellows. The vessel is finally mounted on the table via two pairs of passive absorbers (see

Figure 3.7: *Picture of the cavity taken during the installation. The laser and the optical elements before the cavity entrance are located on the rail parallel to the cavity vessel. The red laser diode, used to aligned the cavity mirrors, enters the cavity by the opposite entrance. It is visible on the picture: between the rail and the cavity vessel and mounted on a post holder at a height higher than the rail.*

fig. 3.8). The optical table is therefore isolated from the beam pipe by a three stage filter: two pairs of bellows and two pairs of absorbers.

The inner part of the cavity is shown in fig. 3.5 (see also fig. 3.4). To increase the gas conductance between the beam pipe and the vessel, holes have been implemented during the soldering of the laser beam tubes. To reduce heat effects induced by synchrotron radiations, the size of the beam pipe inside the cavity has been increased. The tubes are supported by rectangular plates, they have been assembled with respect to the tolerances given in the above section.

The cavity vacuum windows are 3 mm thick and 30 mm diameter silica plates. To avoid birefringence, the windows have been anti-reflection coated and soldered to the stainless steel flanges according to a special procedure (glass-metal soldering). Since the laser beam inclination is 58 mrad with respect to the electron beam, the vacuum windows have been also inclined by 58 mrad.

The optical table must be kept in the machine plane ('HERA is tilted' by 8 mrad and 3 mrad around the horizontal axes x and z respectively, see fig. 2.1 for the axes) and isolated from ground vibrations. Because of large temperature variations inside the HERA tunnel (more than 10 K between open and running conditions), active isolators would have induced movements of the table, therefore only passive absorbers could be used to isolate the table from the ground. A special mechanical interface has been designed to align the table/cavity onto the HERA plane.

Inside the cavity, the vacuum is maintained by two ion pumps visible on fig. 3.6 and pressure is measured by a vacuum gauge (on the top of the cavity vessel, see fig. 3.4). The heavy ion pumps are isolated from the optical table by passive absorbers (see fig. 3.9).

The mirror mounts are shown in fig. 3.10. It is important to be able to align the two mirrors within the accuracies given in the above section. To do so, the rotation around the normal of the optical table is done using a lockable air-vacuum rotator. The orientations of the mirrors in the other directions are performed using a standard optical technique (named 'gimbal mount'): the mirror is attached to a plate which is moved via three micrometric screws acting on a plane, a line and a point. With this technique, the mirror centre stays at the same height during the alignment operations.

The cavity mirrors are aligned with respect to each other using the auto collimation technique and a red laser diode (see chap. 5 for details). The laser diode – visible on fig. 3.6 – is injected inside the cavity by two mirrors (see fig. 3.11) rigidly mounted on a movable rail.

3.2.3 Implementation at HERA

To control the thermal expansions of the cavity and of the optical table, the whole system is surrounded by an isotherm house (see the picture of fig. 3.13). Inside this house, the temperature is controlled and kept constant within $\pm 1^o$. This is enough with regard to the laser longitudinal modes since all mechanical components, including the optical table, are made of stainless-steel[3] (thermal dilatation = 36 μm per degree).

Another purpose of the cavity housing is the radiation protection. The optical elements located on the optic table are made of glass, quartz, calcite, KD*P, TGG and YAG doped

[3]Only the plates on which the cavity mirror post holders are mounted are in Aluminium.

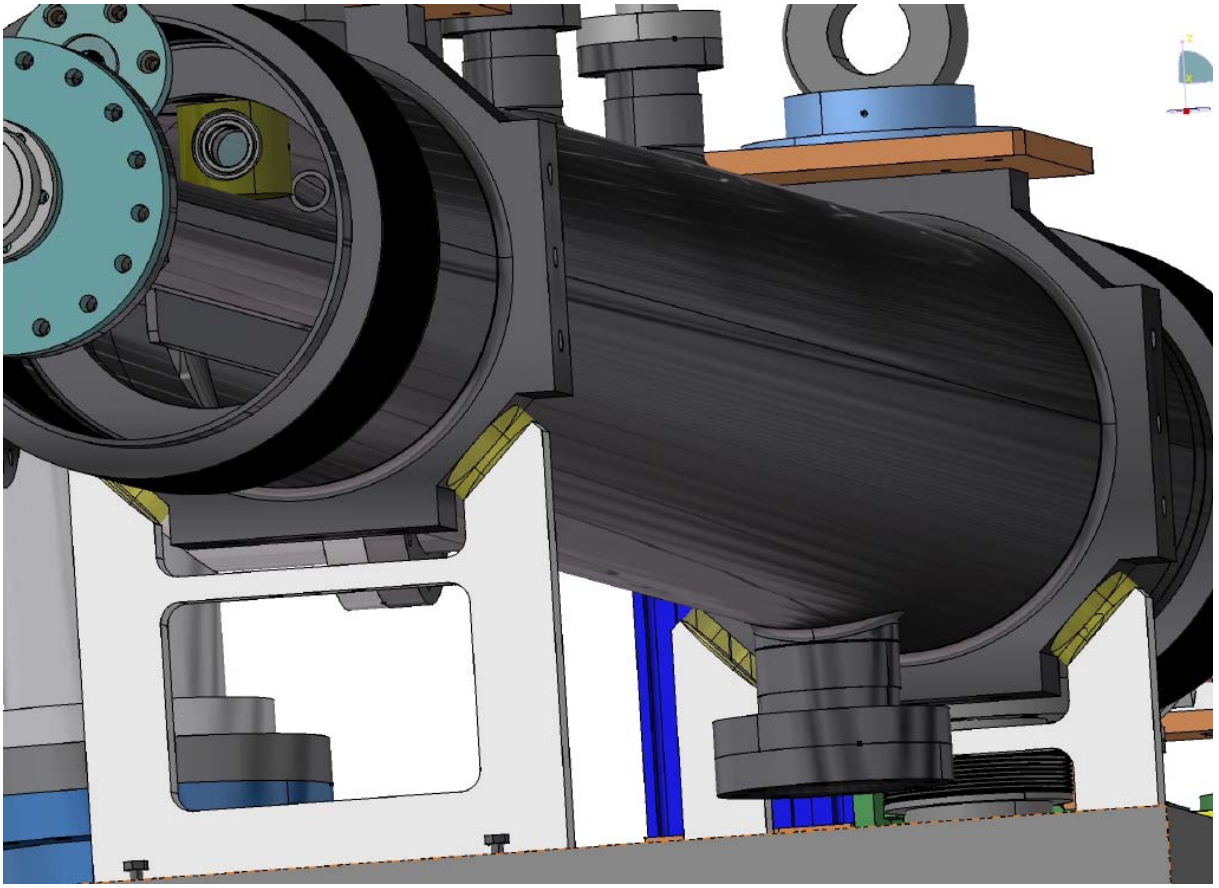

Figure 3.8: *Technical drawing of cavity vessel mount. From [10].*

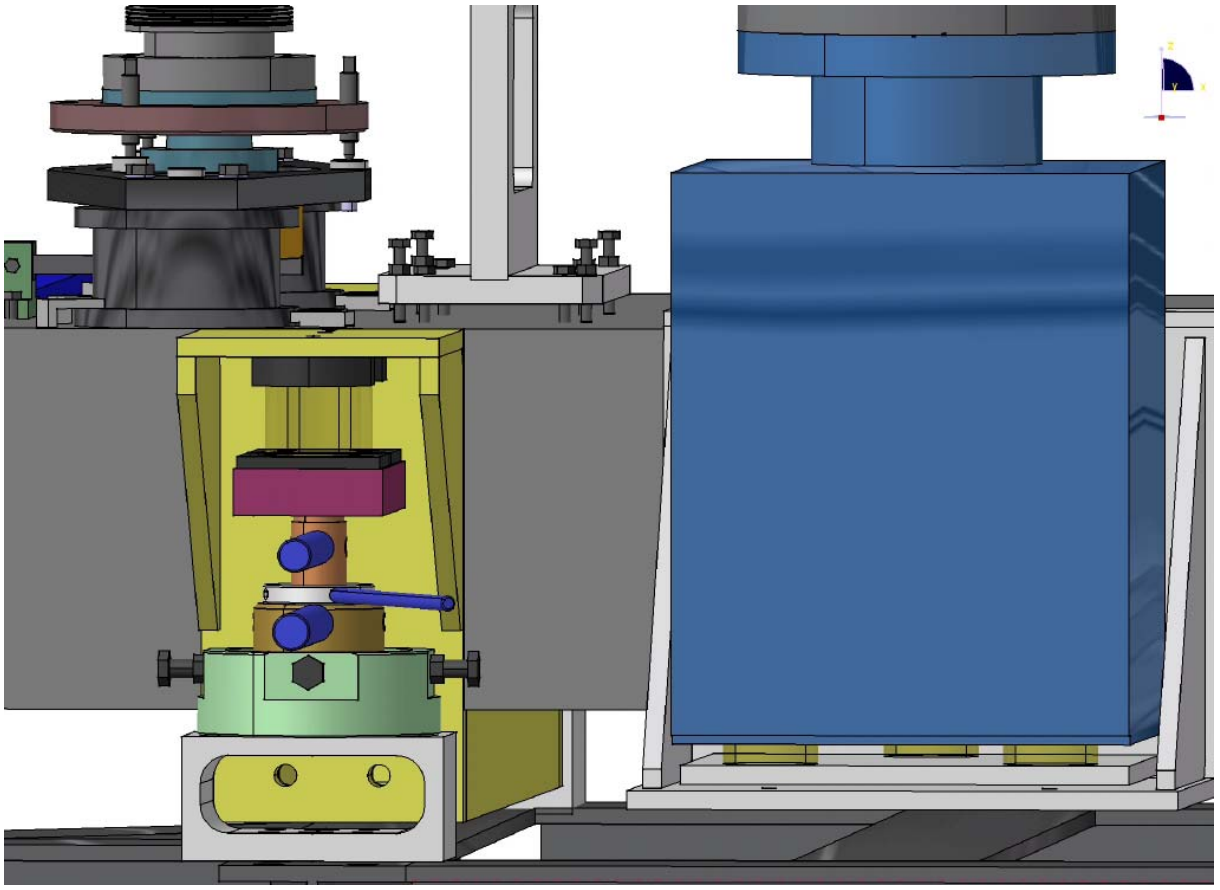

Figure 3.9: *Technical drawing of the ion pump (blue cube on the right of the figure) and of the optical table mount. From [10].*

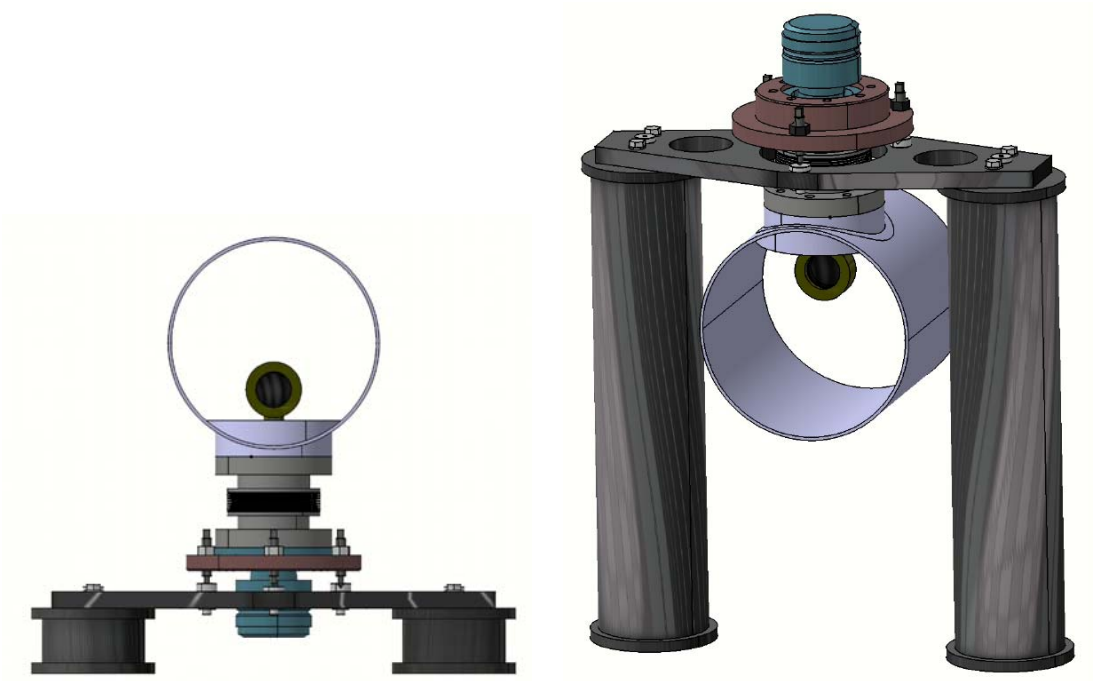

Figure 3.10: *Technical drawing of the cavity mirror mounts (lower and upper mirrors on the left and right sketches respectively). The cylinder around the mirror is the cavity vessel. The belows, used to isolate the mirror mount from the cavity vessel is visible on the left sketch (below the vessel). From [10].*

crystal. They are all sensitive to deep UV, X-rays and gamma-rays. For example, natural quartz (SiO_2 crystalline) always contain a small amount of crystal site defaults: Al, Na, Li atoms and OH^- molecules [11, 12]. These defaults do not modify noticeably the optical properties of quartz except when it has been irradiated. In this case the quartz is solarised: contaminating atoms are ionised and this leads to absorption of light in the near infrared and visible domain [13].

To avoid radiations, a 3 mm lead shielding is located all around the cavity house. During the summer 2000, we have let a couple of cavity mirrors (junk items) directly on the beam pipe at the future cavity location and we observed no alteration of their optical properties.

3.3 Optical scheme

One needs to provide a set of optical elements in order to inject adequately the laser beam inside the cavity and to control the light polarisation. In this section a brief description of these optical elements is given.

We start by a description of the laser, focusing on the informations necessary to understand our experimental results described in chap. 5. Next all optical elements used in our set-up are described. This section is closed by a discussion on the expected level of parasitic birefringence induced in our set-up.

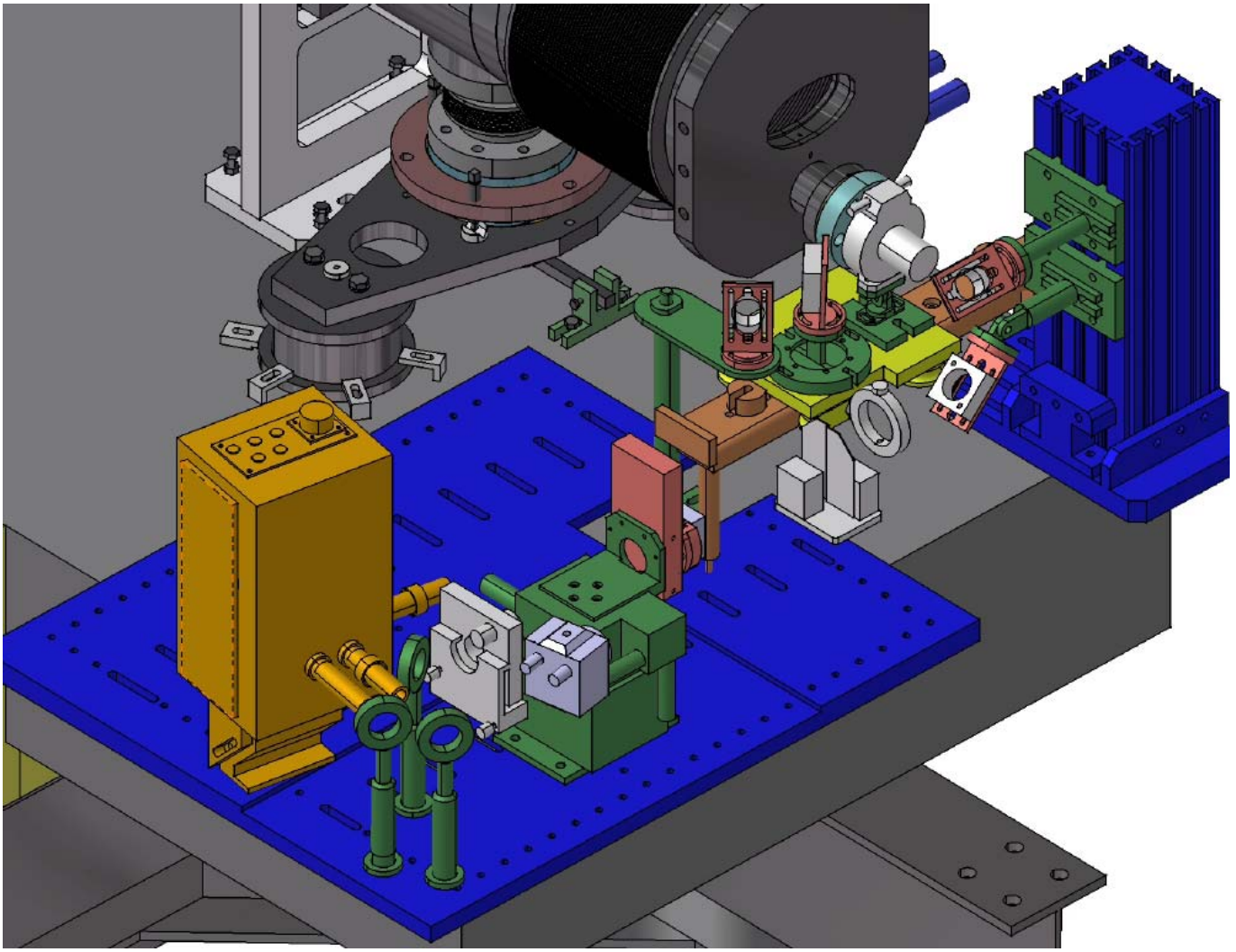

Figure 3.11: *Technical drawing of the ellipsometer. Also visible are the two mirrors used for the cavity mirror alignment. These mirrors, mounted on a rigid rail located* ≈ 24.7 *cm above the table, are used to inject the red laser diode inside the cavity. The Glan-Thomson prism, also mounted on this rail, used for birefringence calibrations is also shown in this picture. For sake of clarity, the electron beam pipe has been removed from the drawing. From [10].*

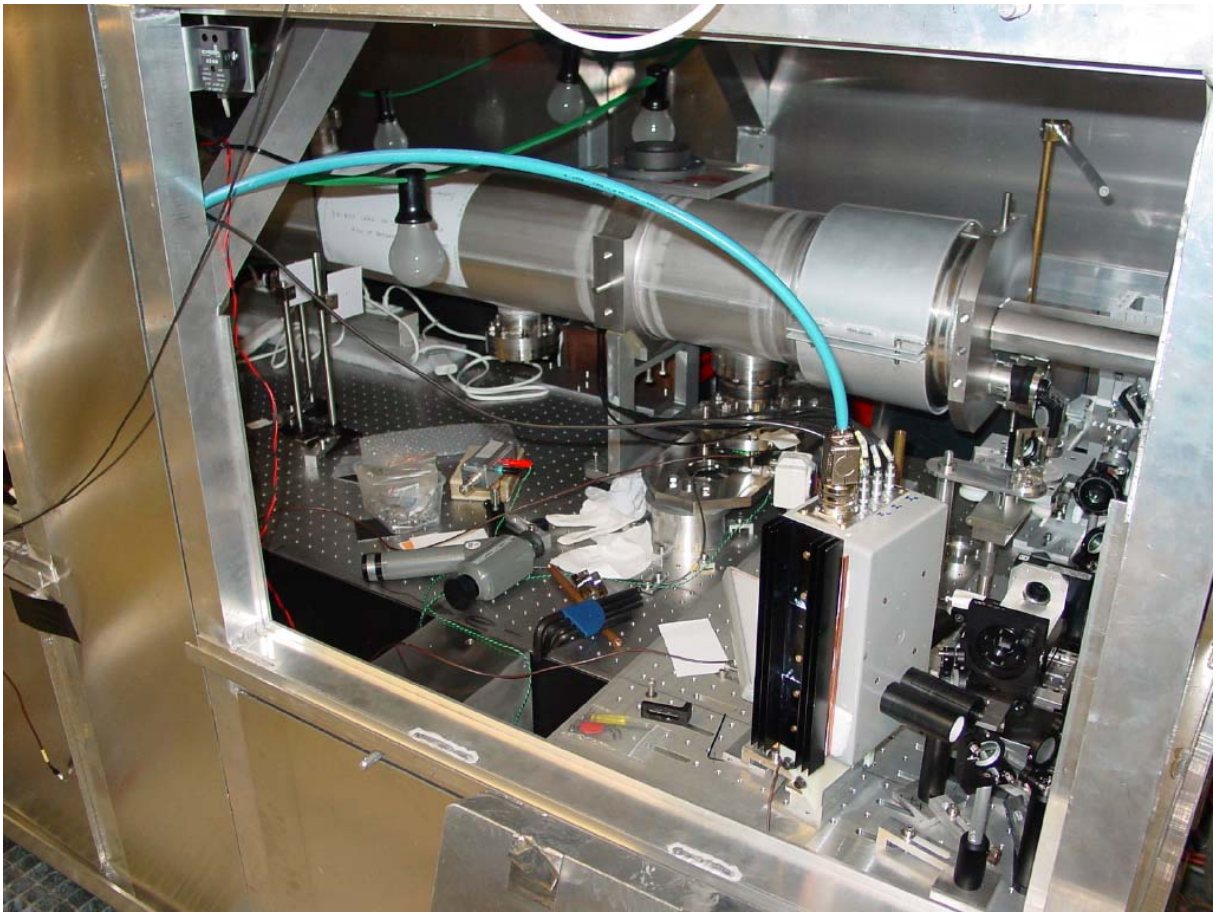

Figure 3.12: *Picture of the cavity output. Visible on this photograph is the cavity housing (thermal isolation plates and aluminium structure), the temperature controlled photodiode box (in front) and the optical elements of the ellipsometer. The lamps were used to heat up the cavity and the optical table.*

Figure 3.13: *Picture of the cavity house. The electronics is located on the top of the cavity house.*

3.3.1 The las

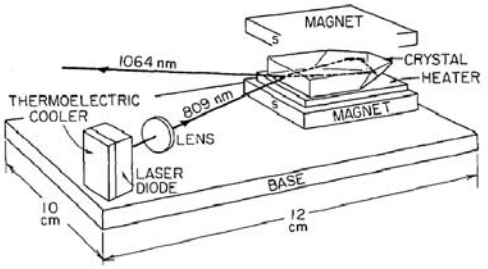

Figure 3.14: *Schematic view of the NPRO laser (see text). From Ref. [15].*

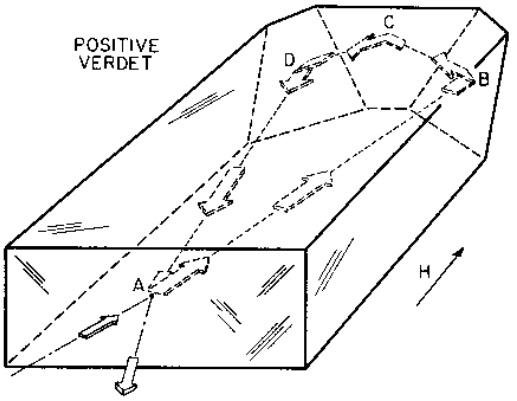

Figure 3.15: *Nd:YAG crystal of a non-planar ring laser (see text for details). The tilts of the light path at points B, C and D fix the polarisation state of the stimulated emitted light .From [14].*

The only laser available from industry, finely tunable in frequency is a non-planar ring Nd:YAG[4] laser (Lightwave[5], model 126). To operate at $\lambda = 1064$ nm, the Nd:YAG rod is pumped by a GaAlAs laser diode cooled in order to emit at 808.5 nm (see fig. 3.14, reasons why a laser is used to pump another laser are given in ref. [16]).

The principle of non-planar-ring oscillator [14, 17] (NPRO) is shown in fig. 3.15. The light emitted by the laser diode enters the rod at point A. The rod surfaces are finely polished and coated in such way that total inner reflection occur at points B, C, and D (at point A the transmission is partial and the surface is curve and coated). The crystal

[4]It is a solid state Neodymium doped Yttrium-Aluminium-Garnet laser.

[5]Recently, the company Innolight has provided a cheaper similar laser. This new laser is, in addition, less noisy and has a smaller linewidth. But it was unfortunately not yet available when we ordered our Lightwave laser ...

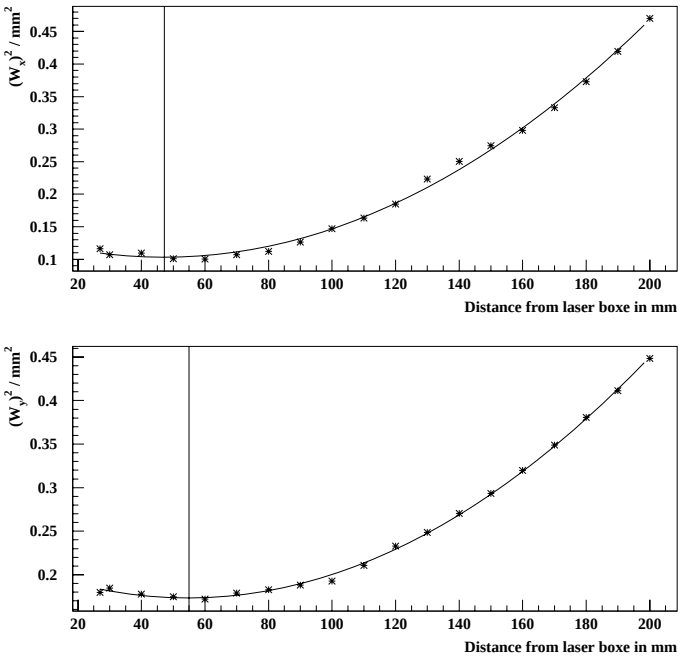

Figure 3.16: *Square of the laser beam radius as a function of the distance from the laser box. Measurement is performed with a beam-scan from Photonics.*

	Given/constructor	measured
Initial Power	760 mW	600-700 mW
Noise amplitude (bandwidth 5 Hz to 10 MHz)	0.019% rms	
Coherence length	>1000 m	
Polarisation	300:1, vertical	
Linewidth	5 kHz over 1 ms	
Frequency jitter	<200 kHz/s	
Frequency drift	<50 MHz/hour	
Thermal tuning range	30 GHz @ 1 GHz/s	
Piezo tuning range	30 MHz @ 4.6 MHz/V (30 kHz bandwidth)	
Waist position	5 cm vertical -	4.7 cm vertical 5.5 cm horizontal
Waist size	0.35 mm vertical 0.46 mm horizontal	0.32 0.42
Beam divergence, full angle	3.9 mrad vertical 3.0 mrad horizontal	

Table 3.1: *Main characteristics of the Lightwave 126-1064-700 laser. We measure the laser beam radius with a beam scan and determine the waist and waist position from a quadratic fit to these measurements.*

is surrounded by a magnetic field H (see fig. 3.14) to match the polarisation state of the resonant mode (garnet is a magneto-optic crystal). The main advantage of such a ring laser, with respect to the standard linear laser cavity, is the reduction of heat inside the crystal (for Nd:YAG laser, heat variation is the main phenomenon broadening the spectral width).

The laser output spatial mode depends strongly on the rod/laser diode alignment [14] and of the entrance surface radius of curvature. We indeed observe a small 'triangular' halo when measuring our beam shape with a CCD camera as shown in ref. [14] (this effect is however very small).

The laser beam is also elliptic as shown by our waist measurements reported in fig. 3.16 (the waist in vertical and horizontal direction are different). An intensity measurement performed at 25 cm from the laser box is shown in fig. 3.17. A characteristic diffractive pattern is clearly visible and, as also shown in this figure, Gaussian fits performed on two projections are very bad. This pattern, depending on the distance between the laser box and the beam-scan device (the intensity shape gets more Gaussian as this distance increases, as expected [3]), induces a bias in the determination of the laser beam waist and therefore on the laser/cavity coupling (the propagation of such beam is more complicated than the one of a pure Gaussian beam). It is difficult to estimate the coupling of such beam to our Fabry-Perot cavity but, in any case, we expect a power reduction inside the cavity.

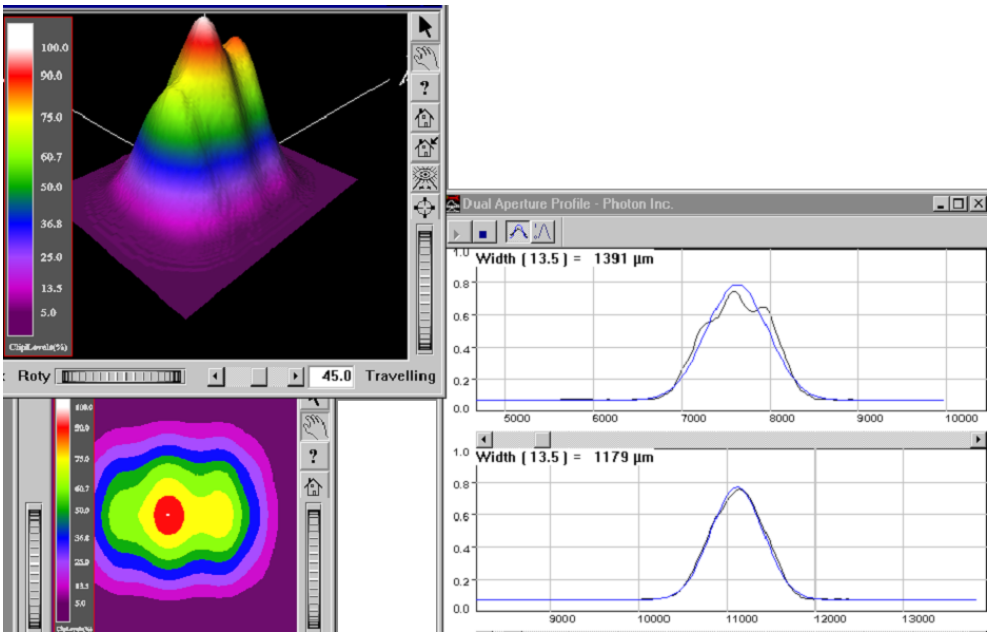

Figure 3.17: *Measurement of the laser beam intensity at 25 cm from the laser box. A 3D view (top left), a 2D contour (bottom left) and two projections (right) are shown. In the latter plot, results of Gaussian fits are also shown.*

There are two ways to modify the laser beam frequency:

- a piezo-electric transducer is located on the rod, thereby modifying the rod geometry and therefore the laser beam frequency (in other words, the transducer changes

the laser cavity length). This is a fast and fine tuning: the laser beam frequency changes by 3.4 MHz for per Volt applied on the actuator (**fast channel**, bandwidth ≈ 30 kHz).

- The rod temperature can be varied thanks to a Peletier module (controlled by a DC voltage). This temperature variation induces a change of the laser beam frequency of 5GHz per Volt applied on the Peletier module. This is a slow frequency variation (**slow channel**, bandwidth ~ 1 Hz).

In fig. 3.18, a schematic picture of the noise intensity is shown. The noise is reduced by feedback control on the laser diode temperature. This laser is a low noise laser and is therefore adequate for our purpose.

The main characteristics of the LightWave laser are given in table 3.1. In chap. 5 we shall advocate the 'large' value of the linewidth to explain why not all the laser beam power could be coupled to the cavity. It is then useful to define the laser linewidth here.

The linewidth is the width of the laser lineshape. The lineshape is defined by the Fourier transform (from time to frequency space) of the electric field autocorrelation function $E^*(t)E(t+\tau)$. The physical origin of a non-vanishing linewidth is related to the random emission phase inside the laser medium. For a solid state laser like the ND:YaG, for example, mechanical strain and temperature variations induce some changes of the optical indices and then of the emission phase [18] (many mechanisms contribute to the lineshape [19], an account for this rich physics topic is obviously beyond the scope of the present work). It can be shown [18] that such phase fluctuations lead to a Lorentzian lineshape. The linewidth thus depends on the mechanical and thermal quality of the laser. Even with a perfect device, the irreducible contribution of the spontaneous emission to the stimulated laser light gives a lower limit on the linewidth (the so called Townes limit [16]). This limit is two orders of magnitudes below the number given by the manufacturer.

The coherence length is a parameter related to the laser linewidth and random emission phase. It can be determined by a Mach-Zehnder like interferometer [24]: if the optical path between the two arms of the interferometer is greater that the coherence length, then no interference pattern is observed. Let us get an idea of the impact of a 1000 m coherence length on the cavity resonance conditions. Taking a finesse around 30000, as the one of our cavity, one gets a number of round trips of $\approx 10^4$, that is a total optical path inside the cavity of 40000 m. Comparing the two numbers one sees that the coherent length is smaller than the optical path (and the laser linewidth greater than the cavity FWHM which is around 3 kHz, though it is given at a different time scale) so that we may not be able to 'fill the cavity completely'.

3.3.2 Details of the optical scheme

One needs to provide a set of optical elements to fulfil the following functions:

- creation of a circular polarisation laser beam and switching between left and right polarisation;
- laser/cavity mode matching;
- laser/cavity geometrical alignment;

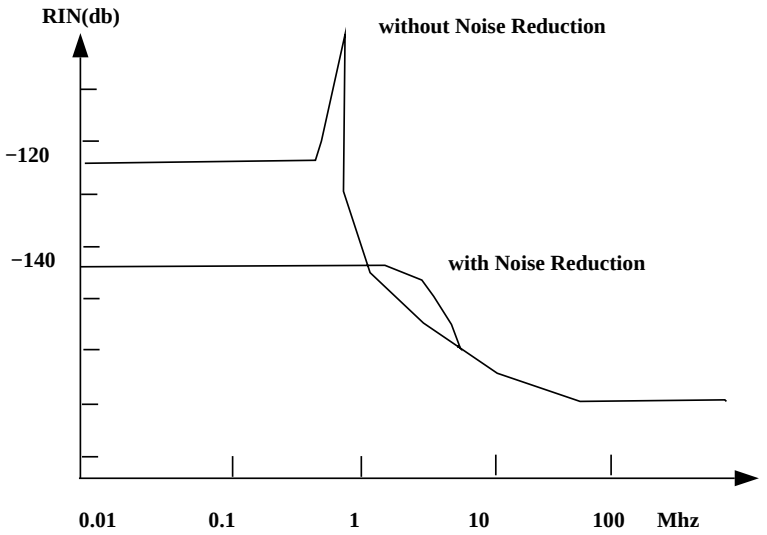

Figure 3.18: *Approximate distribution of the residual noise intensity (as a function of the laser beam frequency variation). From [7].*

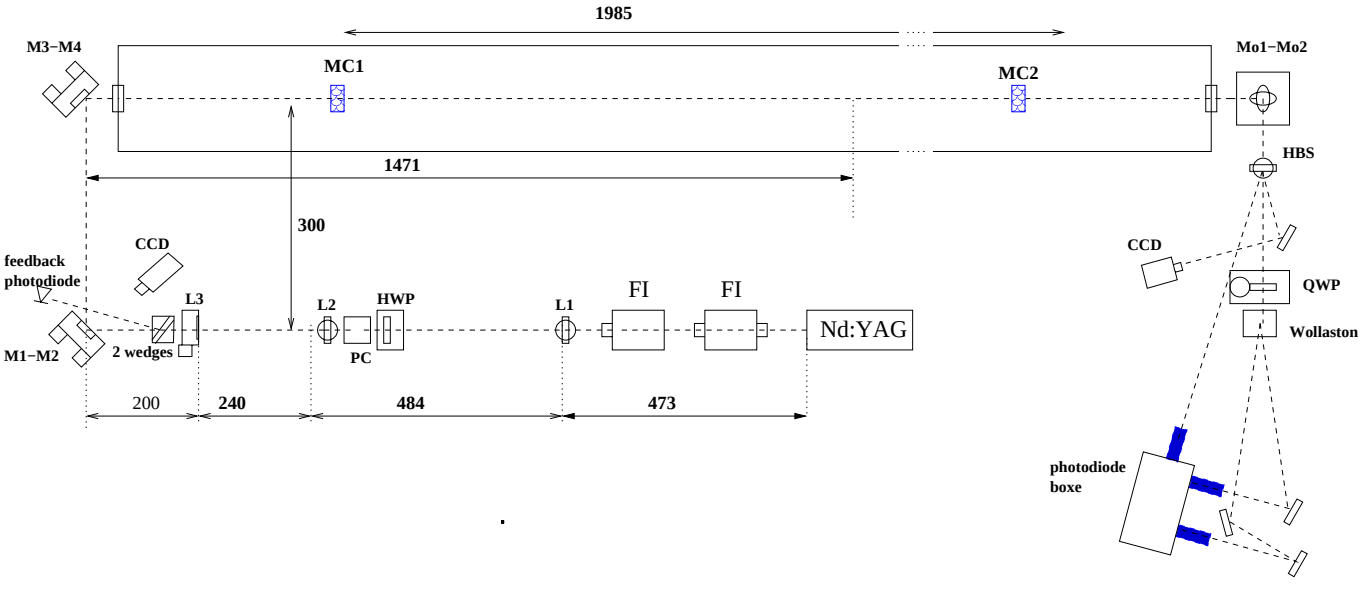

Figure 3.19: *Schematic view of the optical scheme together with main distances. From [22].*

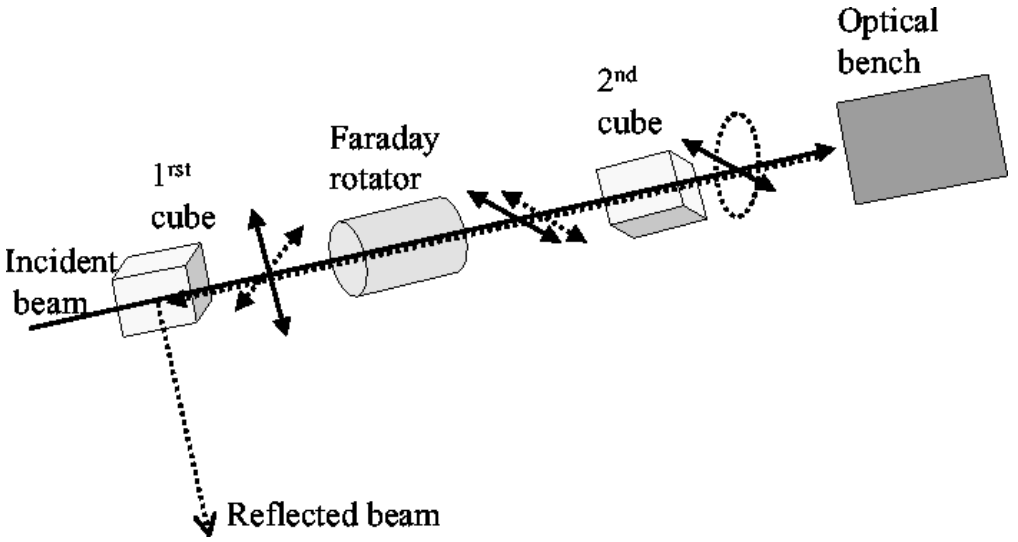

Figure 3.20: *Principle of the Faraday isolator used to protect the laser from the light reflected by an ensemble of optical elements (named optical bench on the figure). The first polarisation cube delivers linear polarised light. Then the polarisation is rotated by* 45^o *by the Faraday rotator. This component is made of a terbium gallium garnet crystal located inside a permanent magnet. After the second cube, the polarisation of the beam reflected by an optical bench (dashed ellipse and dashed arrow in the figure) will be rotated by another* 45^o *by the Faraday rotator so that it will by deflected by the first polarisation cube. The second polarisation cube is then used to match the orientation of the polarisation vector after the Faraday rotator and the polarisation of the reflected beam. This scheme leads to a 40 db laser isolation.*

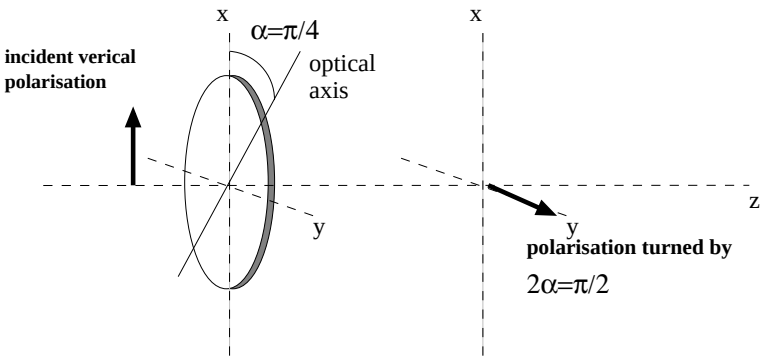

Figure 3.21: *Effect of a half wave plate on linear polarisation. See chap. 4 and appendix A for details.*

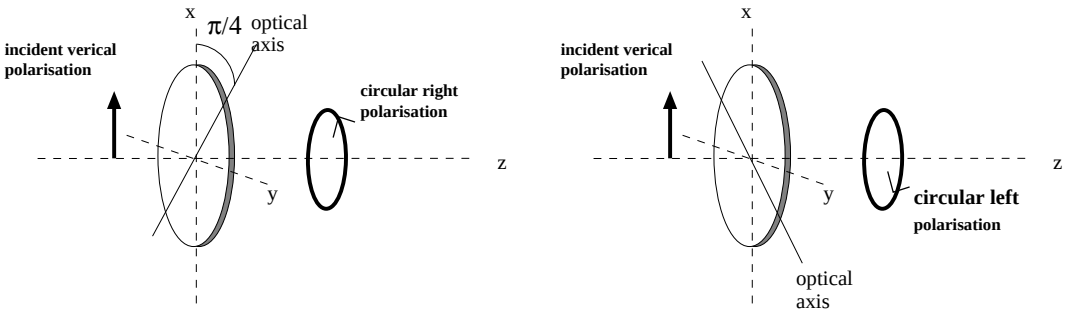

Figure 3.22: *Effect of a quarter wave plate on linear polarisation. See chap. 4 and appendix A for details.*

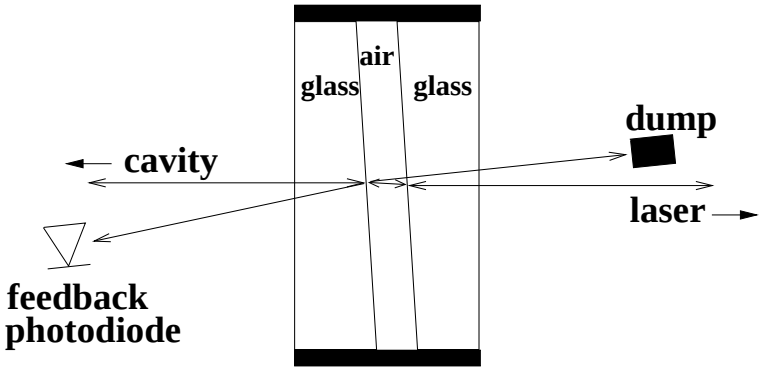

Figure 3.23: *Schematic view of the assembly of the two 6^o wedges used to pick-up the beam reflected by the cavity.*

- extraction of the signal reflected by the cavity for the feedback;
- measurement of the laser beam polarisation.

In addition, because the optical table is close to the HERA beam pipe, all operations on the optical components must be done remotely.

Our Saclay colleagues met the same constraints for the CEBAF cavity project[4, 8]. They provided a very well suited optical scheme that we also used with small modifications. Our optical scheme is shown in fig. 3.19 (see also fig. 3.6). Starting from the laser box we find:

1. A Faraday isolator which insures that no reflected beam enters the laser (this would perturbate the NPRO and then the cavity feedback). This element is made of a gyromagnetic crystal surrounded by a permanent magnet and located between two polarisation separation cubes (see fig. 3.20).

2. A second Faraday isolator used to increase the laser isolation (80 db in all). At the time of writing this document this component is not yet installed.

3. A lens ($f_1 = 400$ mm) to provide a small laser beam inside the Pockels cell and for the laser/cavity mode matching.

4. A quartz half wave plate (thickness $\approx 180\mu$m) to turn the linear polarisation before the Pockels cell (see fig. 3.21).

5. A Pockels cell: electro-optic KD*P crystal (see appendix 4.7 of chap. 4). For a certain value of the power supply on the crystal the cell acts as a quarter wave plate (i.e. the linearely polarised beam is transformed into a circularly polarised beam, see fig. 3.22). The polarisation is switched from left to right by changing the polarity of the Pockels cell high voltage.

6. Two lenses ($f_2 = -100$ mm and $f_3 = 250$ mm) for laser/cavity mode matching.

7. Two 6^o wedge glass plates (see fig. 3.23) to pick-up the beam reflected by the cavity (see fig. 3.24). This signal is used for the cavity feedback (see section 3.4) [6]. Let us mention that the scheme used at CEBAF (see chap. 5) is not usable since the switching of the Pockels cell power supply unlocks the cavity. The two wedge scheme is independent on the beam polarisation and therefore avoids the locking breakdown.

8. Four flat 45^o dielectric mirrors M1, M2, M3 and M4: they have been coated in the same run. Two of them are motorised using four Micro-Control stepper motors.

9. The cavity: a vacuum window, the two cavity mirrors and another vacuum window.

10. Two flat 45^o dielectric coated mirrors – Mo1 and Mo2 – to bring the beam emitted from the cavity down to the ellipsometer (see also fig. 3.11).

[6] In order not to increase the number of optical elements, we first installed the feedback photodiode behind the mirror M4 [23]. But, once installed at DESY, for an unknown reason, we lost a factor twenty on the feedback signal. Due to a lack of time, we used two available wedges, it would have been simpler to use a one face anti-reflection coated parallel plate.

11. An holographic beam sampler. This is a coated glass plate inducing forward diffraction. The two lateral first order beams are emitted at 10^o from the main beam and contain 1% of the power. We use them to control the cavity power and the cavity mode (see also fig. 3.11).

12. The ellipsometer: it consists in a quartz quarter wave plate (QWP), a Wollaston prism (see fig. 3.25) and three InGaAs photodiodes (see chap. 4): two of them read the light intensities of the two beams emerging from the Wollaston prism and the third one reads the laser beam power before the QWP (see previous item). These elements are also visible on the cavity output drawing of fig. 3.11 and on the photograph of fig. 3.12. This is a standard ellipsometer, by rotating the QWP in its plane and then fitting the two intensities measured after the Wollaston prism to an appropriate theoretical expression, one determines the polarisation state of the incident light.

13. Two infrared CCD cameras: one for the alignment (looking at the diffusion on the mirror M1) and one to visualise the mode after the cavity (directly in the beam).

For precise details concerning the optical principles related to the above elements we refer to [20, 21]. We shall briefly describe here the function of some of these elements.

The half wave plate (HWP) works in conjunction with the Pockels cell. For a given value of the DC voltage supplied on the Pockels cell, it serves to rotate the incident vertical polarisation and therefore contributes to define the polarisation state after the Pockels cell (see chap. 4 for details). This component is added with respect to the Cebaf's optical scheme.

The three lenses f_1, f_2 and f_3 provide the spatial mode matching of the laser beam to the cavity. There is a matrix algebra (named ABCD algebra, see refs. [2, 3]) determining the effects of a convex (concave) surface on the spatial and phase properties of a Gaussian beam[7]. Taking into account the fact that the cavity entrance mirror is spherical we have determined the position and the focal of the three lenses (in fact two would have been enough but we also have to provide a small beam inside the Pockels cell). Since our laser beam is elliptical (i.e. waists are different in x and y directions) and since it is not that easy to determine the exact position of each object on an optical table, the second lens has been mounted on a remotely controlled linear translation stage.

The four mirror M1-M4 system are used to align the laser beam onto the cavity optical axis. Two mirrors would have been sufficient for this purpose but we use four mirrors to reduce the birefringence effect (see section 3.3.3).

All our optical components are anti-reflection coated for 1064 nm. The support is an aluminium rail and the interface elements between this rail and the optical mounts have been designed and built in the LAL workshop.

We have spent much effort on the light polarisation measurement, i.e. operation and calibration of the ellipsometer. This is the subject of chap. 4.

[7]It can be easily shown, in the paraxial approximation, that a Gaussian beam is equivalent to a spherical wave with a complex radius of curvature. The ABCD algebra is then derived from the paraxial geometrical optical rules.

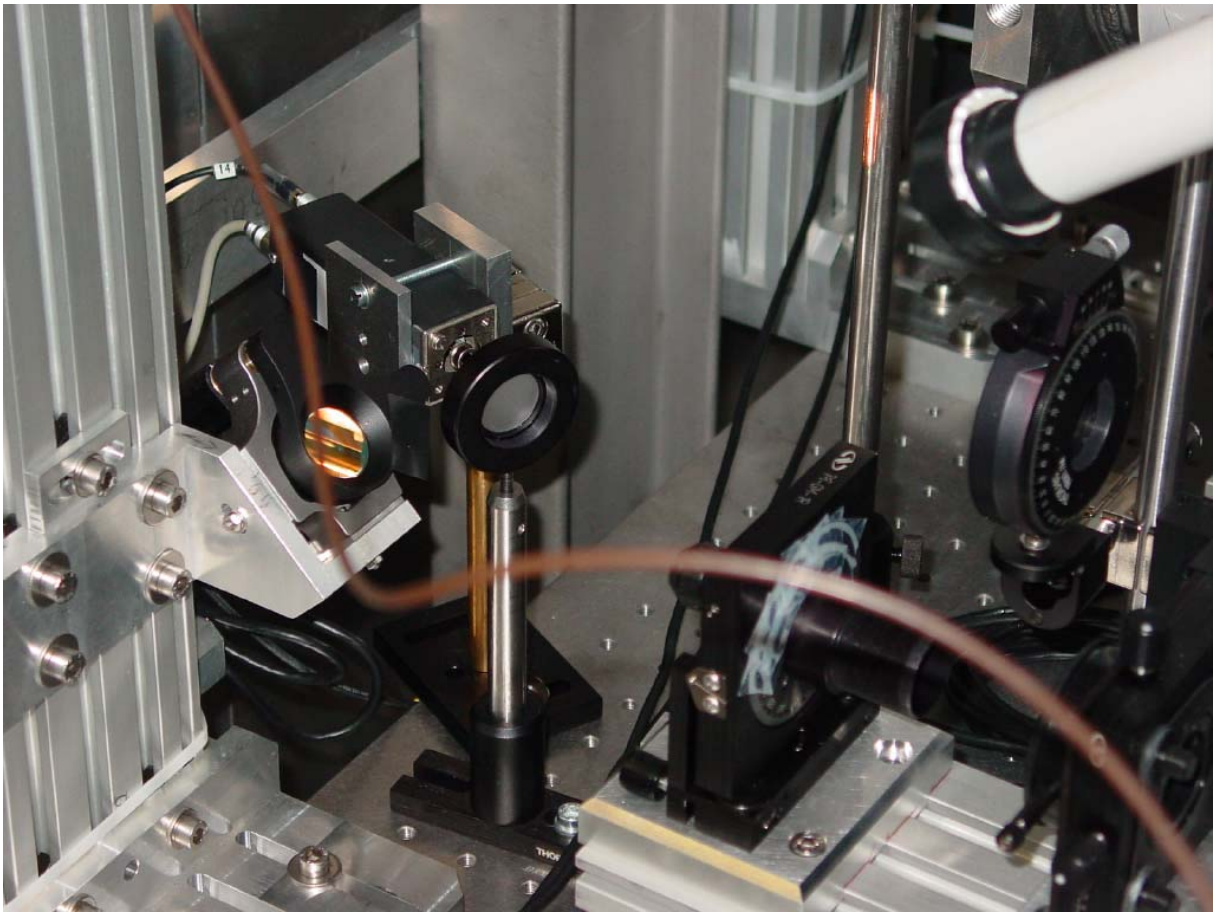

Figure 3.24: *Picture of the mirror M1, the two wedges system (located inside a black tube) and the feedback photodiode and its readout electronic box (with a diffuser in front). Also visible are the CCD used for the laser/cavity alignment (white tube, right upper corner) and the third lens (right bottom corner).*

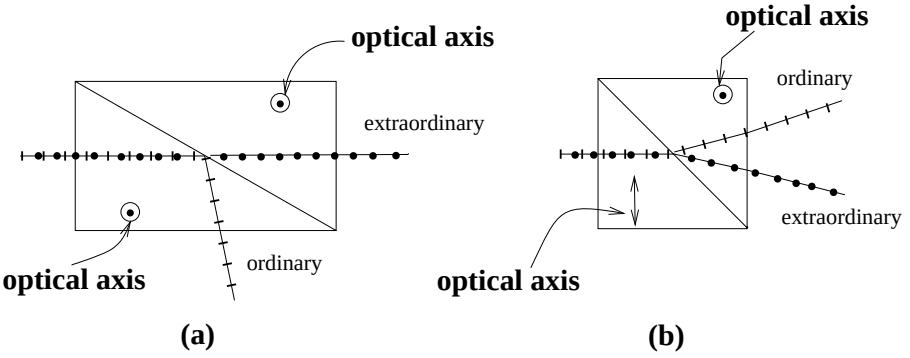

Figure 3.25: *Principle of (a) Glan-Thomson prism and (b) Wollaston prism. Both components are made of calcite (uniaxial crystal, see chap. 4 and appendix A) with optical axes as indicated in the figures. They consist in two prism optically glued. Inside the Glan-Thomson prism, at the interface between the two prisms, total internal reflection occurs for the ordinary ray so that the transmitted light is linearly polarised along the extraordinary electric vector (the second half only serves to align the transmitted ray with the incident one). For the Wollaston prism, the optical axes are oriented differently in the two halves. This leads to an angular separation of the ordinary and extraordinary waves.*

3.3.3 Parasitic ellipticity and birefringence sources of the optical setup

One of the main constraints for the optical scheme design is the necessity to provide the highest degree of circular polarisation at the centre of the cavity (for Compton scattering with the electron beam, see chap. 2). And measure it accurately afterwards.

The light polarisation state is controlled by a half wave plate and a Pockels cell. However, all the optical elements located between the Pockels cell and the cavity centre can modify the laser beam polarisation. Non-absorbing elements can in fact induce a parasitic phase shift between the vertical and horizontal components of the electric vector E_x and E_y. This phenomenon will be called here birefringence (although this word refers to the phase shift). In addition to birefringence, an ellipticity can be induced. The main contributors for this effect are the 45^o mirrors and the two wedge system.

Two 'regions' must be considered: before the cavity centre and after the cavity centre. In the former region, the parasitic birefringence reduces the effective degree of circular polarisation at the laser-electron IP. In the latter region, the birefringence introduces a systematic bias on the laser beam polarisation state measurements.

Let us give here a brief introduction on birefringence using the Jones formalism (for anisotropic crystals, see chap. 4 and for axis-symmetric induced birefringence see appendix 3.8). The Jones matrix of an ideal non-birefringent optical element is simply the 2×2 identity matrix. To take into account a small birefringence one can first assume that the effect is homogeneous within the size of the laser beam spot. Considering the normal incidence and neglecting any internal multiple reflections, the Jones matrix describing

small birefringences of a non-absorbing element is simply the one of a retardation plate:

$$M = \begin{pmatrix} 1 & 0 \\ 0 & e^{i\varphi} \end{pmatrix} \tag{3.2}$$

where φ is called the birefringence and where this matrix expression is given in the so called neutral or eigen-basis. If the incident polarisation is not aligned along the eigen-vectors of M, then a relative phase shift is induced between the two components of the electric field. To determine the birefringence of an optical element, a robust method is then to turn this element between two crossed polariser and then to measure the variation of the transmitted intensity. This method leads both to the birefringence and the neutral axis directions.

To control the birefringence/ellipticity of each of our optical elements, one possibility would then be to calibrate all of them accurately. But this task is impossible with regard to the complexity of the phenomenon. Birefringence effects are inhomogeneous, they strongly depend on the beam characteristics, ambient temperature, mechanical stress induced by the mounting and therefore on the laser beam impact point.

The first thing to do is therefore to reduce, when possible, the parasitic ellipticity/birefringence. The dominant source of parasitic ellipticity/birefringence is the 45^o dielectric mirrors since they have different reflection coefficients for Transverse Electric (TE) and Transverse Magnetic (TM) waves[8]. No information is provided by the manufacturer, but looking at various manufacturer catalogues one can estimate that reflection coefficients for TM and TE waves may differ by $\approx 0.5\%$.

To reduce this effect, we have adopted a well known mirror scheme [9]: four identical 45^o dielectric mirrors M1, M2, M3 and M4 are oriented in such a way that M1 (M2) and M3 (M4) have their normals perpendicular to each other. In this way, the TE and TM waves for M1 (M2) become TM and TE for M3 (M4) respectively so that the ellipticity is, in principle, cancelled out after M4. Since the beam must be inclined by 58 mrad inside the cavity, to keep the orthogonality between M2 and M4, M4 has been turned by 58 mrad around the x axis.

It is difficult to estimate the residual ellipticity/birefringence for this four mirrors scheme. Some studies were performed on a two mirrors scheme (like the one use after the cavity) for the Cebaf cavity project and the result was that the degree of circular polarisation is only modified by one per mille (and roughly one per mille per degree of angular mismatch between the orientation of the two mirrors)[27]. This is satisfactory.

Because it is located after the four mirrors, the cavity entrance window may induce a noticeable birefringence. Although constituted of fused silica, mechanical constraints appear because of air/vacuum pressure (this is mentioned in [25]) and the manufacturing process [28, 29, 30]. In appendix 3.8 we estimate numerically the birefringence induced by the air/vacuum pressure. We find that this effect is negligible. The birefringence induced by manufacturing process (glass-metal soldering from Vermetal) was measured by M. Lintz [31] using the crossed polariser method described above (plus a 'fine tuning' rotation/translation of the sample between the polarisers). The result is shown in fig.

[8] These are the two directions of the electric vector: in the plane of incidence (TE) and perpendicular to plane of incidence (TM). Here the plane of incidence is defined by the normal of the mirror and the laser beam propagation axis. See [24] and chap. 4 for more details.

[9] For example, this scheme is used at SLAC/SLC[25] and JLAB/CEBAF [26]

3.27. Within a few millimetre from the window centre, the birefringence can reach at most 5 mrad.

As for the cavity entrance window, one can try to compensate, at least partially, this parasitic birefringence by adjusting the orientation of the HWP and the Pockels cell power supply. In addition, depending on the orientation of the neutral axes within the laser beam spot size, the parasitic polarisation may not be totally spatially Gaussian (see appendix 3.8) so that it may be filtered out when the cavity is locked on the fundamental mode.

However, a second vacuum window is located between the cavity centre and the ellipsometer. To estimate the bias on the determination of the degree of circular polarisation – i.e. the value of the the fourth component S_3 of the Stokes vector (see section 2.2.1) – induced by the 5 mrad window birefringence, let us start from eq. 3.2. S_3 is extracted from the intensity measurements done after the Wollaston prism. The two orthogonal linear polarisation directions transmitted by the Wollaston prism define the absolute basis denoted by $\{\hat{\mathbf{x}}\ ,\hat{\mathbf{y}}\ \}$. In this basis, the Jones matrix of the birefringent component reads [21]

$$M' = R(-\alpha)MR(\alpha)$$

with α the orientation the neutral axes basis in the absolute basis (we restrict ourselves to the normal incidence) and where $R(\alpha)$ is the 2×2 rotation matrix. If we assume that the laser beam is perfectly circular inside the cavity, then the polarisation state after the window is given by $\mathbf{E_o} = M'\mathbf{E_i}$ with $\mathbf{E_i^T} = (1, i)/\sqrt{2}$. The degree of circular polarisation is further given by (see eq. 2.2 in chap. 2)

$$S_3 = i[\mathbf{E_o}.\hat{\mathbf{x}}\ (\mathbf{E_o}.\hat{\mathbf{y}}\ )^* - \mathbf{E_o}.\hat{\mathbf{y}}\ (\mathbf{E_o}.\hat{\mathbf{x}}\ )^*].$$

To second order in φ, one can write $S_3 = 1 + \Delta S_3$ with $\Delta S_3 = -\varphi^2/2$, i.e. the bias is quadratic in φ. It means that degree of circular polarisation of the laser beam is a priori measured with a systematic uncertainty of $\approx 25 \cdot 10^{-6}$ which is much smaller than our requirements. Let us mention that such small birefringence is compatible with some transmission measurements performed within the VIRGO Collaboration on the same kind of window [32].

The cavity mirrors may also introduce a birefringence because of the thermoelastic deformation due to the high power circulating inside the cavity [34]. In appendix 3.8 we estimate this effect numerically and we conclude that it is negligible. Concerning the birefringence that could be induced by the mirror coating, one can safely neglect it according to the following arguments: the laser beam is reflected under normal incidence and the diffusion coefficients are extremely small (a few ppm see table 3.2). The last source of birefringence for the cavity mirror is the mounting system. This system is shown in fig. 3.26 and it essentially consists in a spring pushing a ring in contact with the cavity mirror. The order of magnitude of the birefringence induced by mechanical stress can be estimated using a simplified version of the calculation presented in appendix 3.8. Following [33], we introduce an effective parameter $C \approx 10^-12$ Pa^{-1} for glass such that the induced birefringence reads $2\pi eCp/\lambda$ with p the pressure supplied on the mirror and e the mirror thickness. The force supplied by the spring on the mirror has been measured (by supplying weights on the system) and is estimated to be at most 2 N, that is a pressure on the mirror $\approx 10^{-4}$ Pa and then a birefringence of the order of 10^{-11} for

$e = 6\ mm$. We can therefore avoid a more quantitative estimate and conclude that this source of birefringence is negligible.

Finally, the two mirrors and the HBS located after the cavity can also induce a birefringence. The HBS birefringence was also measured by M. Lintz [31] but, for this component, it was found to be below the measurement sensitivity (≈ 0.3 mrad) and therefore negligible with regard to our precision requirement. However, the HBS was mounted in a mirror mount for this measurement and we observed a noticeable birefringence when the locking screw was too tight. We then fixed the HBS in its mount using a stress-free glue. As for the two mirrors system, an in situ calibration procedure has been foreseen (see section 3.3.4) though, as described above, they are not expected to modify significantly the light polarisation.

.

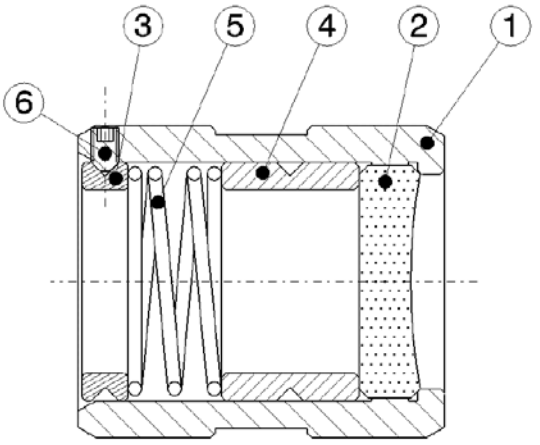

Figure 3.26: *Technical drawing of the cavity mirror mount system.* ①*: mirror holder;* ② *: mirror;* ③*: spacer;* ④*: spacer;* ⑤*: spring;* ⑥*: stop screw. From [10].*

3.3.4 Optical calibration procedure

As mentioned in the previous sections, the laser beam polarisation is not measured before the inner part of the cavity and ellipticity/birefringence can be induced by certain of our optical elements. To optimise the degree of circular polarisation at the laser/electron IP, we follow the method of ref. [25]: since the Compton total cross section is an increasing function of the level of circular polarisation, we vary the Pockels cell's voltage and the optical axis orientation of the associated HWP in order to maximise the total number of backscattered photons. Since at the time of writing this document no electron beam has run in HERA yet, we cannot give any result on this procedure.

In order to control the parasitic ellipticity/birefringence induced by our optical elements, we have foreseen to insert a high quality linear polariser (i.e. a Glan-Thomson

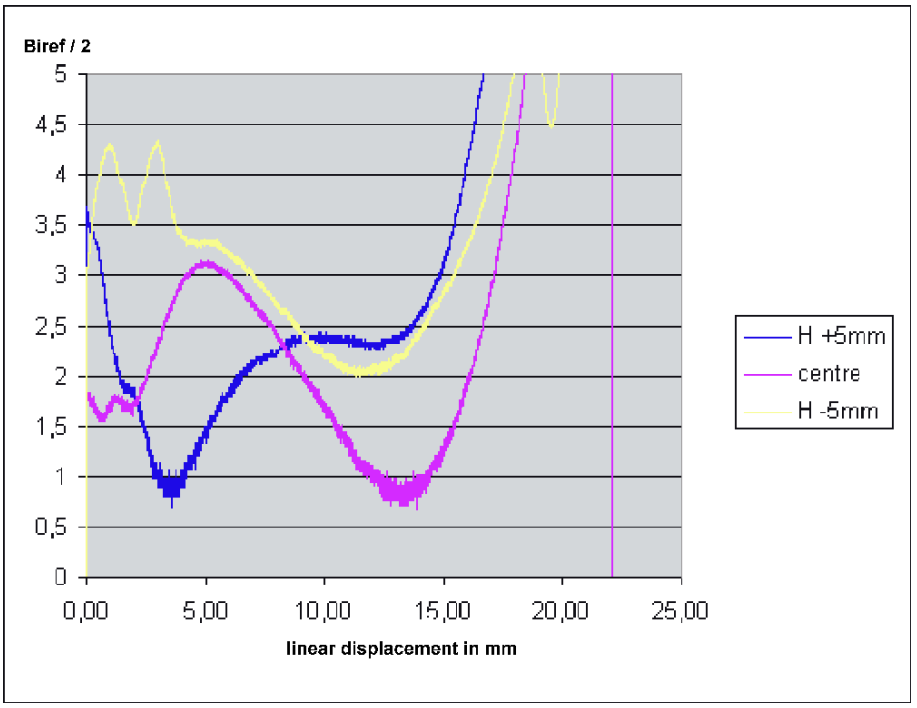

Figure 3.27: *Result of the vacuum window birefringence measurement. Different curves correspond to different linear position scans (at the centre and ± 5 mm apart). The window's centre corresponds to 11 mm on the abscissa axis and half the birefringence is plotted on the vertical axis. Measurements are from [31].*

prism) at various places in our optical scheme: before the four mirror system, before the cavity, after the cavity, before the QWP of the ellipsometer. Rotating the QWP for all these configurations leads, step by step, to an estimate of the optical response of the main pieces of our setup. Again, but here because of a lack of time, we didn't perform this study at the time of writing this document. We postponed these series of measurements for the HERA shutdown of winter 2003.

3.4 Feedback system

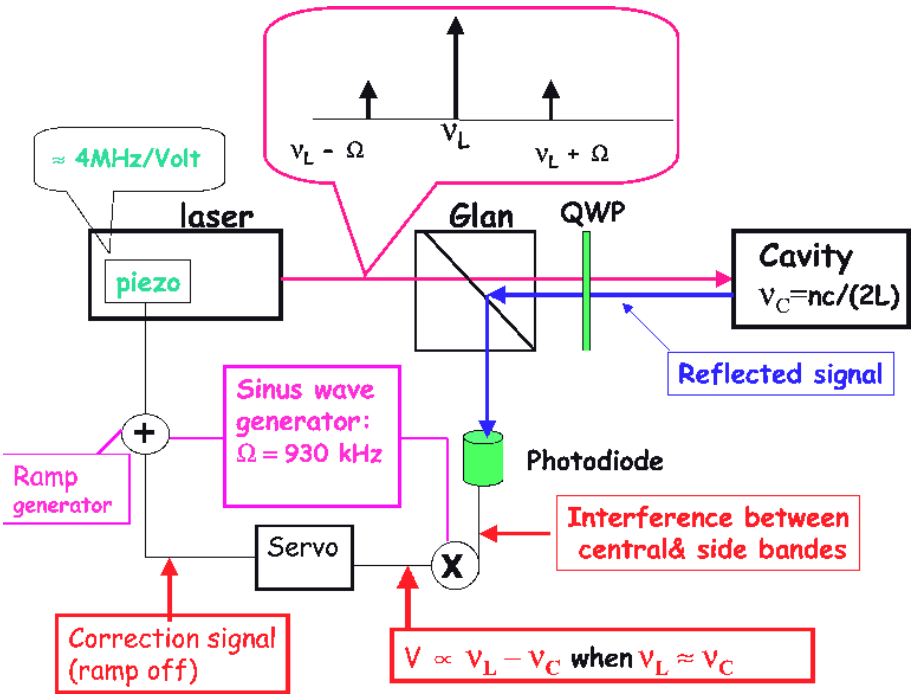

Figure 3.28: *Simplified view of the feedback system (see text).*

The 'Pound-Drever' technique [35, 36] is used for the laser-cavity feedback. This method is illustrated in fig. 3.28. The laser beam frequency is modulated by applying a periodic signal of 50 mV amplitude and $\Omega = 930$ kHz frequency on the piezo transducer (via the laser fast channel, see section 3.3.1). Beside the laser beam frequency ν_L, two side bands of frequencies $\nu_L \pm \Omega$ are generated by this modulation [37]. The electric field has thus three frequency components and the reflected signal measured by the photodiode results from the interference between the central and the side bands. It can be shown (details can be found in ref. [4]) that a demodulation of this signal at the frequency Ω leads to an error signal usable for a feedback loop: close to a cavity resonance frequency ν_c, the error signal is linearly proportional to the difference $\nu_L - \nu_c$ (see fig. 3.29).

To lock the cavity, an electronic feedback system has been designed and built by the SIG group of Saclay. It is a copy of the system used for the CEBAF cavity (itself inspired by the PVLAS experiment system [38]).

This system is depicted in fig. 3.30. A 10 V peak-to-peak ramp, together with the 930 kHz modulation, is supplied on the laser piezo transducer (via the fast channel). The